Title
Printable Mechanical Autonomy

Author
Yan, Wenzhong

Publication Date
2023

Peer reviewed|Thesis/dissertation

UNIVERSITY OF CALIFORNIA

Los Angeles

Printable Mechanical Autonomy

A dissertation submitted in partial satisfaction

of the requirements for the degree

Doctor of Philosophy in Mechanical Engineering

by

Wenzhong Yan

2023

ABSTRACT OF THE DISSERTATION

Printable Mechanical Autonomy

by

Wenzhong Yan
Doctor of Philosophy in Mechanical Engineering
University of California, Los Angeles, 2023
Professor Ankur M. Mehta, Co-Chair
Professor Jonathan Hopkins, Co-Chair

Printable robots created using origami-inspired folding processes have gained extensive attention due to their potential advantages, including low cost, rapid prototyping, lightweight, high accessibility, built-in compliance for safe interaction with humans, compact storage, etc. However, to achieve autonomy, printable robots still rely on bulky, rigid semiconductor-based electronics and their accessories (e.g., electromechanical motors), which could restrict the full potential promised by origami-inspired printable manufacturing. Here, I introduce an integrated folding-based process to create autonomous printable robots by embedding sensing, control, and actuation into compliant materials without requiring semiconductor-based electronics. By combining flexible bistable mechanisms and conductive thermal artificial muscles, we realize various autonomous behaviors. These include self-sustained locomotion and sequencing, information processing, logic and computing, and human/environment-machine interactions without the need of semiconductor-based components. Guided by theory, I have also derived simplified analytical models for the above-mentioned printable devices to enable rapid design and prototyping. Our work opens up new design space for autonomous origami

machines that are low cost, lightweight, and robust to adversarial environmental factors (e.g., magnetic field and physical deformation). This thesis provides routes to achieve autonomy for printable robots through tight functional integration in compliant materials and structures.

The dissertation of Wenzhong Yan is approved.

Veronica Santos

Qibing Pei

Mohammad Khalid Jawed

Jonathan Hopkins, Committee Co-Chair

Ankur M. Mehta, Committee Co-Chair

University of California, Los Angeles

2023

To my cherished family and beloved friends.

TABLE OF CONTENTS

LIST OF FIGURES

LIST OF TABLES

VITA

2013 B.S. (Thermal Energy and Power Engineering), Beihang University.

2016 M.S. (Aerospace Propulsion Theory and Engineering), Beihang University.

2016–present Ph.D. student, Mechanical and Aerospace Department, UCLA.

PUBLICATIONS

Wenzhong Yan(✉), Shuguang Li, Mauricio Deguchi, Zhaoliang Zheng, Daniela Rus, and Ankur Mehta. "Origami-based integration of robots that sense, decide, and respond". *Nature Communications,* 14 (1), 2023 (Featured by the editors in a Collection and Focus).

Wenzhong Yan(✉), and Ankur Mehta. "A Cut-and-Fold Self-Sustained Oscillator for Autonomous Actuation of Origami-Inspired Robots". *Soft Robotics*, 9 (5), 2022.

Wenzhong Yan(✉), and Ankur Mehta. "A crawling robot driven by a folded self-sustained oscillator". *IEEE International Conference on Soft Robotics*, pp. 455-460, Edinburgh, U.K., 2022.

Wenzhong Yan(✉), Chang Liu, and Ankur Mehta. "Origami Logic Gates for Printable Robots". *IEEE/RSJ International Conference on Intelligent Robots and Systems*, pp. 6084-6089, Prague, Czech Republic, 2021.

Wenzhong Yan(✉), and Ankur Mehta. "Towards One-Dollar Robots: An Integrated Design and Fabrication Strategy for Electromechanical Systems". *Robotica*, 41 (1), 2020.

Wenzhong Yan(✉), Yunchen Yu, and Ankur Mehta. "Analytical Modeling for Rapid Design of Bistable Buckled Beams". *Theoretical and Applied Mechanics Letters*, 9(4), 264-272, 2019.

Wenzhong Yan(✉)#, Yunchen Yu #, and Ankur Mehta. "Rapid Design of Mechanical Logic Based on Quasi-Static Electromechanical Modeling". *IEEE/RSJ International Conference on Intelligent Robots and Systems*, pp. 5820-5825, Macau, China, 2019.

Wenzhong Yan(✉), Angela L. Gao, Yunchen Yu, and Ankur Mehta. "Towards Autonomous Printable Robotics: Design and Prototyping of the Mechanical Logic". *International Symposium on Experimental Robotics*, pp. 631-644, Buenos Aires, 2018.

CHAPTER 1

Introduction

1.1 Background and Motivation

In nature, the origami-inspired method plays a vital role in the creation of a wide spectrum of complex biological structures, from proteins to insect wings. Inspired by nature, roboticists explore origami as a design and fabrication strategy, also called printable manufacturing. This printable manufacturing is done using patterned two-dimensional (2D) sheets or even linear threads that can be folded into desired three-dimensional (3D) configurations (different from 3D printing). This strategy provides a simple yet elegant approach to construct a wide range of robot morphologies and functions [19], such as crawling [20], grasping [1], swimming [21], shape morphology [22], self-folding [23], locomotion [24], or combinations of these tasks [25–27]. Such origami-inspired folded devices have several potential advantages, including rapid design and fabrication [28], low cost and high accessibility [29], high strength-to-weight ratio [30], compact storage and transport [6], reconfigurable structures [31] and self-folding [32], and high scalability [33, 34]. However, printable robots has until now mainly focused on the development of physical structures, while relying on semiconductor-based electronics for sensing, actuation, and control, limiting their potential associated with origami-inspired manufacturing [19].

In this thesis, I address the challenge of realizing complete robots made almost entirely of printable mechanisms towards achieving the full potential of printable robots; in particular, I propose to design electromechanical transducers coupled with autonomous controllers

out of sheet materials and string actuators. Figure 1.1 presents the concept for such a method for autonomous, untethered robots—the robots can be created entirely from sheet and thread materials through cut-and-fold processing. I have demonstrated the integration of components critical for this vision (see Fig.1.1 B, C, D, and E); this could be combined with developments in energy storage [35, 36] and stimuli-responsive materials to build such untethered, autonomous robots. By only requiring nearly universally accessible raw materials for the entirety of the robot, we can significantly broaden the reach of robotic technology. For example, the extremely low-cost and easy-to-fabricate characteristics could open up applications in educational tools and toy industry [37]. Furthermore, the electronics-free and nonmagnetic feature of the resulting robot might make them more applicable for tasks in challenging environments. Potential tasks include exploration, rescue, and navigation in high magnetic fields or locations with strong radiation.

1.2 Related Work

Since a comprehensive review on the design, fabrication and control of origami-inspired printable robotics has been summarized in [19], this chapter only focuses on engineering strategies for printable robotic systems, including general origami concept, origami-inspired manufacturing methods, current mechanical autonomy strategies, and relevant topics, i.e., multistable mechanisms and conductive threads (and resulting CSCP actuators).

1.2.1 Origami in Nature, Art, and Mathematics

Origami mechanisms (folding) can be widely found in nature, human art, and mathematics. In nature, origami structures and mechanisms exist across a wide range of geometry scales. DNA (or RNA) is the smallest origami bio-structure. DNA (or RNA) starts as a molecule composed of two polynucleotide chains and folds to form a double helix carrying genetic information for the growth, regulation, and reproduction of almost all organisms (and many

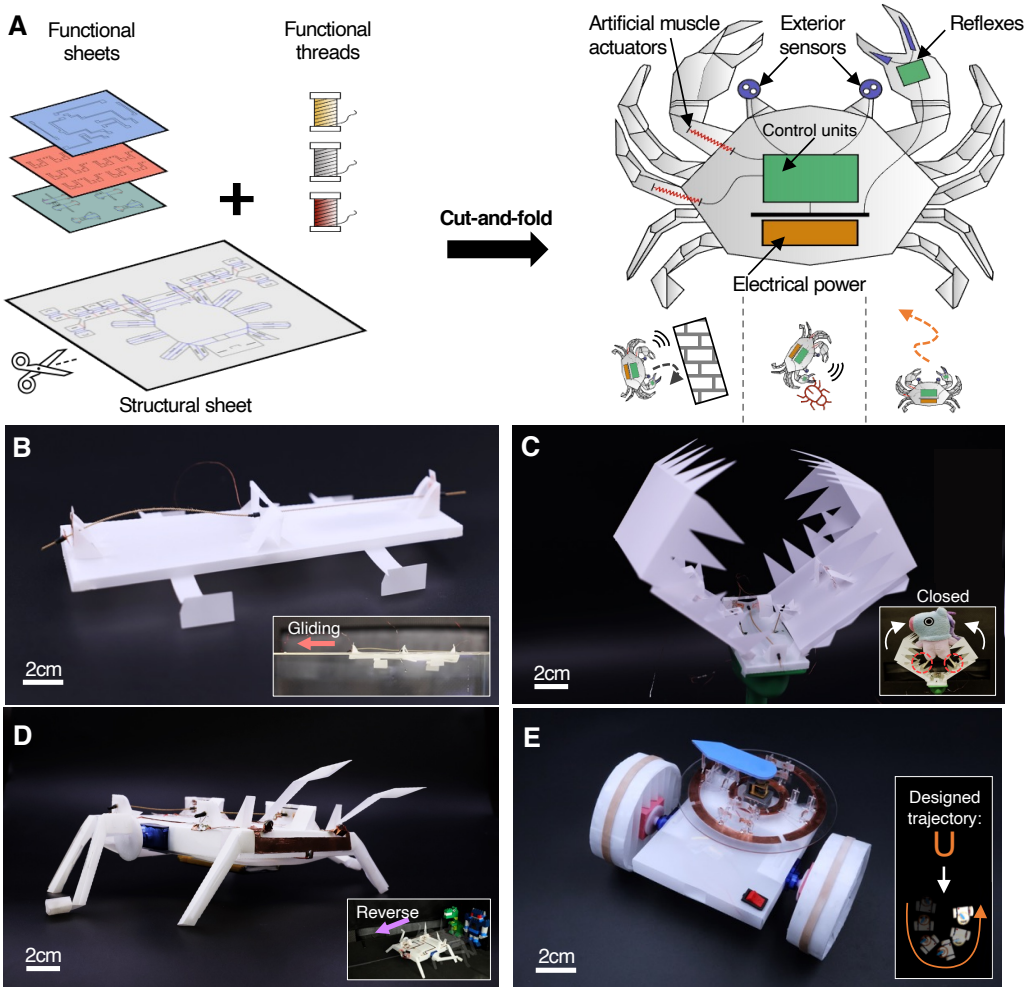

Figure 1.1: Autonomous, untethered robots with sensing, computing, and actuating tightly integrated in compliant origami materials. (A) A concept for an autonomous robot entirely created from functional sheet materials and threads through cut-and-fold processing. (B) A swimmer that glides on water autonomously. (C) A flytrap-inspired robot that distinguishes active objects from static stimuli and closes its leaves to capture its 'prey'. (D) A crawler that detects obstacles and executes decision-making to reverse its direction. (E) An untethered car that locomotes along reprogrammable trajectories.

viruses) [38]. Other examples on a small scale include proteins [39] and enzymes [40]. These molecules harness origami folding (or unfolding) to construct their functionalities.

Figure 1.2: Origami in nature. (A) A earwig with its wing unfolding (source: Faber et al. [1]). (B) Unfolding of common beech leaves. Left: buds just after opening; right: corrugated leaves (source: Kobayashi et al. [2]). (C) Section view of a piece of small intestine with circular folds (source: Waugh et al. [3]).

On larger scales, origami mechanisms are extremely useful due to their superior specific strength, light weight, compactness, high deployability and so forth. A typical example is Dermaptera wings, commonly known as earwigs, as shown in Fig 1.2A. These highly specialized wings can have an extremely high folding ratio (closed/open area), with reported values of around 1:10 [41]. This high folding ratio not only gives earwigs a compact, folded package for routine locomotion and navigation, but also provides them with a large beating surface for flight when unfolded. Similar strategy can be seen with most plants. They fold their leaves or flowers at early stages and deploy them while growing (see Fig. 1.2B) [2]. Due to its folding nature, origami is commonly employed to increase surface area within a constrained volume. For example, the small intestine harnesses folding to increase the contact area with ingested food to improve nutrients absorption (see Fig. 1.2C). [42].

Inspired by nature, ancient artists started using folding to create 3D structures from 2D planar materials (e.g., paper). Previously, designers had to decide the final architectural shapes with appropriate folds intuitively. The best-known origami design is the paper crane with its 2D folding pattern shown in Fig. 1.3A and B. The 2D pattern includes mountain folds (red) and valley folds (blue). Modern origami artists generally discourage cuts (or openings) or glue agents on paper. In other words, they prefer to only use flat square sheets

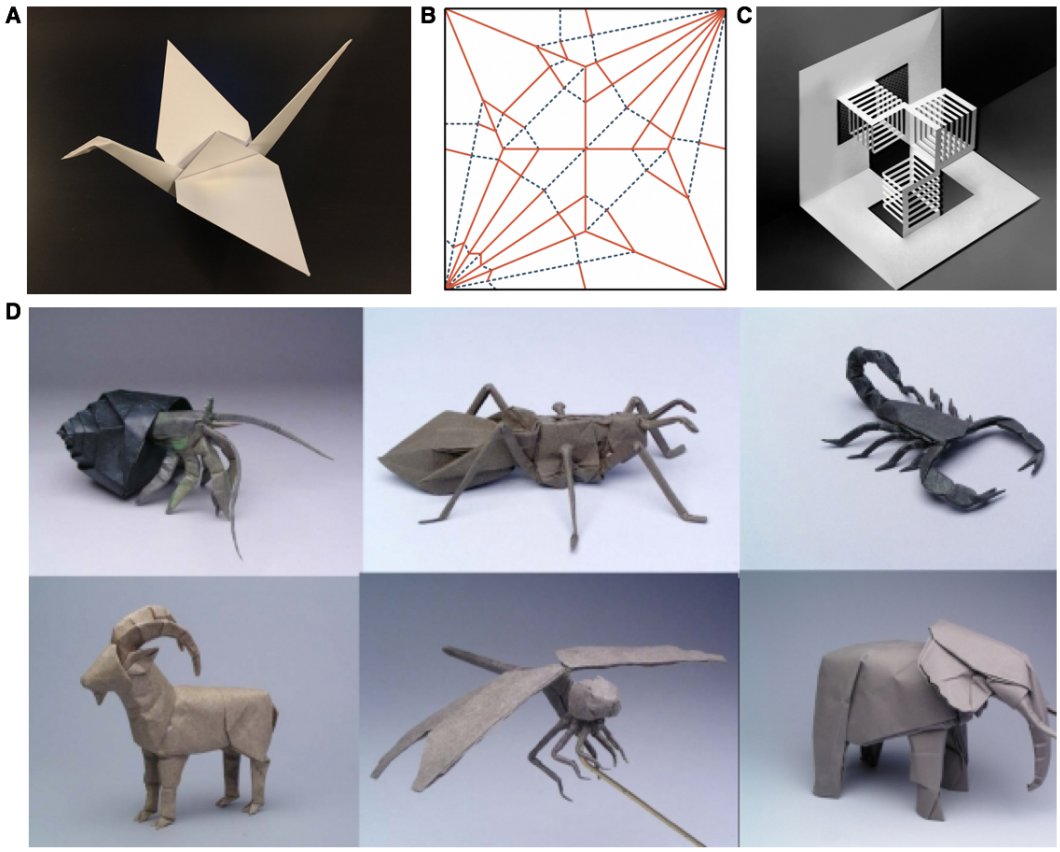

Figure 1.3: Origami arts. (A) An origami crane (source: Happy Friday) with its folding pattern in (B) (source: Rabbit Ear). (C) A kirigami pop-up card. (D) A collection of artworks of Robert J. Lang (source: FAENAaleph).

of paper. Otherwise, artists refer to designs with cuts (or openings) as Kirigami, which is a subset of origami art. An example of Kirigami artefacts is shown in Fig. 1.3C. In this thesis, we do not distinguish between them.

Due to the complexity of folding and lack of systematic methodology, the resulting 3D artifacts are usually simple. By introducing math into origami, folders can harness algorithms to generate endless types of origami models. Robert J. Lang is one of the most famous origami artists and theorists. Robert has studied the mathematics of origami and then employed computers to investigate the intrinsic theories, allowing him to create complex and elegant designs, such as insects and animals (see Fig. 1.3D). Recently, origami mathematicians have

proven the universality of origami theoretically: any polygon or polyhedral shell can be folded from a single rectangular piece of paper [43]. In addition, practical solutions were developed without requiring extra paper and folds [44, 45]. The origami-inspired method and its mathematical model can be a powerful design and manufacturing tool for robotics advancement, leading to the origami-inspired printable manufacturing strategy [46].

1.2.2 Origami-Inspired Printable Manufacturing

Origami-inspired engineering, as a top-down approach, enables unprecedented rapid prototyping and customization of robots by manufacturing structures in a 2D plane and folding them into their final 3D shape. The power of origami-inspired planar design and fabrication has been found in several applications [30, 47–51]. Nevertheless, creating complicated electromechanical robotic systems using origami-inspired printable manufacturing remains challenging.

Recently, Onal et al. [4] developed a general principle of building worm robots, whose bodies are made of only a flat sheet and whose actuation is realized with NiTi coil actuators placed on the robot's body (see Fig. 1.4A). Mehta et al. [29] proposed a method to co-generate mechanical, electrical, and software designs for printable robots from structural specifications. So far, origami folding has mostly been harnessed to form the mechanical subsystems of origami robots. The electrical subsystems are still constructed with traditional bulky electronic components and wiring. This method is widely adopted thanks to its simplicity and minimal design iterations required. In other words, the origami-inspired method is merely a rapid and inexpensive alternative to conventional manufacturing approaches (e.g., molding), while the barrier in constructing the robots' electrical subsystems and integration of these subsystems remains unsolved. Subsequently, some attempts have been made to incorporate the mechanical and electrical subsystems into integrated systems that can be created through the origami-inspired method. Onal et al. [52] devised smart laminates that contain an electronic layer for the control and actuation of the folded mechanism.

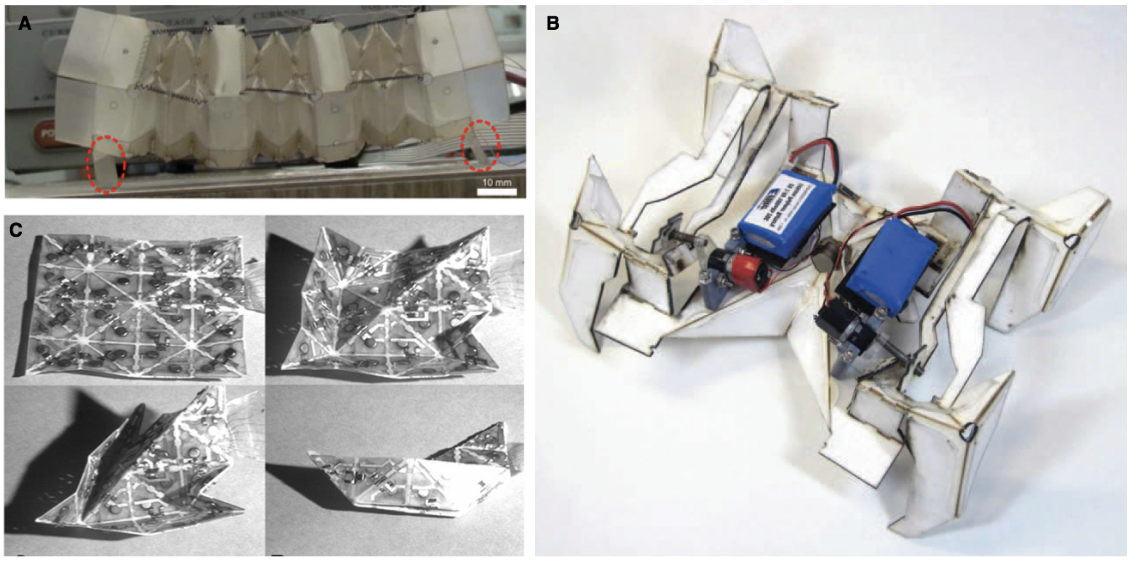

Figure 1.4: Printable manufacturing. (A) Peristaltic crawling locomotion of an origami printable robot (source: Onal et al. [4]). (B) A self-folding crawler built with the laminated shape-memory composite (source: Felton et al. [5]). (C) A a self-folding "boat" composed of programmable universal sheet (source: Hawkes et al. [6]).

Felton et al. [5] then proposed more sophisticated multilayer laminates including self-folding hinges that can be controlled by embedded heating elements, resulting in self-folding functional machines, as shown in Fig. 1.4B. This class of laminates have been found to be very useful for various applications due to their capabilities of forming functional, complicated 3D mechanisms (e.g., reconfigurable robots [6], see Fig. 1.4C).

However, these laminates require expensive materials and elaborate fabrication processes, which seriously limit their accessibility to casual end-users. In summary, current design and fabrication strategies for origami robots either depend on carefully constructed materials or merely replace mechanical structures with their origami counterparts, yet still requiring conventional electrical components and software. Therefore, these design and fabrication strategies have limited the accessibility of robotic creation due to resource constraints. In this thesis, we will explore various design and manufacturing schemes to expand the design space of robotic electromechanical systems by using origami-inspired methods. It is expected

that these designs and manufacturing schemes will employ inexpensive and widely available materials, as well as simple fabrication processes, which will lead to increased accessibility for the general population.

1.2.3 Mechanical Autonomy

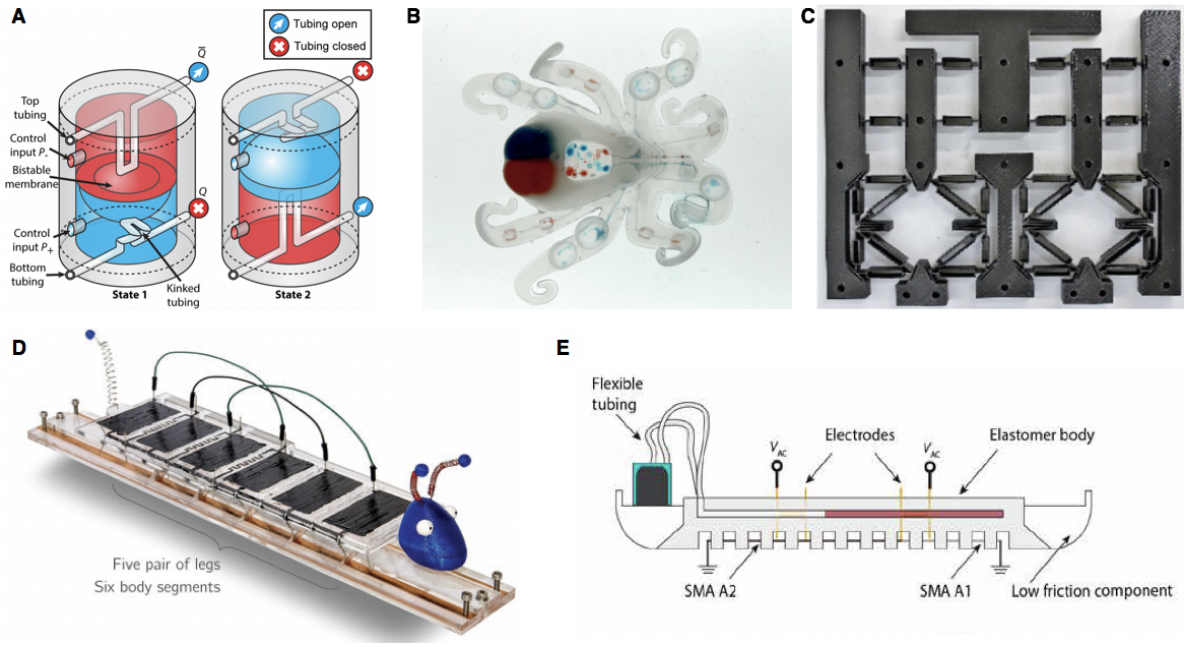

Figure 1.5: Mechanical autonomy. (A) A soft, bistable valve for autonomous control of soft actuators. (source: Rothemund et al. [7]) (B) The first entirely soft, autonomous robots, Octobot (source: Wehner et al. [8]). (C) A macroscale NAND gate printed by a commercial Fused Deposition Modeling (FDM) 3D-printer. (source: Song et al. [9]). (D) A biomimetic, electronic-free crawling locomotion robot, "Trevor", composed of six body segments and five pairs of legs (source: Henke et al. [10]). (E) An SMC (soft matter computers)-controlled Softworm robot, capable of producing three distinct gaits (source: Garrad et al. [11]).

Recently, advances in materials and mechanisms have enabled the embodiment of control in mechanical architectures. Fluidic oscillators, including microfluidic logic [53] and pneumatic ring oscillator (see Fig. 1.5A) [7, 54], are able to generate oscillatory pressure outputs

without hard components or electronic control. These oscillations can be harnessed to implement periodic actuation (see Fig. 1.5B) [8] and rolling locomotion [54] for fully soft robots and only requires a constant pressure source. Nevertheless, these fluidic oscillators function through the interactions between the fluidic and elastomeric components, which are barely possible to be adapted into origami robots configuration. Another class of oscillators feature autonomous oscillation under respective constant stimulus fields, such as humility gradient [55], temperature discrepancy [56] and visible light pattern [57]. The behaviors of these oscillators highly depend on stimulus fields and thus have limited controllability, thus constraining robot autonomy. Soft dielectric elastomer oscillators (see Fig. 1.5D) function similar to their electronic analogy, ring oscillators. They are based on the interaction of DES/DEA (dielectric elastomer switch/dielectric elastomer actuator) [10]. However, the requirements for high voltage and rigid support frames preclude their employment in untethered origami robots.

In addition to oscillators, there are attempts to implement mechanical computing systems [58]. Such computing systems include MEMS (micro-electro-mechanical system) logic gates [59], all-optical logic gates [60], and magnetic bubble logic devices [61]. Logic devices on a macro scale have also been proposed and investigated, such as additively manufacturable logic gates (see Fig. 1.5C) [9] and fully soft digital logic (see Fig. 1.5E) [11, 62]. However, these existing mechanical computing systems are not compatible with the origami-inspired method and usually require expensive and complicated fabrication, which will, in turn, limit accessibility to robotics. New strategies for embedding control, sensing, and actuation into mechanical structures are needed to achieve the full potential of printable robots; in particular, the use of only universal materials will broaden the accessibility to robotic creation by reducing cost and specific skills [63].

1.2.4 Multistable Mechanisms

Recently, multistable structures and mechanisms have been explored as powerful building blocks to create structures and materials with new functionalities. These include shape-reconfigurability, reusable energy-trapping metamaterials, and soft robots capable of jumping. In this thesis, we focus on two basic forms of multistable mechanisms, namely bistable and monostable mechanisms with snap-through transitions. These multistable mechanisms show a strong nonlinear relationship between displacement and actuation force as shown in Fig. 1.6.

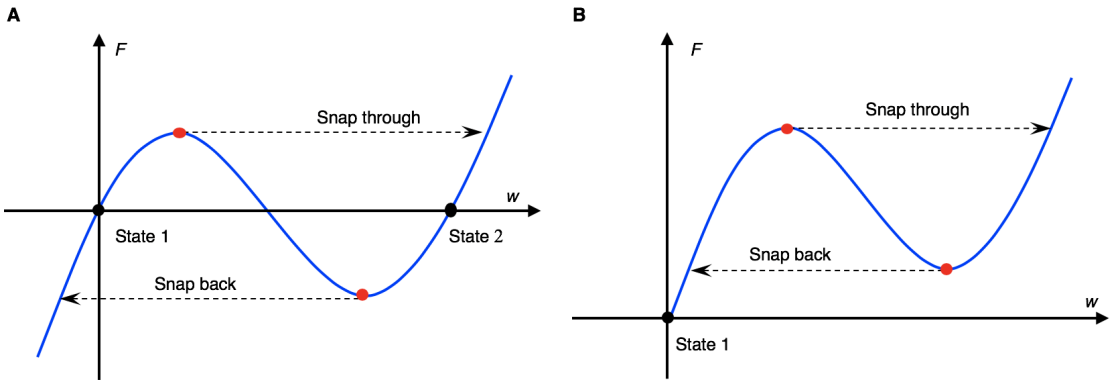

Figure 1.6: (A) A typical displacement-force curve of a bistable mechanism with two stable equilibrium states. (B) A typical displacement-force curve of a monostable mechanism with one stable equilibrium state.

Bistable mechanisms, featuring two stable equilibrium states, have been investigated for a long time. These mechanisms are ideal as switches because power is only required for switching them from one equilibrium state to the other but not for maintaining a current state. Meanwhile, their rapid and large-stroke transition between the two stable states during snap-through motions makes them apt candidates for actuators. Thanks to these advantages, bistable structures are extensively harnessed in various engineering domains, such as MEMS [12] (see Fig. 1.7A), robotics (see Fig. 1.7B) [13], energy harvesting [64], actuators [65, 66], origami technology (see Fig. 1.7C) [14], signal propagation (see Fig.

1.7D) [15], and deployment mechanisms [67]. In addition, bistable mechanisms possess high reliability, high structural simplicity, and consume relatively little power when incorporated into mechanical systems, which are potentially desirable for aerospace applications, e.g., energy absorbing [68] when aerospace devices are subjected to foundation excitation [69, 70] or becomes suddenly unbalanced [71]. The realization of these desirable properties requires more dedicated efforts.

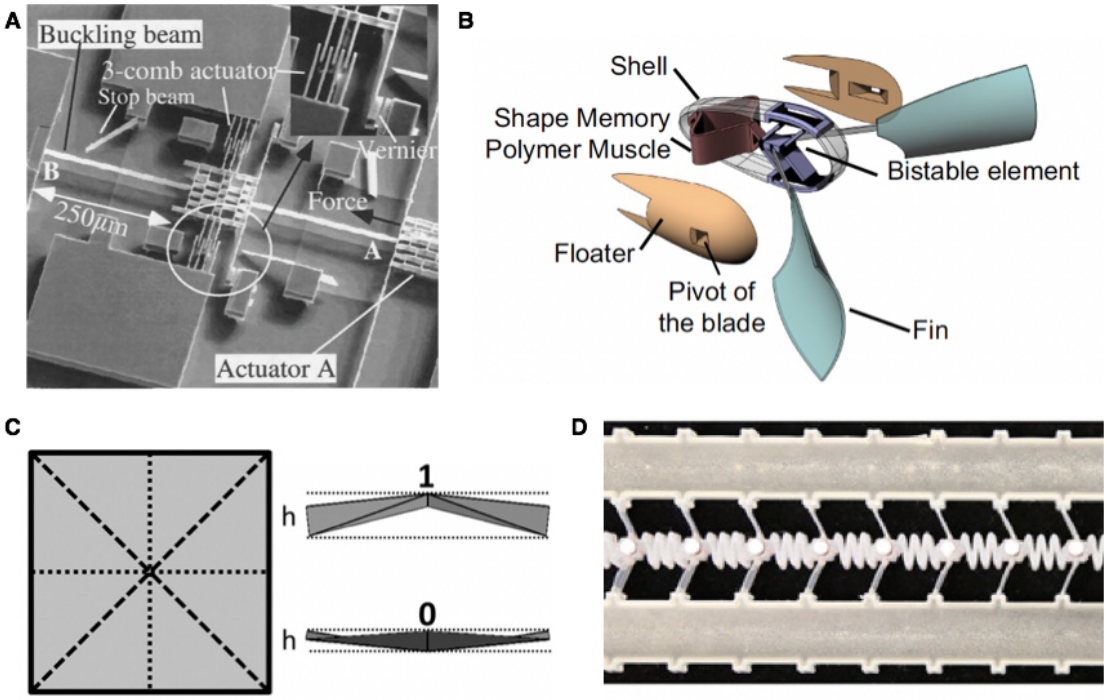

Figure 1.7: Bistable mechanisms and applications. (A) A MEMS bistable device composed of an actuator A, three-comb actuator, and a buckling beam AB (source: Taher et al. [12]). (B) A soft, untethered robot, capable of directional propulsion by harnessing bistability (source: Chen et al. [13]). (C) A bistable origami mechanomemory. left: fold pattern for a waterbomb; right: the 1 and 0 states of the waterbomb base (source: Treml et al. [14]). (D) A 1D mechanical signals propagating system, consisting of a series of bistable elements connected by soft coupling elements (source: Raney et al. [15]).

Monostable mechanisms have similar properties to bistable mechanisms, however, they

have only one stable state. Following the removal of the applied force, the mechanism can snap back to its stable state as shown in Fig. 1.6B. This special dynamic property allows automatic reset behaviors, which enables a series of applications, such as the soft valve [7,54] (see Fig. 1.5A).

In summary, all these special properties, especially the high nonlinearity of both bistable and monostable mechanisms suggest the potential to function as control or sensing elements. These elements might be incorporated into fully printable robots.

1.2.5 Conductive Threads

Recently, intrinsically soft conductive threads have been extensively used in wearable devices [72,73]. These conductive threads can be fabricated into different configurations that function as soft circuits, switches (see Fig. 1.8A) [16] , antennae [74], actuators (see Fig. 1.8B) [75], and sensors (see Fig. 1.8C) [18], etc.

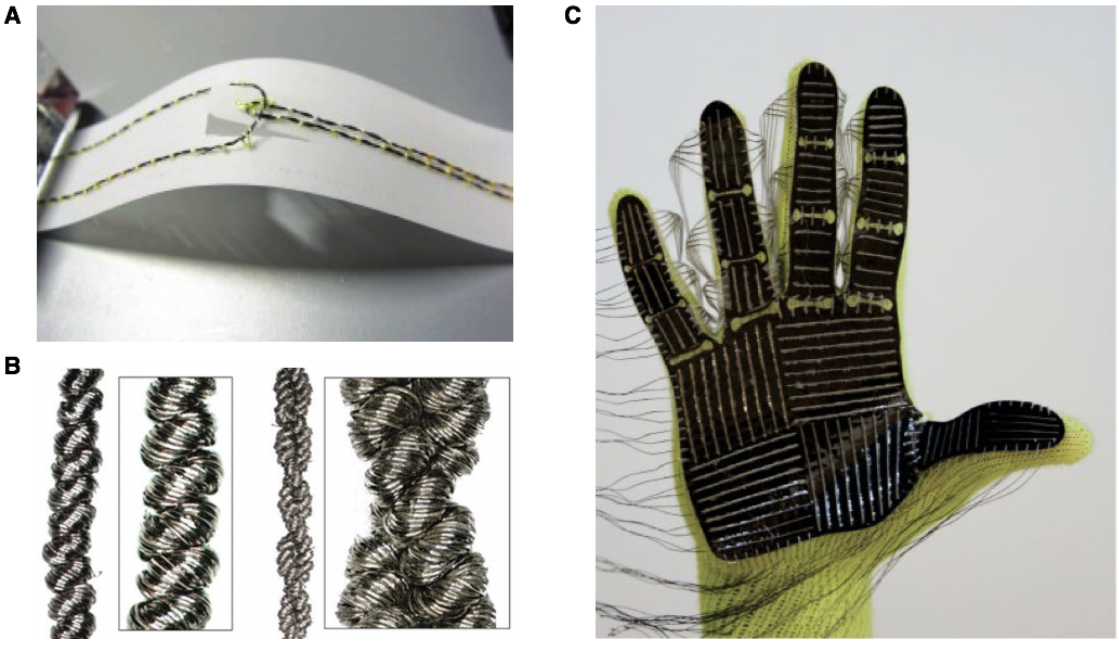

Figure 1.8: Conductive threads as functional components. (A) A cantilever switches composed of conductive threads and bendable substrate materials (source: Harnett et al. [16]). (B) CSCP actuators. Left: single ply actuator; right: a double ply actuator (source: Yip et al. [17]). (C) A scalable tactile glove composed of a piezoresistive film sensors connected by a network of conductive thread electrodes that are passively probed (source: Sundaram et al. [18]).

The CSCP actuators are a trending technology due to their high performance and versatility [76]. These CSCP actuators, twisted and annealed from conductive threads, not only exert large amounts of force, but also function as conductors. This unique combination may lead to many potential applications, such as actuation for robot arms [17]. Meanwhile, the low cost and easy fabrication of this conductive thread have drawn our attention thanks to its high potential to be integrated into printable robots. Nevertheless, few attempts have been made to incorporate these threads into origami robots, leaving their integration a challenge. This thesis makes use of CSCP actuators as conductors and actuators, combining them with multistable mechanisms to embed control and sensing into origami-inspired structures to

generate fully printable robots.

1.3 Organization and Outline

The rest of the thesis consists of four chapters and the content of each chapter is as follows:

In Chapter 2, we present the design of a self-sustaining printable oscillator that generates periodic oscillations by harnessing bistable mechanisms and conductive actuators. I report printable manufacturing methods for this class of oscillators and explore their potential applications in robotics. This results in several printable devices, including crawling robot and origami swimmer. The concept regrading oscillator incorporation of multistable mechanisms and conductive actuators lays the foundation of printable mechanical autonomy and inspires other printable control, sensing mechanisms, and well beyond in the following chapters.

In chapter 3, to model and rapidly design the printable oscillator introduced in Chapter 2, I first describe the oscillator dynamic system with a simplified, quasi-static model, whose validity is verified by time constant comparison. Then I derive an analytical formula for the oscillator's behavioral characteristics, i.e., its oscillation period, as a simplified expression of the design parameters. Based on this expression, I formulate the design of a printable oscillator from behavioral specifications into an optimization problem that maximizes its robustness to manufacturing tolerances. This is demonstrated by an example case study. This rapid design methodology can also be expanded to serve as a design tool for other devices with similar structures. For example, this method is applicable to the origami multiplexed switches and logic gates introduced in Chapter 4.

In Chapter 4, we further create origami logic gates and sensors, which enables the integration of robots that can autonomously interact with their environments through sense-decide-act control loops. The enabling technology is an origami multiplexed switch (OMS), which can select between two input signals and forward the chosen one based on a selection signal, functioning as a mechanical analog of the electronic transistor. Based on OMSs and

their derivatives, I have built several autonomous origami robots, including a flytrap-inspired robot that can distinguish and capture 'living prey' from inanimate stimuli, a crawler that can autonomously detect obstacles and execute decision-making to reverse its crawling direction, and an untethered wheeled car that can locomote along reprogrammable predesigned trajectories. The capability of autonomous interaction represents a major step toward highly integrated and robust untethered origami robots and intelligent machines.

In Chapter 5, all the results and findings presented in this thesis are summarized and concluded. I also briefly discuss future research towards fully printable untethered, autonomous robots.

CHAPTER 2

Printable Oscillators

This chapter has been partially adapted from two conference article (1) and (2), and two journal papers (3) and (4). The text of the publication was modified to fit within the format of the thesis, and the supplementary information of the publication integrated into the main text.

(1) **Wenzhong Yan**(✉), Angela L. Gao, Yunchen Yu, and Ankur Mehta. "Towards Autonomous Printable Robotics: Design and Prototyping of the Mechanical Logic". *International Symposium on Experimental Robotics*, pp. 631-644, Buenos Aires, 2018.

(2) **Wenzhong Yan**(✉), and Ankur Mehta. "A Crawling Robot Driven by A Folded Self-Sustained Oscillator". *IEEE International Conference on Soft Robotics*, pp. 455-460, Edinburgh, U.K., 2022.

(3) **Wenzhong Yan**(✉), and Ankur Mehta. "Towards One-Dollar Robots: An Integrated Design and Fabrication Strategy for Electromechanical Systems". *Robotica*, 41 (1), 2020.

(4) **Wenzhong Yan**(✉), and Ankur Mehta. "A Cut-and-Fold Self-Sustained Oscillator for Autonomous Actuation of Origami-Inspired Robots". *Soft Robotics*, 9 (5), 2022.

2.1 Introduction

Driven oscillation is a simple yet efficient strategy for periodic actuation, especially locomotion. However, generating these oscillations typically requires bulky rigid components or electronic control units, restricting origami machines' full potential of being completely foldable. Here we describe a class of origami-inspired oscillators that induce linear oscillation using a constant electrical power source, without the need for electronic controls. These oscillators are foldable, lightweight, low-cost, electronic-free, and nonmagnetic. The oscillator consists of a pair of self-opening switches; these feature a configurable timed delay effect and can serve as one-shot actuators with instantaneous large geometrical changes. The oscillation arises from the systematic coupling of the components such that the opening of one switch automatically resets the other (see Fig. 2.1). The resulting mechanical oscillation admits many potential applications, which we demonstrate with (i) fluid stirring, (ii) LED flashing, (iii) directional crawling of an origami walker on ground, and (iv) gliding of an origami swimmer on water. Our oscillation mechanism offers an approach of realizing simple control functions directly into origami structures; this work paves the way for realizing fully foldable autonomous origami robots with a high integration of actuation, control, and locomotion.

2.2 Mechanism and Design

2.2.1 Self-Opening Switches

The key mechanism generating these foldable design is a self-opening switch. This switch derives its operation from a precompressed bistable (buckled) beam with two stable equilibrium states coupled to a conductive super-coiled polymer (CSCP) actuator [17] (see Fig. 2.3 for detailed fabrication process). When supplied with an electrical current as presented in Fig. 2.1B and C, this switch functions as a normally-closed timer [77]. Initially, the switch is in the unactuated state with the biased contact closed (Fig. 2.1B). The actuator

gradually increases its temperature by Joule heating, resulting in an applied force on the bistable beam. When the displacement of the beam exceeds a given displacement threshold $w_{\text{snap-thru}}$, the beam experiences snap-through, triggering a rapid transition between bistable states and leading to the opening of the electrical connection of the biased contact (Fig. 2.1C). Therefore, this is an self-opening switch characterized by a timed delay. Potentially, this switch could be desired as an actuator in applications where controllable actuation duration or instantaneous large geometrical changes are required [78, 79]. Before starting the next operation, the switch needs to be reset with the bistable beam toggled back to the state 1 and the actuator cooled down to environment temperature. The operating frequency of this switch is typically limited by the latter, needing cooling time T_{cool} to reset the CSCP actuator.

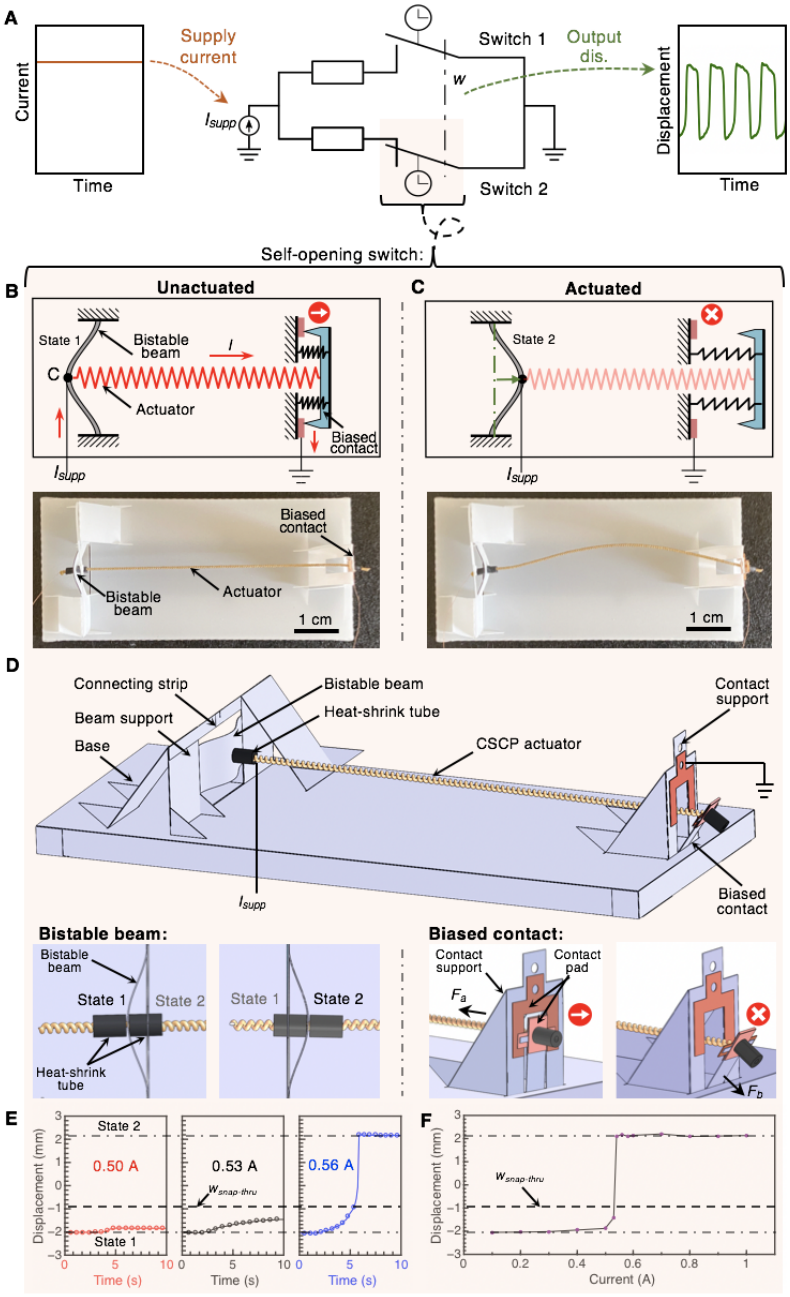

Figure 2.1: A printable oscillator. (A) An oscillator is composed of two switches in parallel with their poles linked. The mechanism of the oscillator with the unactuated state in (B) and the actuated state in (C). (D) The structure of the switch. (E) Time-resolved displacement of the centerpoint C of the bistable beam. (F) Stable displacement of centerpoint after actuation as a function of the supply current.

Thus, the self-opening switch is composed of a bistable buckled beam, a CSCP actuator, and a biased contact connected in series (Fig. 2.1D, with detailed fabrication process in Fig. 2.4 and 2.5). One end of the actuator is connected to the biased contact, whose other terminal is electrically grounded; the other end is attached on the bistable beam and connected to a current supply, I_{supp}. Due to the axial displacement constraints, the originally straight beam decreases in length by being compressed; it then buckles into a cosine-wave shape after reaching a compression threshold, resulting in a bistability. The beam does not require power to remain in either unactuated or actuated states, although switching between states does require energy. When the beam, at state 1, is driven rightwards by the actuator to a critical displacement, $w_{\text{snap-thru}}$, it will snap to its state 2 (Fig. 2.1C); it can be reset to state 1 (Fig. 2.1B) with a critical displacement leftwards, $w_{\text{snap-back}}$.

The delay of the switch is determined by the time needed to for the actuator to heat up sufficiently to initiate the bistable beam's snap-through. To demonstrate the self-opening mechanism, we built a prototype device. As shown in Fig. 2.1E, the bistable beam cannot reach the threshold displacement at low supply currents—the resulting equilibrium temperature and thus drive force in the CSCP actuator is too low. Once the drive current surpassed a threshold, the actuator was then able to drive the beam pass its threshold causing snap-through into state 2 (Fig. 2.1F). Increasing the supply current further beyond this threshold reduces the time needed for the actuator to heat up to its critical temperature and thus the time delay of the switch, increasing the operating speed of the device.

2.2.2 Oscillators

The foldable linear oscillator consists of two aforementioned self-opening switches connected mechanically and electrically (Fig. 2.1A). The two switches connected electrically in parallel (i.e.,, with the same current supply connections) mechanically couple opposing unactuated and actuated states respectively. To generate oscillation, we mechanically linked the two switches' poles forming a double pole, single throw switch. To physically implement this

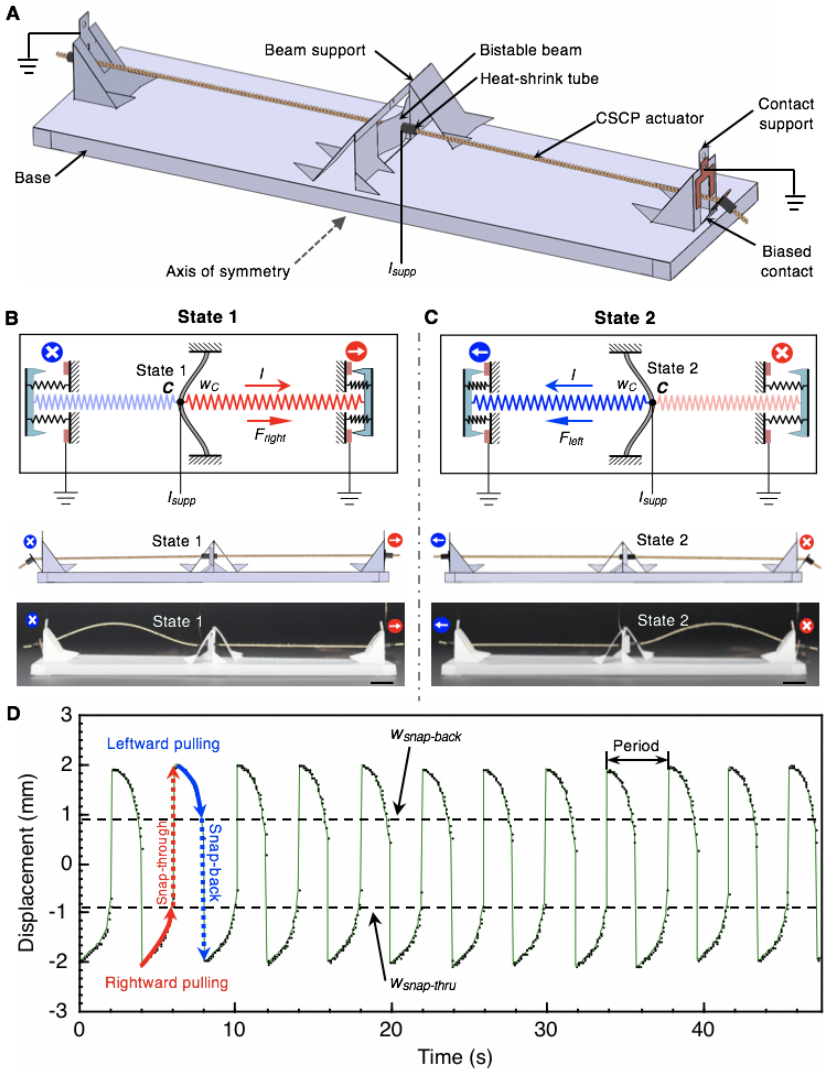

Figure 2.2: Oscillation of a printable oscillator. (A) The oscillator is created by combining two switches in a head-to-head configuration with a shared bistable beam; the actuated state of one switch is coupled to the unactuated state of the other (B) and vice versa (C). (D) The two-switch oscillator generates an oscillating output motion when a constant current power supply ($I_{\text{supp}} = 0.60$ A) is applied. Scale bar, 1 cm.

mechanical linkage, the two switches can be integrated by sharing the same bistable beam leading to a simpler configuration (Fig. 2.2A, see Fig. 2.6 for fabrication details). The motion of the timed opening of one switch will automatically reset the other (back to the

unactuated state, still needing to cool down the actuator). Thus, no stable state exists for this system composed of two connected switches; a system-level instability is built up as the switches close and open sequentially and asynchronously, each shifted by 180° in phase (Fig. 2.2, B and C). This system-level instability results in periodic linear oscillation of the displacement of the centerpoint C of the bistable beam with a minimal unstable transition period (Fig. 2.2D) [54].

To demonstrate, a foldable linear oscillator is fabricated with two integrated identically designed self-opening switches (Fig. 2.2A). The mechanical structure is made from commercially available flexible DuraLar$^{\text{TM}}$ Polyester Film and conductive yarn, with $w_{\text{snap-thru}}$ $\approx$ -0.89 mm and $w_{\text{snap-back}} \approx 0.87$ mm, and supplied with a constant electric current power ($I_{\text{supp}} = 0.60$ A). In order to reduce the reset time T_{cool}, a forced air source is supplied. After about 3 initial transient cycles, the oscillator started to generate a stable periodic oscillation of the output displacement of the midpoint C of the bistable beam with oscillation period, $T_{\text{osc}} = 3.93$ s, calculated by averaging its peak-to-peak periods in the time-displacement curve (see Fig. 2.2D). Each oscillation consists of four phases: rightward pulling, snap-through, leftward pulling, and snap-back (Fig. 2.2D). The snap-through and snap-back phases are significantly faster than the pulling phases: in this case the snap-through time was $T_{\text{snap-thru}} \approx$ 0.12 s (3.1% of the period) and snap-back time was $T_{\text{snap-back}} \approx 0.10$ s (2.5% of the period).

We further investigated the envelope of the foldable linear oscillator design. We varied the input current and found out the shortest oscillation period was about 3.15 s when the current reached 0.63 A. Beyond this value, oscillation could not be sustained as the actuators could not cool down between periods. However, we could reduce the oscillation period further, achieving down to 0.34 s, by using active cooling to speed the thermal reset. This observation provides us a methodology to increase the oscillation frequency for certain applications. We also explored the possibility of the oscillator working in different environments. Firstly, we submerged the oscillator completely under water; the oscillator was able to oscillate with a period of around 1.21 s from a 1.58 A supply; this could be used as an actuator

for underwater robots leading to a new application domain for origami-inspired designs. Secondly, we placed the oscillator into a strong magnetic field of 180 mT (about 4000 times Earth's field). The oscillator was unaffected by either constant or dynamic magnetic fields, demonstrating the potential of this oscillator for actuation within otherwise challenging high magnetic environments such as Magnetic Resonance Imaging (MRI) systems (with fields of 0.5–3 T).

2.3 Printable Fabrication and Assembly

We use the foldable, self-opening switch as an example to demonstrate the fabrication method. The fabrication of foldable linear oscillator and other robots (see Section 2.4) shares a similar process, which can be found in Section 2.5.1. The fabrication of the switch consists of three consecutive steps: (i) CSCP actuator creation; (ii) origami cut-and-fold and (iii) assembly with actuator and contact pads.

2.3.1 CSCP Actuators

The CSCP actuator was formed by using commercially available conductive yarn (235-34 4ply HCB, V Technical Textiles Inc.) with a diameter of about 0.4 mm. These actuators were prepared by following three steps (Fig. 2.3): (i) inserting coils by continuously twisting the conductive yarn under tension, (ii) annealing the coiled yarn with a cycling heating/cooling process under tension, and (iii) stabilizing the actuator by repeating the heating/cooling cycles without tension. Specifically, the conductive yarn was twisted by a stepper oscillator (XY42STH34-0354A, Guangzhou Shenglong oscillator Co. Ltd.) under a 0.28kg weight until it formed coils. The weight was free to move vertically but not allowed to rotate. The coiled yarn was then de-stressed by a 8-hour annealing process (0.45A annealing current, 30 s heating and 30 s cooling per cycle) under the same weight. Lastly, the actuator was released from the pretension and treated by a heating/cooling process (0.27 A stabilizing

current, 10 s heating and 10 s cooling per cycle) for 5 min to stabilize the strain (about 3% in our case). The obtained actuator has an average diameter of 0.71 mm.

As tested, the slope of the force-displacement curve and therefore the mean stiffness of the 50-mm-long actuator, was measured to be 0.38 N/mm. In addition, the mean slope of the curve is the thermal coefficient, $c_T \approx 1.6\times\ 10^{-2}$ N/°C [17].

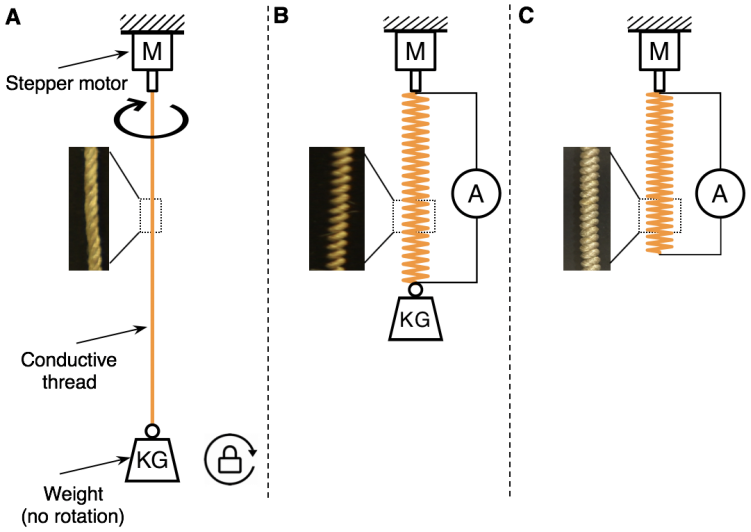

Figure 2.3: Fabrication of the CSCP actuator. (A) Coils insertion. The conductive yarn was pretensioned by a weight and then twisted by a stepper oscillator until coils were formed. (B) Annealing process of the coiled yarn. The coiled yarn was periodically heated/cooled to release the twisting stress, resulting in a CSCP actuator. (C) Stabilization process of the actuator. The weight was removed and the actuator was treated by a similar heating/cooling process to stabilize the strain.

2.3.2 Origami Components

We fabricated the origami frame of the switch by patterning a flexible, polyester film (DuraLar^{TM}, Grafix Plastics) with a cutting machine (Silhouette CAMEO 2, Silhouette America, Inc.) with parameters set to 100% blade depth, 40% speed, and 90% force (Fig.

2.4). The cutting lines were 100% cut in length and dashed lines were 50% cut in order to make it easier to fold and while maintaining enough strength to hold its shape. The 2D fabrication pattern of the switch is shown in Fig. 2.4A, where red dashed lines mean mountain folds and blue dashed lines represent valley folds. Essentially, the out-of-plane structures are created in a manner similar to weaving: the out-of-plane structure is formed by making the strip-like peripheral structure go through the slot from the backside of the base. For example, the strip-like pattern of the biased contact is bent downward and comes out from the contact support slot on the base (Fig. 2.4B). The connections between origami structures were reinforced by double-rib tabs, which were designed to precisely align the connected structures, and further served to stiffen the overall structure (Fig. 2.4B). Simple tabs were used for small-dimension structures where double-rib tabs would otherwise not fit. Thus, by using origami features as connectors, we can include self-alignment while minimizing resources required to assemble the devices. The bistable beam was precisely formed and constrained through three steps: (i) z-shape folding, (ii) sidewall confinement, and (iii) pulling constraint. The z-shape folding pattern (Fig. 2.4C) resulted in the prescribed compression on the beam by decreasing its axial span. Then the beam was fed through the beam slot on the base (Fig. 2.4B); the sidewalls of this slot provide an additional equal constraint on the length of beam (Fig. 2.4C). Connecting strips with notches were then used to constrain the other end of the buckled beam's width, giving rise to the final form of the desired bistable beam (Fig. 2.4B).

2.3.3 Assembly

Then we assembled the electrical design of the switch in two main steps, as shown in Fig. 2.5. (i) The two patterned contact pads (laser-cut copper tapes), i.e., a U-shaped pad and a T-shaped pad, were aligned and attached to the static pole and the biased pole of the contact, respectively, to form the biased contact circuitry (Fig. 2.4B). (ii) One terminal of the CSCP actuator was fixed to the beam by using a piece of heat-shrink tubing (7496K81, Insultab)

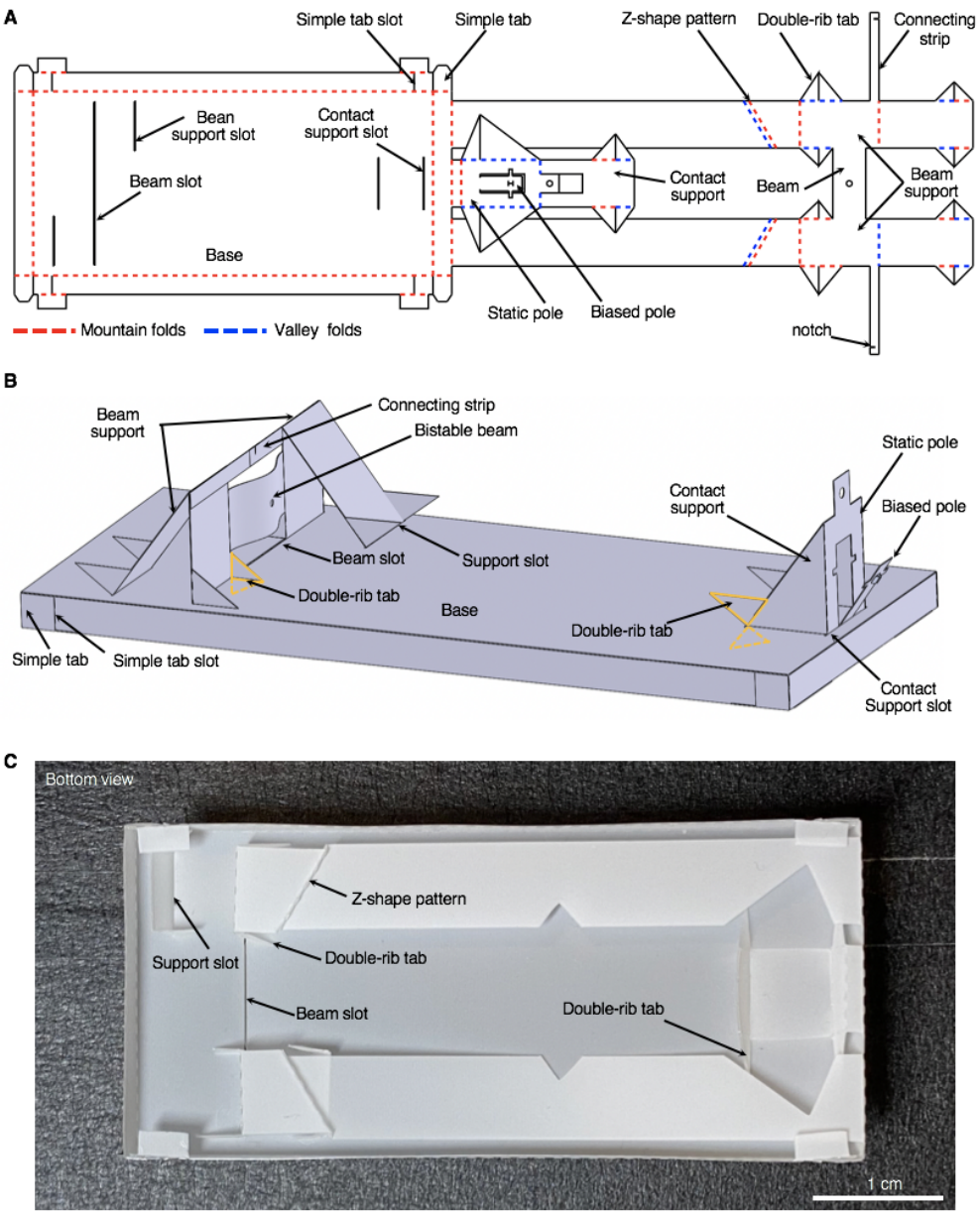

Figure 2.4: Fabrication of the origami frame of the self-opening switch. (A) 2D pattern of the origami structure. Red dashed lines represent mountain folds and blue lines are valley folds. (B) 3D folded origami structure of a self-opening switch at unactuated state with labels. (C) Bottom view of the switch.

on either side. The other terminal of the actuator was similarly fixed to the biased pole of the contact through another heat-shrink tube, additionally forming a electrical connection between the actuator and the T-shaped contact pad. Thin copper wire was used to connect these two terminals to improve the electrically connection. Thus, an actuator—T-shaped pad—U-shaped pad current path is formed when the switch is powered (Fig. 2.1B). It's worth noting that the mechanical contact between the two poles must be ensured to guarantee electric connection when switch is in its unactuated state (Fig. 2.1B and D).

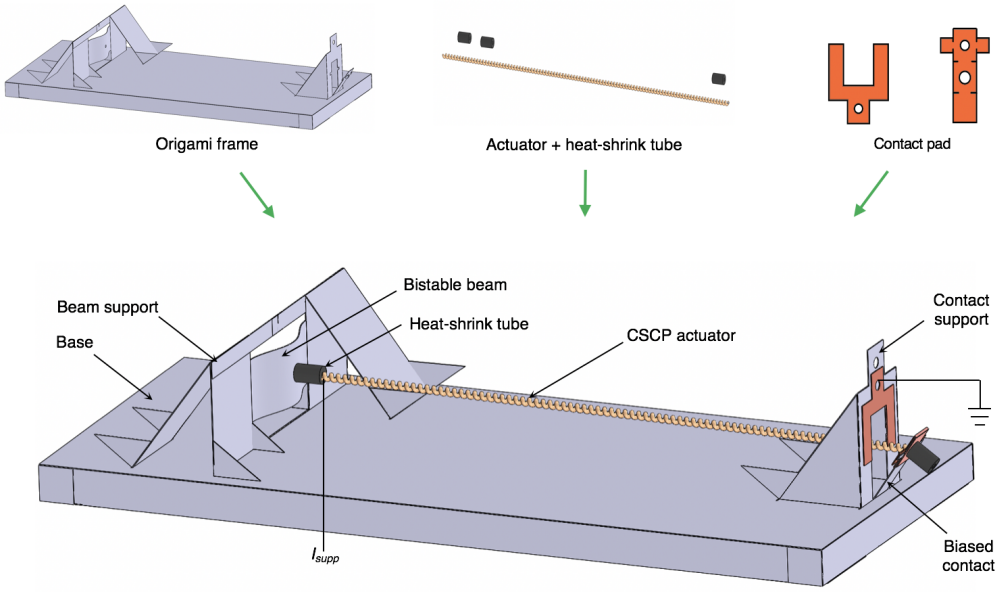

Figure 2.5: Assembly of the self-opening switch. The U-shaped and T-shaped contact pads were aligned and attached on the biased contact's static pole and biased pole, respectively. Then the actuator was assembled with its left terminal fixed to the bistable beam and its right terminal fixed to the T-shaped contact pad on the biased pole of the contact switch. The right connection forms both a mechanical connection as well as an electric connection between the actuator and contact pad. Both connections were secured by using heat-shrink tubing (7496K81, Insultab).

The fabrication of the foldable linear oscillator shares a similar process to that of the foldable switch. The oscillator could be treated as two symmetrically jointed switches by

sharing the same bistable beam. The corresponding 2D fabrication pattern is shown in Fig. 2.6A, where the pattern in dashed box is the added biased switch from the second self-opening switch (without its bistable beam). Hence, we follow the same procedure steps as above to fabricate the oscillator, using the similar components (Fig. 2.6B) to manufacture our linear oscillator symmetric about the bistable beam (Fig. 2.6C). The mixer, low-frequency flapper, LED display controller, origami walker, and swimmer were all developed on the basis of the linear oscillator and thus fabricated by the same procedure with minor modifications.

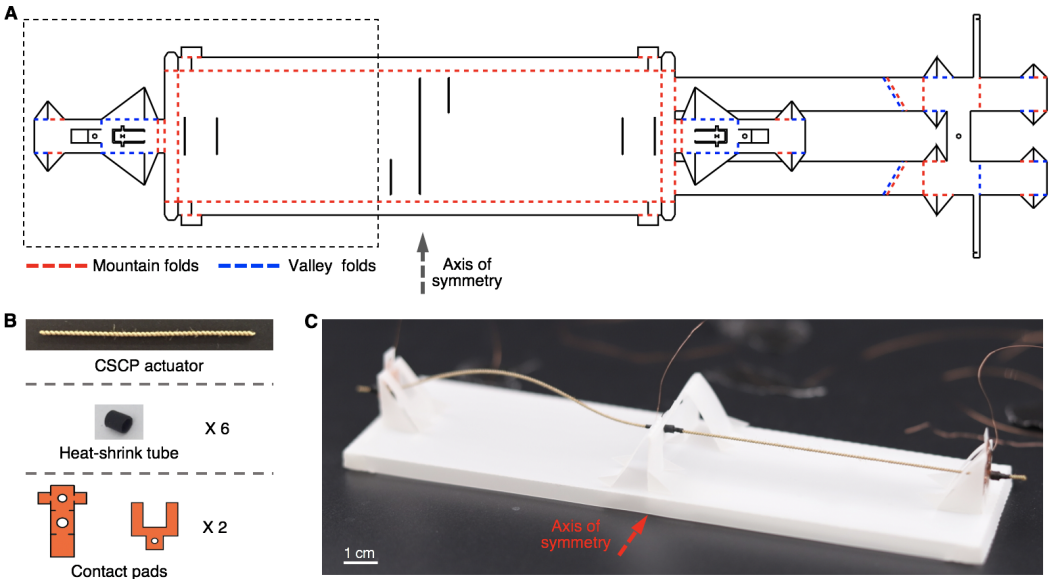

Figure 2.6: Design and assembly of the printable oscillator. (A) 2D pattern of the origami frame. Red dashed lines represent mountain folds and blue lines are valley folds. The pattern in the dashed box is newly added on the basis of the design of the self-opening switch, as shown in Fig. 2.5. (B) A list of essential components for the oscillator assembly. (C) Assembled printable oscillator, which is symmetric about the bistable beam.

2.4 Oscillation-Driven Applications

To demonstrate the ability of the foldable linear oscillator to drive motion using only a single, constant current input, we proposed four applications built on our design: mixing

fluid through the oscillatory dragging of an agitator actuated by the oscillator (Fig. 2.7), animating an LED display using the periodic motion of the oscillator to control electrical circuits (Fig. 2.8), powering an origami walking robot under asymmetric friction using a driven reaction mass to generate inertial forces (Fig. 2.9), and propelling an origami swimmer on water utilizing a rotary paddle driven by the linear oscillation of the oscillator (Fig. 2.10). The fabrication and assembly of these origami robots can be found in Section 2.5.1

2.4.1 Fluid Stirring

We first demonstrated the ability of the foldable linear oscillator to deliver oscillatory actuation: we controlled the motion of an agitator of a foldable mixer for stirring and mixing fluid [80]. The agitator is attached centrally on the bottom of the bistable beam through a connector—a narrow origami hinge (Fig. 2.7A). Thus, no additional fastening agents are needed; the mechanical subsystem of the mixer can be fabricated through a single piece of polyester film (DuraLar^{TM}, Grafix Plastics) sheet. The agitator has relatively large area and is orientated perpendicular to the oscillation path of the bistable beam to increase the drag force in fluid and hence, the stirring ability. Correspondingly, a opening underneath the bistable beam is created to allow a direct contact of the agitator with the fluid. Once a constant current power is supplied, the mixer can disturb the fluid driven by the periodical snap-though and snap-back motions of the bistable beam.

We mixed water with blue dye using this mixer (Fig. 2.7B). The mixer was attached on the top of a shallow water tank (150 mL); the agitator was submerged into water to maximize the stirring capability. Before the power supplied, 0.1 mL blue dye was injected into the water and rested for some time to exclude the effect of other factors (e.g., diffusion) that may result in dye mixing. The dye stayed heterogeneous even after around 120 s. Qualitatively, Fig. 2.7C shows that mixing by using the mixer can achieve a homogeneous solution (i.e.,, the dye is dispersed throughout the water) within the next 120 s. The fluid need not be

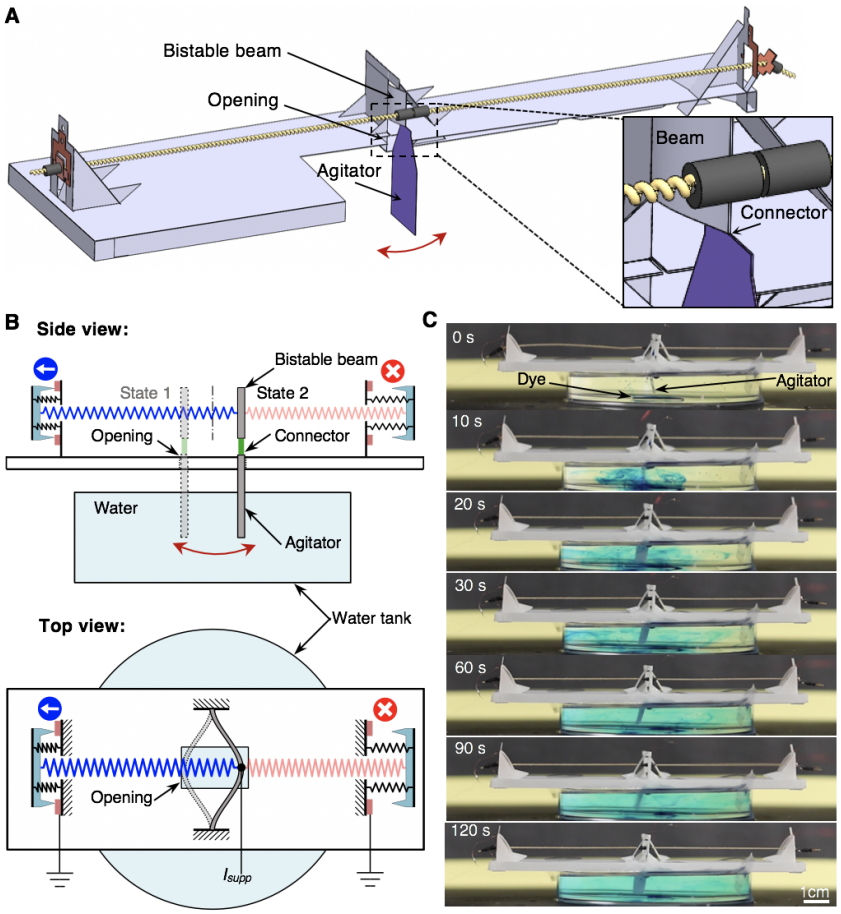

Figure 2.7: Stirring and mixing of fluid. (A) The 3D rendering of the mixer. On the basis of the oscillator, an origami agitator (in purple) is attached on the bottom edge of the bistable beam through an origami hinge. (B) The mechanism of the stirring. The mixer is fixed on the top of a water tank. The agitator is driven by the bistable beam to disturb the fluid (top: side view; bottom, top view). (C) The blue dye is injected into water and rests for about 120 s before the stirring. Once a constant current power is supplied, the oscillation of the bistable beam drives the mixer stirring the water to achieve fluid mixing in 120 s.

a liquid: by similarly attaching a wing on the bistable beam, we could instead generate low-frequency flapping, which can presumably be used to deliver gas flow while stirring [80].

2.4.2 LED Flashing

In addition to oscillatory actuation, the linear oscillator can generate sequential electrical control. We controlled the on/off states of two LED circuits resulting in the controlled animation of the light arrays. On the basis of the linear oscillator, two LED arrays are incorporated into the system by connecting their cathodes at point a and b, respectively (Fig. 2.8A). The LED light arrays can be supplied with independent power (i.e., V_{LED}). Therefore, the states of two LED arrays are only controlled by the open/closed status of the corresponding self-opening switches.

Here, we integrated the two LED arrays into an LED panel composed of 49 green LED (Fig. 2.8B). This LED panel has two different light patterns (Fig. 2.8C). When switch 1 is closed, the LED panel shows pattern 1; respectively switch 2 and pattern 2. V_{LED} is about 5.1 V and is independent of the controllable oscillator supply current. Once the linear oscillator is powered, the LED panel switched between pattern 1 and 2 leading to the designed animation of a stick figure walking. When the supply current to the linear oscillator was increased (at around t=6 sec), its oscillation frequency increased (Fig. 2.8D), animating the figure to walk faster and then run.

2.4.3 Directional Crawling

We also demonstrated the ability of the linear oscillator to achieve translational locomotion of origami robots by using only a constant current input, with two applications. The first application is to drive an origami oscillation-enabled robot to crawl on ground by harnessing the symmetric oscillation of the oscillator under asymmetric friction [10, 81]. Building on the linear oscillator, we attached two one-gram masses (tin balls) beside the bistable beam, as well as four angled legs on its edges (Fig. 2.9A). These masses are used to improve the transmission efficiency from the potential energy of the bistable beam to the kinetic energy of the robot to increase its locomotion speed. The two masses were evenly distributed on

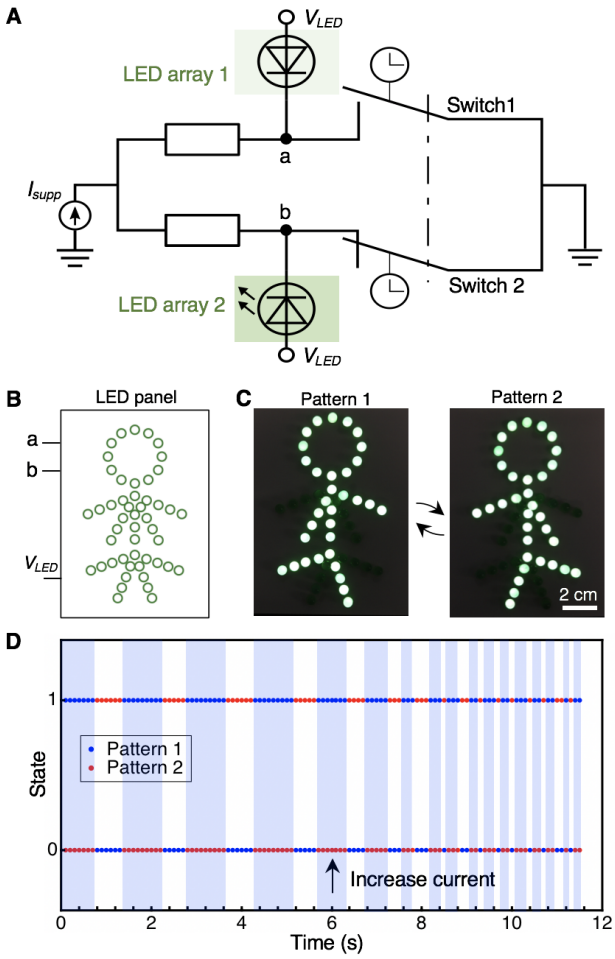

Figure 2.8: Animation of an LED display. (A) The schematic of the circuit. The two LED arrays are integrated into a panel with a stick-figure pattern with three terminals, namely a, b, and power supply pin (B) (see Fig.2.12C and D for detailed circuit design). (C) Two different lighting pattern of the LED panel. (D) Once the linear oscillator powered with a constant current, the LED panel (supplied with a 5.1V power source) starts to flash, alternating between pattern 1 and pattern 2.

the both sides of the bistable beam to reduce the asymmetry of the resulting robot. Each leg contacts the ground with an angle of around 45°, along with a brush-like-shape design, to generate a large difference in the directional coefficients of friction to enable forward locomotion [81].

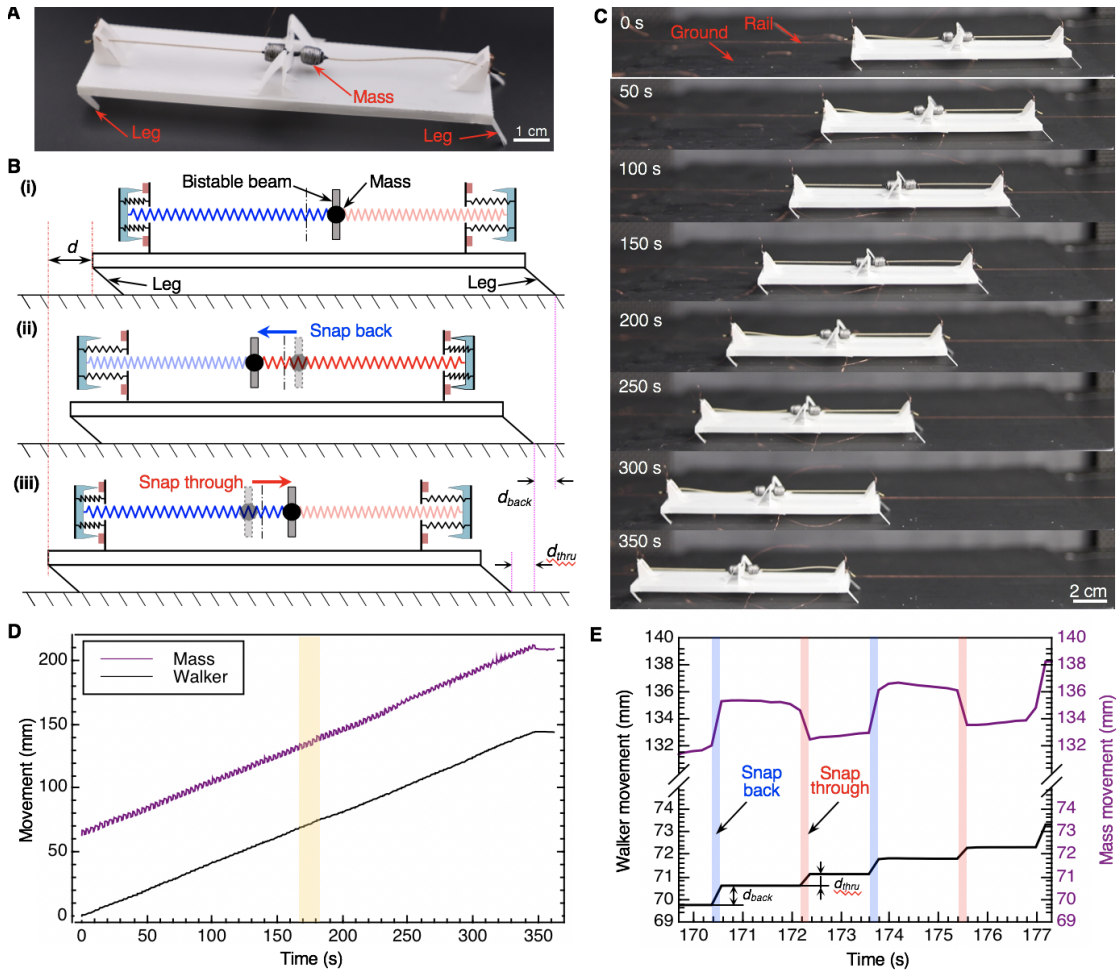

Figure 2.9: Crawling of an origami walker. (A) The walker is composed of a linear oscillator, four legs (45° against the ground), and two one-gram masses. (B) Simplified walking mechanism of the walker. (C) The walker marched leftward along a rail designed to guide its direction. (D) Time-resolved plots of the displacement of the right-hand-side mass and walker over time. (E) Detailed movement traces from 170 s to 177 s of (D).

The mechanism of this walking robot is described in Fig. 2.9B in two steps. In the first step, from state (i) to (ii), the bistable beam (and attached mass) snaps back (leftward in the figure). When the beam comes to rest, the kinetic energy of the mass is delivered to the robot, driving it leftward by a distance, d_{back}. For the second step, from state (ii) to (iii), the walker moves further leftward by another distance, d_{thru} due to the reaction from the

bistable beam snap-through to the right. The corresponding rightward motions in each step are suppressed due to the asymmetric friction against the surface condition of the selected terrain—a polyvinyl chloride cutting mat (10671, Dahle Vantage)—and the unique transient impact-induced actuation from the snap-throughs. Thus, the robot can move leftward by a distance, $d(= d_{back} + d_{thru})$, in one oscillation cycle.

The coefficients of friction in two directions are measured as 0.36 (leftward) and 0.72 (rightward). The origami walker can monotonically march 146.0 mm in 350.1 s, achieving an average speed of about 0.42 mm/s, with the attached mass oscillating about that moving centerpoint (Fig. 2.9C and D). We further zoomed in the movement curves from 170 s to 177 s, validating that the driven back-and-forth oscillation of the linear oscillator is capable of realizing monotonous directional locomotion for origami robots (Fig. 2.9E). We also notice that the crawling of the robot only happened when the snap-through (or snap-back) motion occurred, validating the transient impact-induced locomotion mechanism of the walker.

2.4.4 Gliding on water

Besides the symmetric oscillation-enabled locomotion, we designed a foldable swimming robot (Fig. 2.10A) that can glide on water surface by harnessing the periodic rotational propulsion of a paddle [13]. This rotational propulsion is generated through a special mechanism that guides the paddle travel through an asymmetric stroke driven by the symmetric oscillation of the bistable beam. The swimmer is built upon the foldable linear oscillator with additional integrated origami features (see Fig. 2.10B). We added four stabilizers around the oscillator and one paddle onto the bottom edge of the bistable beam. The stabilizer has three functions: (i) to balance the swimmer to avoid rolling; (ii) to control the gliding direction via vertical fins; (iii) to reduce friction against the sidewalls (if necessary) via horizontal bumpers. The L-shaped paddle is connected with the bistable beam through a flexible connector and constrained by a narrow hole on the body. The flexible connector joint enables the angular movement of the paddle while being compatible with the origami-

inspired manufacturing method. Additional features are added onto the edges of the paddle to increase the propulsion force in water and thus, the thrust ability.

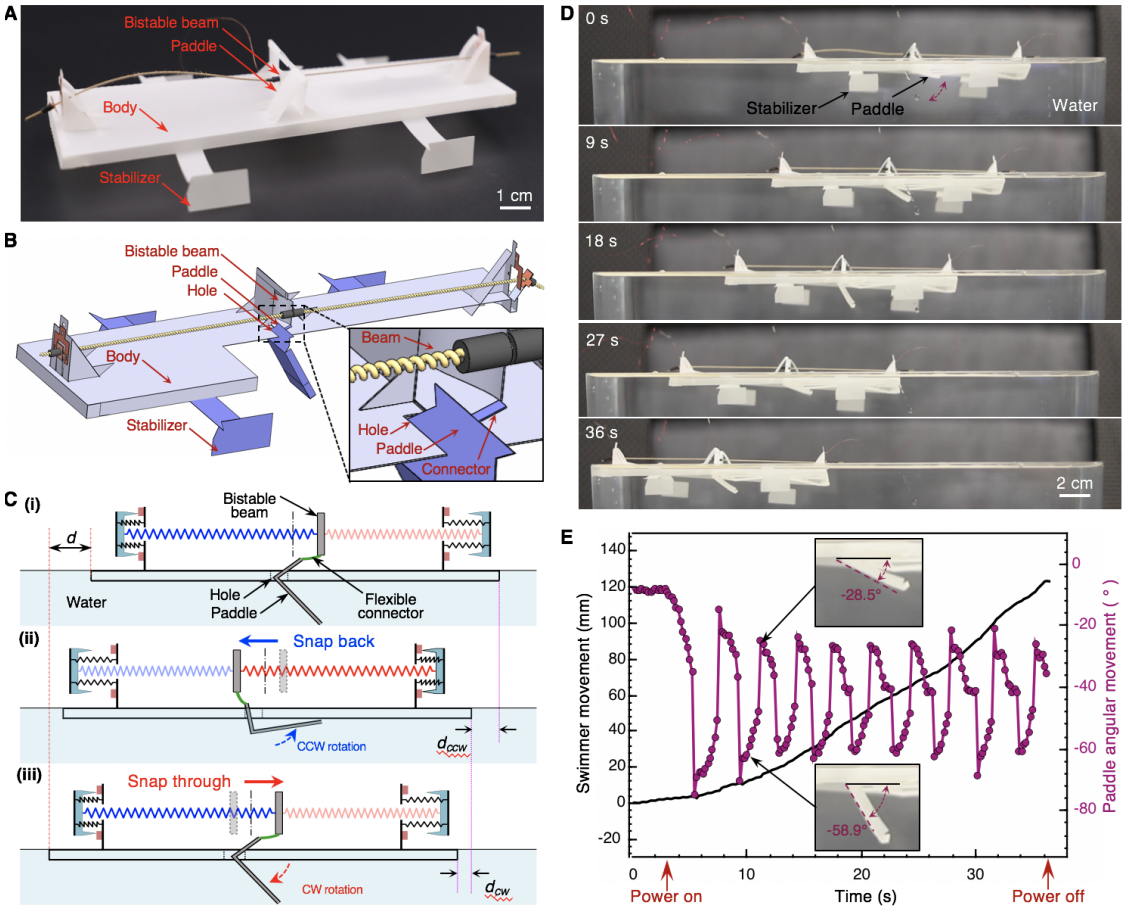

Figure 2.10: Gliding of a folded swimmer on water. (A) The swimmer consists of an oscillator, four stabilizers, and one L-shaped paddle. (B) The stabilizers and paddle (in purple) are added onto the edges of the oscillator and the bottom edge of the bistable beam, respectively. (C) Simplified locomotion mechanism of the swimmer. (D) Power was supplied after about 3-seconds; the resulting oscillation of the oscillator drives the rotational motion of the paddle to propel the swimmer leftward over the water surface. (E) Time-resolved plots of the (angular) displacement of the swimmer and paddle.

It is worth noting that all of the newly added components (including four stabilizers, one

paddle, and the flexible connector) are fabricated by the same origami-inspired method as the foldable linear oscillator are thus integrated into a monolithic design. In other words, the mechanical subsystem of the foldable swimmer can be directly made out of a single sheet material. This monolithic design and fabrication strategy improves the robot's simplicity and hence, reduces the manufacturing complexity and cost.

Once the power is supplied, the paddle generates thrust on the swimmer in two steps (Fig. 2.10C). In the first step, from state (i) to (ii), the bistable beam snaps back (leftward in the figure) driving the paddle counter-clockwise (CCW) to propel water, which results in a leftward gliding of the swimmer by a distance, d_{ccw}. In the second step, from state (ii) to (iii), the bistable beam snaps through (rightward in the figure) and thus the paddle rotates clockwise (CW), thrusting the swimmer leftward by another distance, d_{cw}. Therefore, the robot can swim leftward by $d(= d_{ccw} + d_{cw})$ in one cycle. Over time, the swimmer can continuously glide on water surface only with a constant current supply.

We experimentally demonstrated the capability of the swimming robot, with an on-board, integrated linear oscillator. After a 3-second's rest, the swimmer was powered by a constant current supply and traveled 120.8 mm in 33.0 s, achieving an average speed of about 3.66 mm/s (0.027 body lengths per second) (Fig. 2.10D and E). Meanwhile, the paddle featured a oscillatory rotational motion (in purple, Fig. 2.10E) driven by the linear reciprocating motion of the bistable beam. Unlike the origami walker, the swimmer glided continuously with the intermittent propulsion from the paddle thanks to the small friction on water.

2.5 Materials and Methods

2.5.1 Fabrication of Origami-inspired Devices

2.5.1.1 The printable mixer and low-frequency flapper

The printable mixer was mainly composed of an oscillator and an origami agitator (Figure 2.7A). The difference of the 2D fabrication patterns of the origami frame compared with that of the oscillator is highlighted by green shadows (Figure 2.11A). Specifically, a flat agitator was attached on the bottom edge of the bistable beam through a narrow origami hinge. Correspondingly, a opening was cut on the base to allow a direct contact of the agitator with fluid underneath.

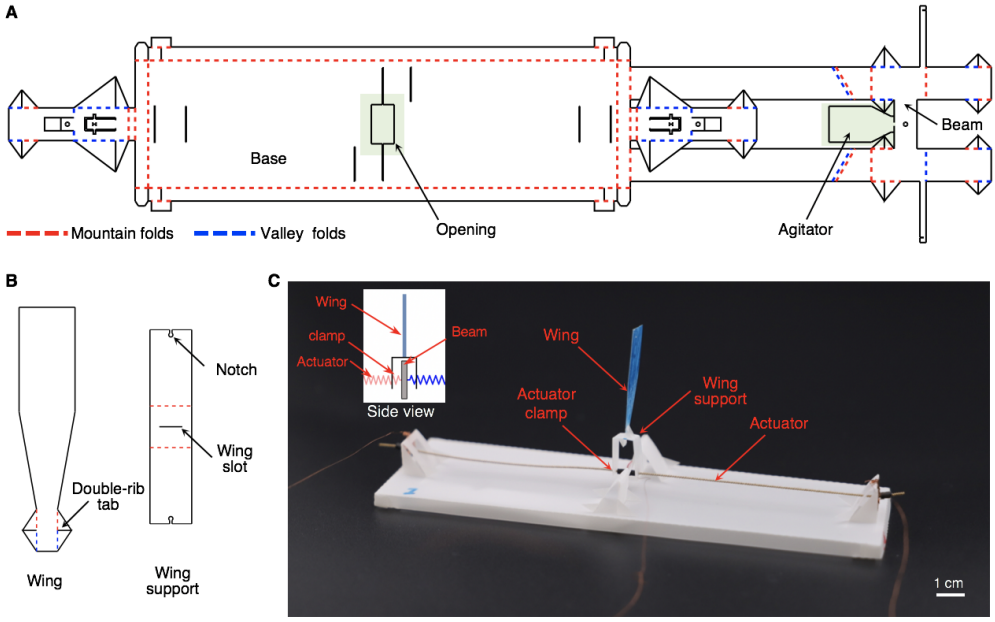

Figure 2.11: Design and assembly of the printable mixer and flapper. (A) 2D fabrication pattern of the origami frame of the mixer. Patterns in green shadow indicate the differences compared with the design of the oscillator. (B) 2D pattern of the wing and corresponding support structures of the flapper. (C) The detailed configuration of the flapper.

On the other hand, the low-frequency flapper was built by adding an origami wing and

its support structure onto an oscillator. The 2D pattern of the wing is shown in Figure 2.11B. Before being attached onto the oscillator, the wing was mounted onto its support by a double-rib tab connecting to the wing slot. Then, the wing support structure was fixed onto the actuator through the Ω-shaped notches at the edge of the wing support (Figure 2.11C).

2.5.1.2 The LED display

The animated LED display had two major components, an oscillator and an LED panel. The LED panel was composed of an origami frame and 49 green LED diodes (diameter: 5 mm, wavelength: 520-525 nm, forward voltage: 3.0-3.2 V). The 2D pattern of the origami frame with tabs to connect origami structures is shown in Supplementary Figure 2.12A. This frame functions as a framing to support the diodes with openings to allow active cooling airflow to go through (Figure 2.12B and E) to the working actuator underneath. The pattern of the LED diodes were divided into three groups (Figure 2.12C) and arranged into a circuit where the parallel connection of group 2 and group 3 was in series with group 1 (Figure 2.12D). The LED panel was placed over the oscillator with its two terminals, i.e., a and b, connected into the circuit (Figure 5A and Figure 2.12D).

2.5.1.3 The printable walker

We equipped an oscillator with four legs and two one-gram masses to construct an origami-inspired printable walker. The four legs were attached on the edges of the oscillator with a 45° angle against the ground (Figure 4.6A). Meanwhile, four rail holes were cut besides the legs. Thin copper wires were threaded through the holes to constrain off-axis forces and guide the locomotion direction (Figure 4.6C). The 2D fabrication pattern of the origami frame of the walker is shown in Figure 2.13A with newly added features in green shadow compared to the oscillator design. Figure 2.13B presents a zoom-in view of the detailed

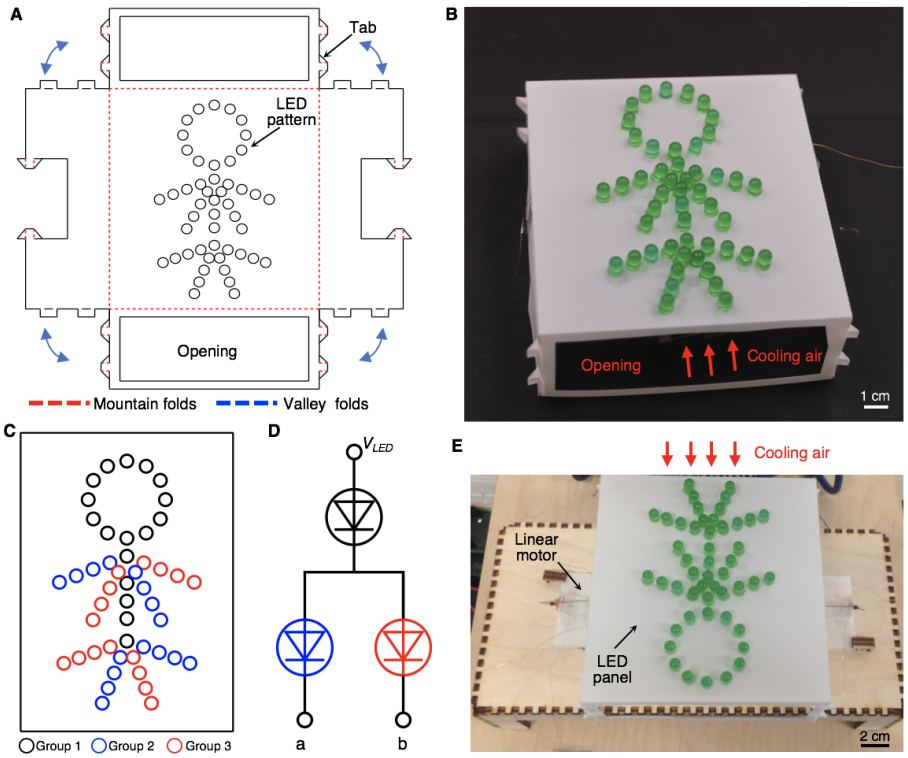

Figure 2.12: Design and assembly of the printable LED display. (A) 2D fabrication pattern of the origami frame of the LED panel. (B) Assembled LED panel with 49 LED diodes. 49 LED diodes were divided into three groups (C) with its equivalent circuit shown in (D). (E) The LED panel was placed above the oscillator with its opening allowing the active cooling air to go through.

features of the leg and rail hole. A brush-like design was adopted for the legs to increase its tip's softness; the increased differentiation of the coefficients of friction in each direction improves the locomotion of the walker. In addition, two masses (tin balls with a central hole) were mounted around the CSCP actuators beside the bistable beam, using heat-shrink tubing to form mechanical stoppers (Figure 2.13C).

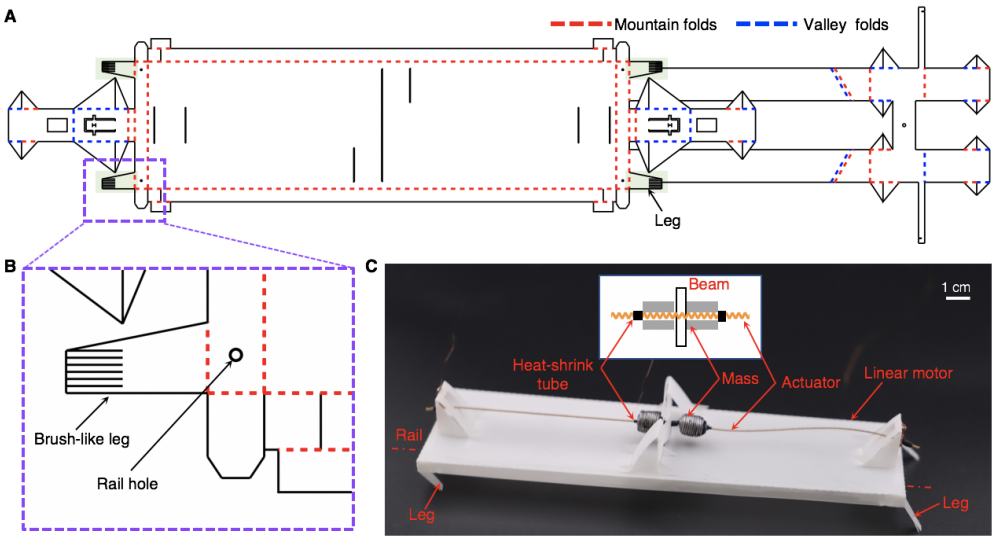

Figure 2.13: Design and assembly of the printable walker. (A) 2D fabrication pattern of the origami frame of the walker with newly added patterns in green shadow on the basis of the design of the oscillator. (B) The zoom-in view of the brush-like legs and rail hole. (C) The detailed structure of the walker with labels.

2.5.1.4 The fully printable swimmer

As shown in Figure 4B, the swimmer consists of an oscillator, four stabilizers and one L-shaped paddle. The corresponding 2D fabrication pattern is presented in Figure 2.14A with all additional components in green shadow beyond the design of the oscillator. A narrow hole was cut parallel to the beam slot to constrain the movement of the paddle to achieve rotational actuation to increase the generated thrust (Figure 4C). The L-shaped paddle was attached to the bottom edge of the bistable beam with a flexible connector (Figure 4B and Figure 2.14B). This connector transmits mechanical displacement from the bistable beam to the paddle. We also created turn-up structures (Figure 2.14B) around the paddle to enhance the dragging ability and thus, propulsion of the paddle. The paddle was designed as a multi-segment structure for manufacturing simplicity: (i) The "L" shape could be formed by folding along the hinge; (ii) The resulting shape could be more easily fed through the

hole during assembly.

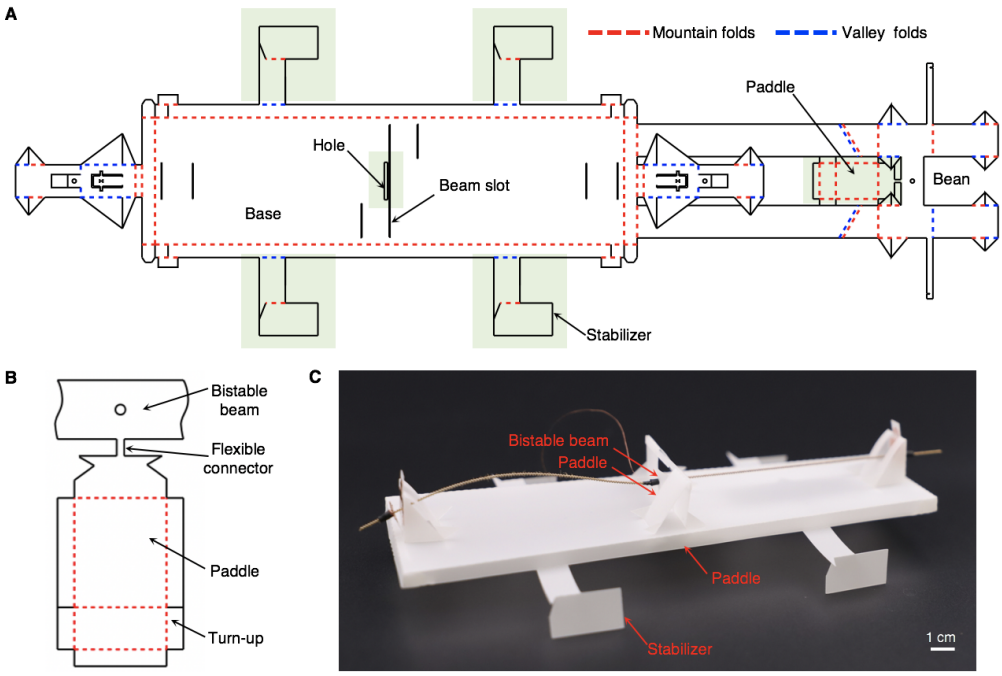

Figure 2.14: Design and assembly of the printable swimmer. (A) 2D fabrication pattern of the origami frame of the swimmer. Newly added features are covered by green shadow to show the modifications to the design of the oscillator. (B) The zoom-in view of the 2D pattern of the L-shaped paddle connected with the bistable beam through a flexible connector. (C) The photo of the swimmer with labels.

2.5.2 Characterization of components

The CSCP actuator

Two properties of the CSCP actuator, namely the stiffness k and thermal coefficient c_T, need to be empirically characterized. k was extracted from the slope of the force-displacement curve [17] obtained by using a Mechanical Test System (UniVert, CellScale). Two ends of the actuator sample (50 mm) were fixed on two plywood mounts (Figure 2.15A). Before assembly onto the Mechanical Test System, a K-type thermocouple (CT-QB-K-0.1, PerfectPrime)

coupled with a thermometer (COMINHKPR146086, Leaton) was attached on the actuator using cyanoacrylate glue (Krazy glue, Elmer's Product, Inc.), as shown in Figure 2.15B. The slope of the force-displacement curve and therefore the mean stiffness of the 50-mm-long actuator, was measured to be 0.38 N mm^{-1} (Figure 2.15C).

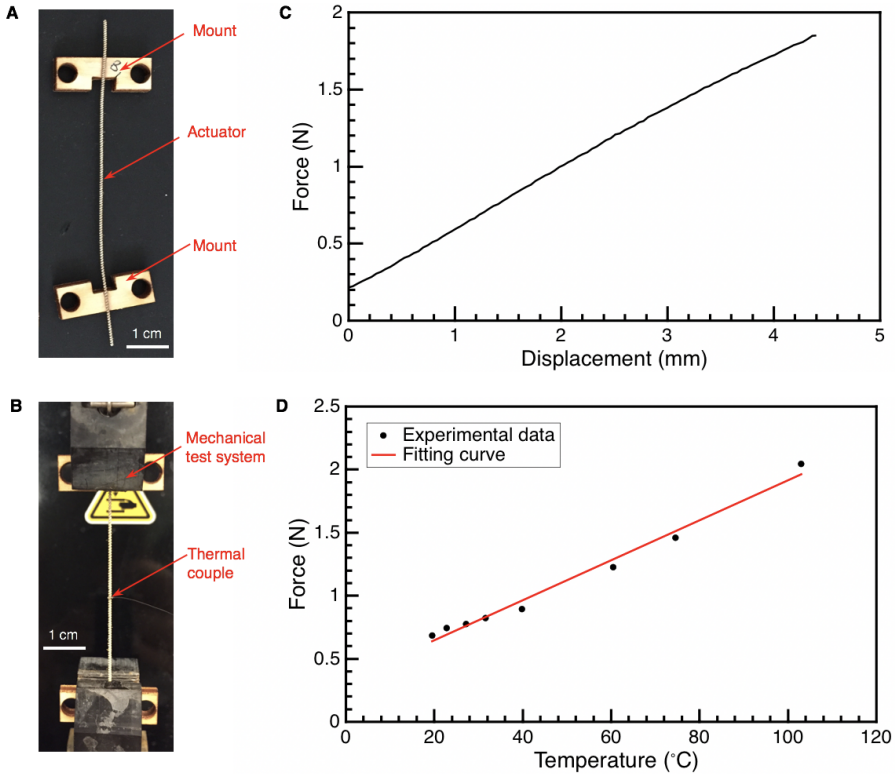

Figure 2.15: Characterization of the CSCP actuator. A testing actuator sample with its two ends fixed on plywood mounts (A). A thermocouple was attached on the actuator (B). (C) The force-displacement curve of the actuator in room temperature. (D) The exerted force of the actuator as a function of its temperature when heated up through Joule heating.

The actuator was heated up through Joule heating with a DC power supply (TP-3003D-3, Kaito Electronics, Inc.). Once the temperature of the actuator was stable, the temperature and corresponding generated force were read and recorded from the thermometer and Mechanical Test System, respectively. Changing the supply power yielded new data points; the resulting temperature-force curve is shown in Figure 2.15D. The mean slope of the curve is

the thermal coefficient, $c_T \approx 1.6\times\ 10^{-2}$ N °C^{-1} [17].

The bistable beam

The bistable beam testing samples were composed of an origami bistable beam (with its origami support structure), a rod, and two plywood mounts. As shown in Figure 2.16A, the rod was attached to the bistable beam through the central hole by using heat-shrink tubing. The other end of the rod was fixed to the bottom plywood mount. Meanwhile, the bistable beam support was glued to the top mount. During the experiment, the Mechanical Test System (UniVert, CellScale) clamped the two plywood mounts. The force-displacement curve of the bistable beam is presented in Figure 2.16B, which indicates the values of the w_{rise}, $w_{\text{snap-thru}}$, and $F_{\text{snap-thru}}$ are -2.12 mm, -0.89 mm, and 0.42 N. It is worth noting that the values of w_{rise}, $w_{\text{snap-thru}}$, and $F_{\text{snap-thru}}$, are converted to the coordinate system as shown in Figure 1D (or Figure 3.1).

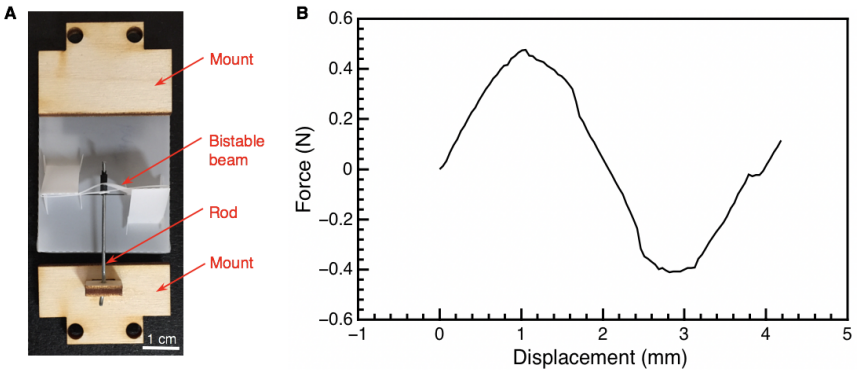

Figure 2.16: Characterization of the bistable beam. (A) A testing bistable beam sample with its two terminals glued onto plywood mounts. (B) The force-displacement curve of the bistable beam.

2.6 Conclusion and Discussion

Previous methods to achieve periodic actuation of origami devices have relied on bulky rigid components, often requiring external control system devices and limiting use in applications where completely foldable robots are desirable or necessary. This paper presents a foldable linear oscillator composed of two self-opening switches. The oscillation of the oscillator stems from two instabilities: the buckling instability of the bistable beam that control the "closed" and "opened" states of the biased contacts of each self-opening switch, and the system-level instability caused by the mechanical coupling of the poles of the two self-opening switches. This printable oscillator outputs periodic linear displacement and enables driving origami robots and mechanisms from only a single constant electrical power supply. Thus, this oscillator empowers oscillatory motions in completely foldable devices, illustrating the feasibility of embedding simple control into the electromechanical constructions, eliminating the need for auxilliary electronic devices through mechanical design. Moreover, this oscillation mechanism can be characterized as a generic physical strategy to convert a constant energy input into an oscillatory output through coupled feedback of time-delayed mechanical instabilities.

We were able to achieve oscillation periods down to approximately 0.34 s; the oscillation of the oscillator can be faster through simultaneously increasing the pulling speed and cooling speed. The snap-through motion of the beam itself provides much faster structural deformations at high force, which could be independently applicable to additional non-periodic tasks [82].

We demonstrated the capability of the printable oscillator by (i) stirring and mixing of fluid, (ii) animating an LED display, (iii) driving an walking robot, and (iv) propelling a gliding swimmer. When supplied with a constant current power, the linear oscillator could give rise to the aforementioned applications and others requiring periodic actuation of origami designs. Due to the high currents (but low voltages) necessary for the thermal actuators, a low series resistance is necessary for its power supply; with an appropriate

battery, these designs can be untethered to enable infrastructureless operation. These can be put into complex environments that would otherwise preclude typical electronic components, including large ambient magnetic or radiation fields.

The printable oscillator is built through origami-inspired manufacturing techniques; the oscillator is preprogrammed and patterned in two-dimensional (2D) sheet material and then folded and assembled into its final three-dimensional (3D) geometry. This approach not only allows integrated and monolithic design and rapid fabrication, but also leads to accessible, low cost, and potentially disposable designs [19], making them an attractive alternative to non-foldable systems that require electronic controls components.

The mechanism of the printable oscillator is verified through the experimental observation of the periodic displacement of the bistable beam. To enable systematic design, we need to built an analytical model for this printable oscillator to allow us to predict its oscillation period against the supply current, geometric parameters, and material properties. This is detailed in Chapter 3.

CHAPTER 3

Modeling and Rapid Design of Printable Oscillators

This chapter has been partially adapted from one conference article (1) and one journal paper (2). The text of the publication was modified to fit within the format of the thesis, and the supplementary information of the publication integrated into the main text.

(1) **Wenzhong Yan**(✉)#, Yunchen Yu #, and Ankur Mehta. "Rapid Design of Mechanical Logic Based on Quasi-Static Electromechanical Modeling". *IEEE/RSJ International Conference on Intelligent Robots and Systems*, pp. 5820-5825, Macau, China, 2019.

(2) **Wenzhong Yan**(✉), Yunchen Yu, and Ankur Mehta. "Analytical Modeling for Rapid Design of Bistable Buckled Beams". *Theoretical and Applied Mechanics Letters*, 9(4), 264-272, 2019.

3.1 Introduction

Printable oscillator, introduced in Chapter 2, is a class of dynamic electromechanical mechanisms which leverages carefully designed mechanical structures to generate programmed control actions from a constant electrical power supply. The basic configuration of this printable oscillator can be abstracted as a bistable mechanism driven by an actuator, which is found in many other processes and applications [83–87]; thus, this work's analysis can be extended to these other systems. For example, it can be easily adapted to model the dynamics of origami logic as described in Chapter 4. The construction of such complex dynamic

systems is usually bottlenecked by the design process, which involves numerous iterations of computationally expensive analysis.

In order to efficiently customize and explore the functionality of this class of integrated mechanism in a rapid prototyping context, a systematic design method needs to be built. Bruch et al. [83] developed a model-based method to design pre-stressed buckled beams with specified snap-through characteristics. Gao et al. [88] also proposed a method for designing and fabricating bistable mechanisms with required snap-through behaviors. These studies utilized data-driven methods that required extensive computation. In this paper, we present an efficient formulation of printable oscillator design from behavioral specification as a low-complexity optimization problem.

Our design method is based on a quasi-static assumption that the printable oscillator's electrothermal subsystem (i.e., the actuators) features a much larger characteristic time constant compared to its mechanical subsystem (i.e., the bistable beam); thus, the behavior of the integrated system is dominated by the dynamics of the actuators. Under this assumption, we develop an analytical expression of the oscillation period of this mechanism on the key snap-through characteristics of bistable buckled beams. Further more, we conduct the analytical modeling of bistable buckled beams, which results in explicit formulas of key snap-through characteristics of bistable buckled beams on the basic design parameters, i.e., material properties, geometry, and boundary conditions. Therefore, we have the analytic expression of the oscillation period of the oscillator on the basic design parameters. With this analytical expression, we eventually transform the design of printable oscillator with a specified oscillation period into a set of constraints on the design parameters. To determine a specific parameter assignment, we can apply these constraints to an optimization criterion. In this work, we choose to maximize the robustness of the resulting design to manufacturing tolerances. As inevitable errors lead to inaccuracy in the realization of the design, we seek to minimize the resulting offset in the specified behavioral parameter after fabrication. This optimization-based method for the rapid design of printable oscillator is demonstrated with

a case study.

3.2 Analytical Modeling of Printable Oscillators

3.2.1 System Description and Governing Equations

The symmetric structure and periodic motion of printable oscillator allow us to only consider its behavior within one single snap-through motion. In this paper, the bistable mechanism is a clamped-clamped elastic buckled beam which is initially straight, and its behavior is described with a PDE [89]. The actuator is characterized with a thermo-electric-mechanical model [17]. In addition, to generate a more generous model, we add another design freedom that the actuation position of the actuator can vary. The targeting system is shown in Fig. 3.1.

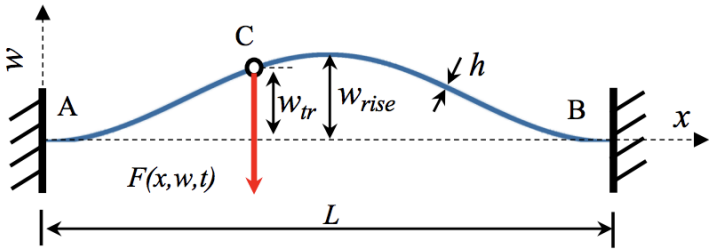

Figure 3.1: A simplified model of the printable oscillator. The actuation force $F(x, w, t)$ from the actuator is applied at a specific point C with an initial displacement w_{tr}. The x-axis represents the line connecting the two ends (i.e., point A and B) of the beam, while the w-axis is set perpendicular to the x-axis at the left end (i.e., point A) of the beam.

3.2.1.1 Bistable Beam

The length, width, and thickness of the beam are denoted as L_0, b, and h, respectively. The span of beam after buckling is denoted as L; the difference between the original length and

the span is denoted as d_0. The ratio $\mu = (x_C - x_A)/(x_B - x_A)$ characterizes the position at which a point force F is applied. Assuming the Euler-Bernoulli beam model, the non-linear PDE that describes the displacement $w(x,t)$ of the beam is as follows [89]:

$$EI\frac{\partial^4 w}{\partial x^4} + P\frac{\partial^2 w}{\partial x^2} - \frac{EA}{2L}\frac{\partial^2 w}{\partial x^2}\int_0^L (\frac{\partial w}{\partial x})^2 dx + m\frac{\partial^2 w}{\partial t^2} + c\frac{\partial w}{\partial t} = F(x,w,t) \tag{3.1}$$

$$w(0,t) = \frac{\partial w}{\partial x}(0,t) = 0, \quad w(L,t) = \frac{\partial w}{\partial x}(L,t) = 0$$
$$w(x,0) = w_0(x) = \frac{w_{\text{rise}}}{2}[1 - cos(\frac{2\pi x}{L})] \tag{3.2}$$

where m, E, c, P, I ($I = bh^3/12$) and A ($A = bh$) refer to the mass per unit length, Young's modulus, viscous damping coefficient, axial loading, second moment, and cross-sectional area of the beam, respectively. $w_0(x)$ refers to the initial displacement of the beam, while w_{rise} refers to the initial rise of the beam's midpoint.

3.2.1.2 CSCP Actuator

The thermo-electric-mechanical model of the actuator is as follows [17]:

$$F_a = k(x_a - x_0) + b_a\dot{x_a} + c_T(T - T_0) \tag{3.3}$$

where F_a, x_a and x_0 are the generated force, the loaded and unloaded length of the actuator, and k, b_a are the mean stiffness and mean damping of the actuator, respectively. T is the temperature of the actuator, T_0 is the room temperature (i.e., 25 °C), and c_T is the mean slope that compensates the temperature rise. In order to simplify our model, we ignore the term $b_a\dot{x}$, as the effect of damping is considered negligible. The temperature rise of the actuator is described with Eq. 3.4, as derived from Yip's work [17]:

$$T(t) = \frac{R}{\lambda I^2}(1 - e^{-\frac{\lambda}{C_{\text{th}}}t}) + T_0 \tag{3.4}$$

where λ is the absolute thermal conductivity of the actuator in the ambient environment, while C_{th} and R refer to its thermal mass and resistance, respectively. The voltage U

across the actuator is assumed constant in this work. The relationships between some of the aforementioned parameters of the actuator and its length x_0 are as follows:

$$k = \frac{\gamma_1}{x_0},\ C_{\text{th}} = \gamma_2 x_0,\ \lambda = \gamma_3 x_0,\ R = \gamma_4 x_0 \tag{3.5}$$

where γ_1, γ_2, γ_3, and γ_4 are associated with the environment, experimental setup, and properties of the actuator material.

3.2.2 Quasi-Static Approximation Framework

Here the dynamic model of printable oscillator is simplified under a quasi-static assumption. Ultimately an analytical formula of printable oscillator's oscillation period is derived.

3.2.2.1 Quasi-Static Assumption

To simplify our model, we make a quasi-static assumption that the electrothermal subsystem of printable oscillator features a significantly larger characteristic time constant than the mechanical subsystem. Thus, in response to the force generated by the actuator, the bistable beam is able to achieve equilibrium instantly. Therefor, the dynamics of the actuator dictates the behavior of the entire system. This quasi-static assumption is verified with FEA simulations. Moreover, we assume that the bistable beam settles instantly after snap-through motion, since it will immediately rest on a flexible contact pad with high damping [90].

3.2.2.2 Quasi-Static Assumption Verification

To validate our assumption, the time constants of both subsystems are evaluated and compared. The time constant of the mechanical subsystem (underdamped) is estimated as $\tau_{\text{m}} = \pi/(w_{\text{n}}\sqrt{1-\zeta^2})$ [91], where w_{n} and ζ refer to the natural frequency and damping ratio of the system. In this work, we adopt the first-order natural frequency to calculate the time

constant τ_{m}. The time constant of the electrothermal subsystem, on the other hand, is given as $\tau_{\mathrm{et}} = C_{\mathrm{th}}/\lambda$ [17]. To obtain the natural frequency w_{n} of the mechanical subsystem and explore the relationships between w_{n} and design parameters, several FEA models are built, with their design parameters listed in Table 3.1. Specifically, Case 1 is used as the example to demonstrate the verification process.

3.2.2.3 FEA Model

The FEA model of the simplified mechanical subsystem is built with ABAQUS 2017, as shown in Fig.3.2(A). Both ends of the beam are fixed after precompression ($d_0 = 0.6$ mm). One end of the actuator is connected to the beam at the location $\mu = 0.43$ and the other end is fixed at a position that makes the actuator initially stress-free. The equivalent Young's modulus of the actuator is given by the equation $E = kL/A$. In the FEA model, the element Beam B21H is adopted for both the beam and the actuator.

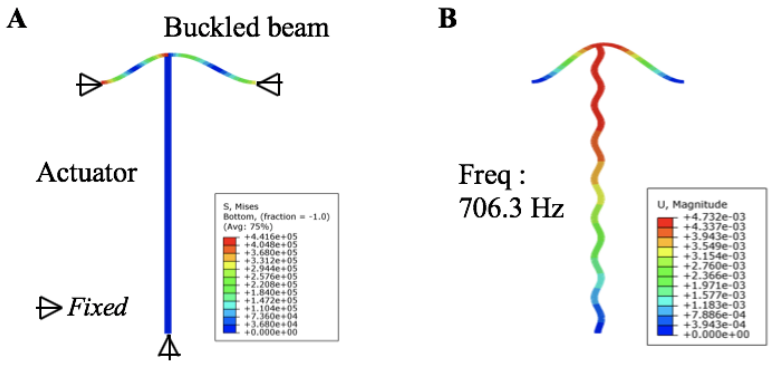

Figure 3.2: FEA simulation (Case 1 in Table 3.1). (A) FEA model. The beam is double-clamped and buckled under axial precompression. One end of the actuator is fixed and the other one is connected with the beam. (B) The first mode shape of the bistable beam with the corresponding natural frequency 706.30 Hz. The dimensions of the figure are adjusted for better presentation.

3.2.2.4 Time Constant Comparison

The natural frequency corresponding to the first mode shape of the bistable beam in Case 1 is 706.3 Hz (Fig. 3.2(B)). Thus, with ζ approximated as 0.5, τ_{m} is calculated as 5.7×10^{-3} s. Meanwhile, with C_{ch} and λ measured as 0.453 $Ws/^{\circ}C$ and 0.249 $W/^{\circ}C$, respectively, τ_{et} can be calculated as 1.8 s. Since C_{ch} and λ both are proportional to the length of the actuator, τ_{et} is constant. The natural frequency of the mechanical subsystem is highly insensitive to relevant design parameters. As shown in Case 2-4 where we assign extreme values to different parameters, the resulting natural frequency is not significantly influenced by these changes (corresponding FEA simulation results are not shown since these cases have rather similar mode shapes to Case 1). Thus, within our range of consideration, the time constant of the electrothermal subsystem is always significantly larger than that of the mechanical subsystem.

3.2.2.5 A Reduced Model of Printable Oscillator

Under the quasi-static assumption, instead of solving Eq. 3.1 for $w(x,t)$, we perform time-stepping and solve for the beam's displacement at any time point in the actuation process, assuming that the beam reaches a static equilibrium. Thus, we can eliminate the time derivative terms in Eq. 3.1 and combine it with Eq. 3.3 with the damping term ignored. The resulting ODE describes the bistable beam's displacement at a specific time point t_{i}, as shown in Eq. 3.6 and Eq. 3.7.

$$EI\frac{d^4w_{\mathrm{i}}}{dx^4}+P\frac{d^2w_{\mathrm{i}}}{dx^2}-\frac{EA}{2L}\frac{d^2w_{\mathrm{i}}}{dx^2}\int_0^L(\frac{dw_{\mathrm{i}}}{dx})^2dx = F\delta(x-\mu L) \tag{3.6}$$

$$F=-c_{\mathrm{T}}[T(t_i)-T_0]-k[w_{\mathrm{i}}(\mu L)-w_0(\mu L)] \tag{3.7}$$

In Eq. 3.6, $w_{\mathrm{i}}(x)$ denotes the displacement of the bistable beam at time t_{i} and satisfies the boundary conditions in Eq. 3.2. We transform the point force applied on the beam at

Table 3.1: A typical set of parameters of a printable oscillator.

Parameters	Unit	Case1	Case2	Case3	Case4
Bistable beam :					
Length (L_0)	mm	14.9	14.9	14.9	14.9
Width (b)	mm	3.0	1.0	3.0	3.0
Thickness (h)	mm	0.132	0.132	0.05	0.132
Precompression (d_0)	mm	0.6	0.6	0.6	0.05
Young's modulus (E)	GPa	3.0	3.0	3.0	3.0
Density (ρ)	g/cm^3	1.38	1.38	1.38	1.38
Poisson's ratio (ν)	1	0.50	0.50	0.50	0.50
CSCP actuator :					
Length (x_0)	mm	50.0	50.0	50.0	50.0
Diameter (D)	mm	0.8	0.8	0.8	0.8
Young's modulus (E)	MPa	18.6	18.6	18.6	18.6
Density (ρ)	g/cm^3	1.15	1.15	1.15	1.15
Poisson's ratio (ν)	1	0.50	0.50	0.50	0.50
Natural Freq.(ω)	Hz	706.3	706.3	574.6	706.3

the position $x = \mu L$ into a distributive load with an equivalent actuation effect, utilizing the Dirac delta function. In Eq. 3.7, F is regarded as negative because it assumes the negative direction, as shown in Fig. 3.1. The magnitude of this point force at time t_i is also given by Eq. 3.7. This boundary value problem can be solved using the Galerkin method [92].

3.2.2.6 Analytical Expression of the Oscillation Period

As we assign different values to F in Eq. 3.6 and study the beam's corresponding equilibrium displacement at $x = \mu L$, we obtain a force-displacement curve of the bistable beam, as represented by the blue curve in Fig. 3.3. Also, Eq. 3.7 indicates a linear relationship between F and the difference between the loaded and unloaded length of the actuator at a given time point. Since the actuator is attached to the beam, this length difference is reflected by the beam's displacement at $x = \mu L$. Therefore, at any time point, there is a linear relationship between F and $w(\mu L)$, as demonstrated by the straight lines in Fig. 3.3. Thus the equilibrium displacement of the bistable mechanism at $x = \mu L$ at time t_{i} is

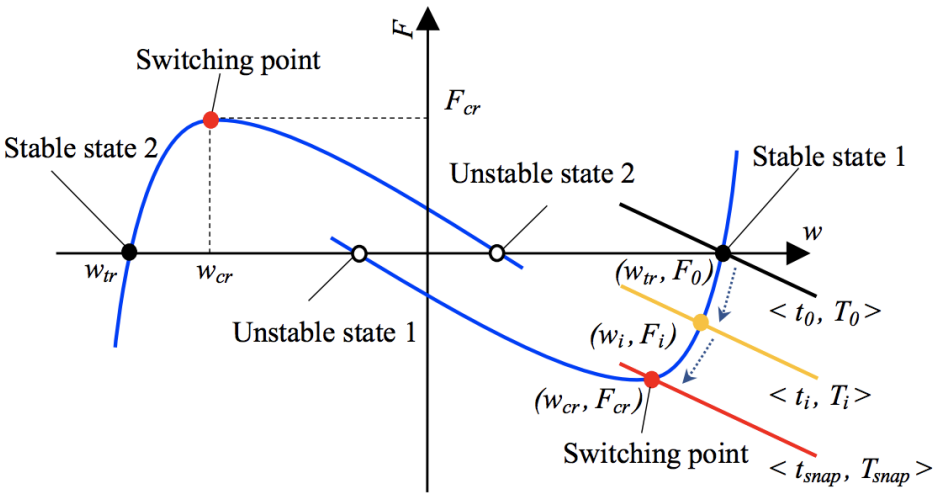

Figure 3.3: The mechanism of the decoupled model of printable oscillators. Blue profiles are the force-displacement curves of the bistable buckled beam under off-center actuation; Straight lines are the force-displacement curves of the CSCP actuator at different temperature.

characterized by the intersection of the invariant force-displacement curve of the bistable beam and the linear curve $F - w_{\mathrm{i}}(\mu L)$ that characterizes the force generated by the actuator at time t_{i}. At the beginning ($t = t_0$), the linear curve is represented by the black line in Fig. 3.3 and intersects with the force-displacement curve at $(w_{\mathrm{tr}}, 0)$, where w_{tr} refers to the initial

displacement of the actuation position ($w_0(\mu L) = w_{\mathrm{tr}}$). As time elapses, the temperature of the actuator increases and the $F - w_{\mathrm{i}}(\mu L)$ curve moves downward, with the intersection of the two curves moving toward the switching point $(w_{\mathrm{cr}}, F_{\mathrm{cr}})$.

This representation of the equilibrium displacement of the bistable mechanism thus allows us to directly calculate the time needed for the bistable beam to reach the snap-through point, which, in this work, is assumed to be the switching point $(w_{\mathrm{cr}}, F_{\mathrm{cr}})$. In other words, we assume that the linear curve given by Eq. 3.7 at the snap-through time t_{snap} passes through the switching point. Thus, t_{snap} satisfies the equation:

$$F_{\mathrm{cr}} = -c_{\mathrm{T}}[T(t_{\mathrm{snap}}) - T_0] - k[w_{\mathrm{cr}} - w_{\mathrm{tr}}] \tag{3.8}$$

Combining Eq. 3.4 and Eq. 3.8, with the fact that the printable oscillator's oscillation period T_{a} is twice t_{snap}, we have:

$$T_{\mathrm{a}} = -2\frac{C_{\mathrm{th}}}{\lambda} ln[1 - \frac{\lambda}{c_{\mathrm{T}} R I^2}(k w_{\mathrm{tr}} - k w_{\mathrm{cr}} - F_{\mathrm{cr}})] \tag{3.9}$$

$$I > \sqrt{\frac{\lambda}{c_{\mathrm{T}} R}[F_{\mathrm{cr}} - k(w_{\mathrm{cr}} - w_{\mathrm{tr}})]}. \tag{3.10}$$

I is the supplied electrical current through the actuator with a lower bound for oscillation defined by Eq. 3.10.

The beam's snap-through characteristics, w_{tr}, w_{cr}, and F_{cr}, are extracted from its force-displacement curve. Studying Eq. 3.6 by changing the magnitude of F and calculating the corresponding displacement of the beam is one possible way to obtain the force-displacement curve, and curves generated with other methods (e.g. experiments) also apply, as long as the parameters w_{tr}, w_{cr}, and F_{cr} can be evaluated from these curves.

3.2.3 Validation and Discussions

In our experiment, we used a 69.0 mm actuator with R = 3.8 Ω, k = -0.28 N/mm, and c_T = 1.6 × 10^{-2} N/°C (see Text S6). The bistable beam features snap-through characteristics

measured to be w_{rise} = -2.12 mm, $w_{\text{snap-thru}}$ = -0.89 mm, and $F_{\text{snap-thru}}$ = 0.42 N (see Text S7). The influence of supply current (for convenience since the resistance is constant) on oscillation period is shown in Fig. 3.4A. When the current increased, T_{osc} dropped monotonically; the corresponding oscillation curves of the center point of the bistable beam are presented in Fig. 3.4B. During the experiment, the motor was unable to oscillate outside the range of [0.54 A, 0.63 A] of the supply current. When the current is smaller than 0.54 A, the actuator could not generate enough force to activate the snap-through motion due to the insufficient equilibrium temperature. Meanwhile, oscillation is not sustainable when the T_{osc} is smaller than T_{cool} due to the switch reset requirements. By fitting the experimental results of the oscillation period versus current, we obtained the the thermal mass, C_{th}, and absolute thermal conductivity, λ, of the actuator to be 2.99×10^{-2} Ws/°C and 2.31×10^{-2} W/°C, respectively. The fitting curve (the red dash line in Fig. 3.4A) indicates the lower bound of the current is around 0.538 A (from Eq.3.10), which is very close to our experimental observation, i.e., 0.54 A. In addition, the fitting curve suggests that the period asymptotically approaches 0 with increasing supply power, however, real limits on the period include cooling time, snap-through duration, and inertial dynamics outside our assumed bounds.

Though dramatically simplified, our model that showed a good agreement with the experimental observation, suggests that it may be used as an analytical tool to predict the system behaviors of the foldable oscillator or other similar devices that composed of bistable mechanisms and linear actuators. In addition, this analytical model can be potentially used to create a design tool for rapid prototyping of the oscillator due to its simplicity and explicitness [93]. However, in order to achieve rapid design of oscillator from behavioral specification, frequency, the analytical formulas of the buckled beam's snap-through characteristics, w_{tr}, w_{cr}, and F_{cr} expressed by the basic design parameters, i.e., material properties, geometry, and boundary conditions are needed.

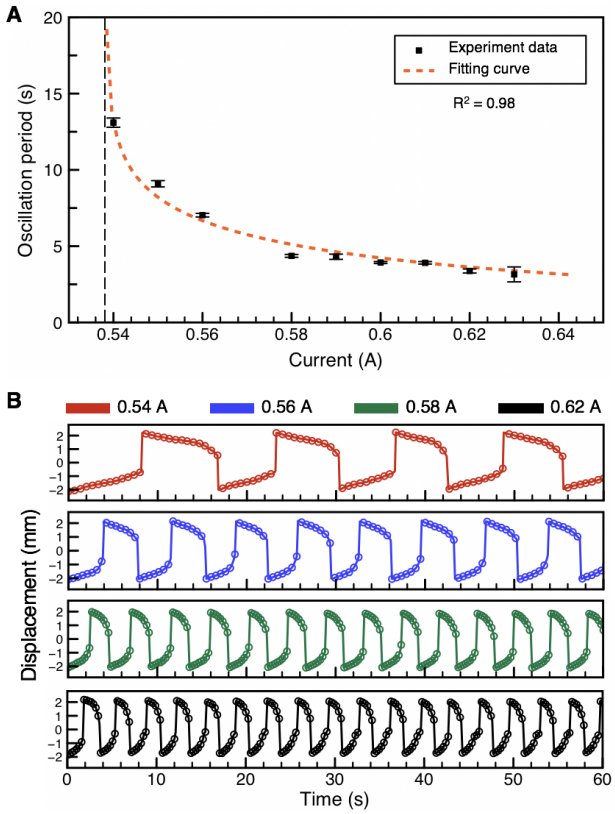

Figure 3.4: Oscillation period varies with the supply current. (A) Oscillation period, T_{osc}, as a function of the current amplitude. The fit curve (red dashed curve, $R^2 = 0.98$) matches well with the experimental data, predicting the lower bound of the applicable current supply as around 0.538 A. Below this lower bound, the motor is no long capable of oscillating. The curve also indicates that the oscillation period can be arbitrarily low with sufficient current (provided equally short cooling time). Error bars represent standard deviations. (B) Time-resolved oscillation displacement curves with various supply currents: $I_{\text{supp}} = 0.54$ A (red); $I_{\text{supp}} = 0.56$ A (blue), $I_{\text{supp}} = 0.58$ A (green), and $I_{\text{supp}} = 0.62$ A (black).

3.3 Analytical Modeling of Bistable Buckled Beams

3.3.1 Description of the System

Here we consider a clamped-clamped and initially straight elastic beam, as shown in Fig. 3.5. The original length, width, thickness, and Young's modulus of the beam are denoted as L_0, b, h, and E, respectively. Under a compressive axial load P, one of the beam's terminals moves towards the other, resulting in a first-mode buckling shape with initial rise w_{rise} (i.e., the initial displacement of the beam's mid-span). The distance between the two terminals of the beam after buckling, what we refer to as the span, is denoted as L; the difference between the original length and the span is denoted as d_0 (i.e., $d_0 = L_0 - L$). Moreover, the cross-sectional area of the beam and the second moment are denoted as A ($A = bh$) and I ($I = \frac{1}{12}bh^3$), respectively.

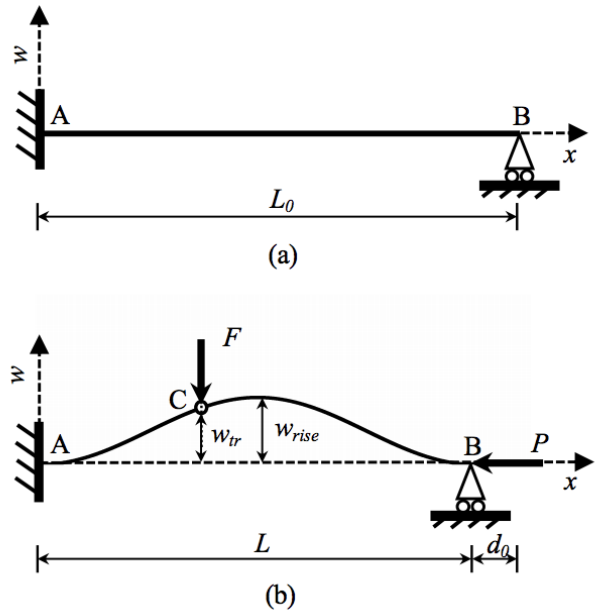

Figure 3.5: A clamped-clamped bistable buckled beam. (A) The non-loaded straight beam; (B) The beam in its buckled configuration with an actuating force F applied at the location C.

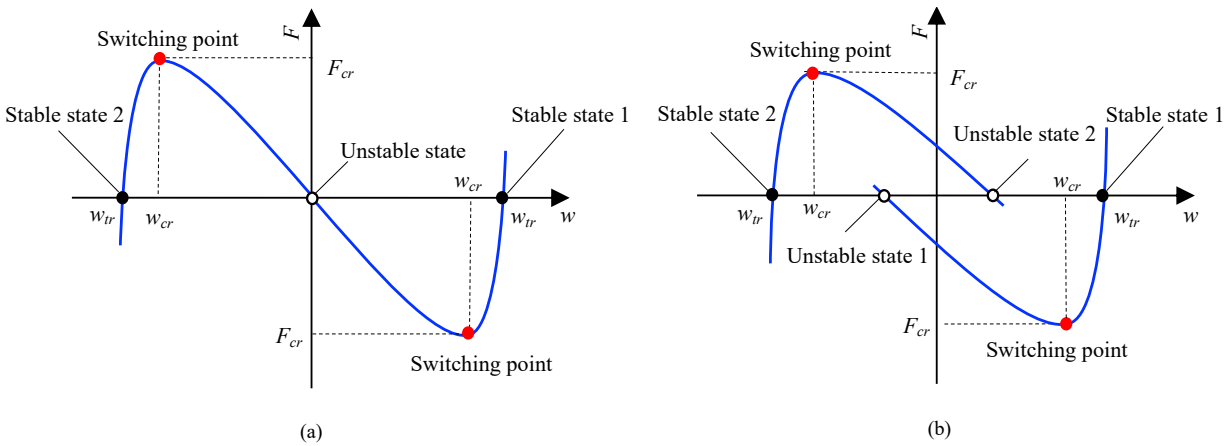

Figure 3.6: Characteristic force-displacement ($F - w$) curve of bistable buckled beams. (A) Under center actuation; (B) Under off-center actuation.

The system's two-dimensional reference frame is chosen such that the x-axis coincides with the line connecting the two ends of the beam after it is axially compressed, while the w-axis is set perpendicular to the x-axis at one end of the beam, as shown in Fig. 3.5. A point force F in the w-direction is applied vertically to the buckled beam at a selected location C. The ratio $\delta = \frac{x_C - x_A}{x_B - x_A}$ is the parameter that indicates the position at which F is applied to the beam.

3.3.2 Theoretical Model

In this section, a theoretical model of bistable buckled beams is derived and subsequently simplified. This model allows for characterizing the snap-through properties of a bistable buckled beam and enables the derivation of analytical expressions of the beam's important snap-through characteristics.

According to Euler's buckling model of a double-clamped slender beam, when the axially compressed beam is undisturbed (i.e., $F = 0$), its behavior can be described with the

following differential equation:

$$\begin{aligned} & w^{iv}(x) + n^2 w''(x) = 0 \\ & n^2 = \frac{P}{EI} \\ & w(0) = w(L) = w'(0) = w'(L) = 0 \end{aligned} \tag{3.11}$$

The eigenvalues of this homogeneous Strum-Liouville problem can be denoted in form of $n_{\mathrm{i}}L$, and these eigenvalues satisfy the equation:

$$1 - cos(n_{\mathrm{i}}L) = \frac{1}{2} n_{\mathrm{i}} L sin(n_{\mathrm{i}}L) \tag{3.12}$$

The eigenvalues give rise to a series of nontrivial eigenfunctions of Eq. 3.12:

$$\begin{aligned} w_{\mathrm{i}}(x) = \begin{cases} C_{\mathrm{i}}[1 - cos(n_{\mathrm{i}}x)] & i = 0, 2, 4... \\ C_{\mathrm{i}}\{1 - cos(n_{\mathrm{i}}x) - \frac{2}{n_{\mathrm{i}}L}[n_{\mathrm{i}}x - sin(n_{\mathrm{i}}x)]\} & i = 1, 3, 5... \end{cases} \\ n_{\mathrm{i}}L = 2\pi, 4\pi, 6\pi... \qquad i = 0, 2, 4... \\ n_{\mathrm{i}}L = 2.86\pi, 4.92\pi, 6.94\pi... \qquad i = 1, 3, 5... \end{aligned} \tag{3.13}$$

When a force F is applied to the beam, its displacement $w(x)$ can be described as a superposition of these eigenfunctions:

$$w(x) = \sum_{i=0}^{\infty} A_{\mathrm{i}} w_{\mathrm{i}}(x) \tag{3.14}$$

where the set of amplitudes A_{i}'s minimizes the energy of the system under the constraint of the beam's current length, $L + d_0 - d_{\mathrm{p}}$ [94]. d_{p} refers to the contraction from the axial load P and is given as $d_{\mathrm{p}} = \frac{PL}{EA}$. Thus, we have the following equation:

$$L + d_0 - d_{\mathrm{p}} = \int_0^L \sqrt{1 + [w'(x)]^2} dx \approx \int_0^L \{1 + \frac{[w'(x)]^2}{2}\} dx \tag{3.15}$$

Combining Eq. 3.14 and 3.15, we have:

$$g(\bar{A}) = \sum_{i=0}^{\infty} \frac{A_i^2 (n_{\mathrm{i}}L)^2}{4} - (d_0 - d_{\mathrm{p}})L = 0 \tag{3.16}$$

The energy of the system can be written as:

$$\begin{aligned} U(\bar{A}, F) &= \frac{EI}{2}\int_0^L [w''(x)]^2 dx + Fw(\delta L) + \frac{Pd_{\mathrm{p}}}{2} \\ &= \frac{EI}{4L^3}\sum_{i=0}^{\infty} A_i^2 (n_{\mathrm{i}}L)^4 + F\sum_{i=0}^{\infty} A_{\mathrm{i}} w_{\mathrm{i}}(\delta L) + \frac{Pd_{\mathrm{p}}}{2} \end{aligned} \tag{3.17}$$

where the three terms refer to the bending energy of the beam, the potential energy of the force, and the compression energy, respectively [94]. In Vangbo's work, the parameter δ in the second energy term is always set to 0.5 as the force is applied at the beam's center; in this work, however, we allow δ to vary in order to account for off-center actuation.

Therefore, we solve for the A_{i}'s that minimize U in Eq. 3.17 and conform to the constraint specified by Eq. 3.16. We introduce a Lagrange multiplier λ in order to find the equilibrium state of the beam under a force F. We consider:

$$K(\bar{A}) = U(\bar{A}, F) - \lambda g(\bar{A}) \tag{3.18}$$

The solutions A_{i}'s should satisfy:

$$\frac{\partial K}{\partial A_{\mathrm{i}}} = 0 \quad (and \quad \frac{\partial K}{\partial \lambda} = 0) \tag{3.19}$$

Solving Eq. 3.19, with λ chosen in the same way as in Vangbo's work, we have:

$$A_{\mathrm{i}} = \frac{2FL^3 w_{\mathrm{i}}(\delta L)}{EI(n_{\mathrm{i}}L)^2[(\eta L)^2 - (n_{\mathrm{i}}L)^2]}, \quad with \quad \eta^2 = \frac{P}{EI} \tag{3.20}$$

Combining Eq. 3.20 and the constraint given by Eq. 3.16, we can determine the magnitude of F when given a value of the parameter η.

$$F(\eta) = \frac{EI\sqrt{(d_0 - d_{\mathrm{p}})L}}{L^3\sqrt{\sum_{i=0}^{\infty} \frac{w_i^2(\delta L)}{(n_{\mathrm{i}}L)^2[(\eta L)^2 - (n_{\mathrm{i}}L)^2]^2}}}, \quad with \quad d_{\mathrm{p}} = \frac{PL}{EA} = \frac{\eta^2 LI}{A} \tag{3.21}$$

Also, combining Eq. 3.14 and 3.20, we have:

$$w(\eta) = \frac{2F(\eta)L^3}{EI}\sum_{i=0}^{\infty} \frac{w_i^2(\delta L)}{(n_{\mathrm{i}}L)^2[(\eta L)^2 - (n_{\mathrm{i}}L)^2]} \tag{3.22}$$

Eq. 3.20, 3.21, and 3.22 characterize the connections among the actuating force F, the beam's displacement w, and the axial load P ($P = \eta^2 EI$) applied to the beam from side walls. Importantly, the obtained force-displacement curve can be used to characterize the mechanical properties of the bistable buckled beam.

3.3.3 Reduced Model

As largely mentioned in related works [95, 96], the first two modes of buckling, $w_0(x)$ and $w_1(x)$, have predominant contribution in the beam's displacement $w(x)$ in both center and off-center actuation scenarios [96]. Thus, we can make the approximation that $w(x) = A_0 w_0(x) + A_1 w_1(x)$ and write:

$$F(\eta) = \frac{EI\sqrt{(d_0 - d_\mathrm{p})L}}{L^3\sqrt{\frac{w_0^2(\delta L)}{(n_0 L)^2[(\eta L)^2-(n_0 L)^2]^2} + \frac{w_1^2(\delta L)}{(n_1 L)^2[(\eta L)^2-(n_1 L)^2]^2}}} \tag{3.23}$$

$$w(\eta) = \frac{2F(\eta)L^3}{EI}\left[\frac{w_0^2(\delta L)}{(n_0 L)^2[(\eta L)^2 - (n_0 L)^2]} + \frac{w_1^2(\delta L)}{(n_1 L)^2[(\eta L)^2 - (n_1 L)^2]}\right] \tag{3.24}$$

Moreover, recall that $P(\eta) = \eta^2 EI$ and that we have:

$$\begin{aligned} P_0 &= n_0^2 EI, \quad with \quad n_0 L = 2\pi \\ P_1 &= n_1^2 EI, \quad with \quad n_1 L = 2.86\pi \end{aligned} \tag{3.25}$$

where P_0 and P_1 represent the axial compressive load of the first-mode and second-mode buckling, respectively. Note that the switching of the beam always features an axial load greater than P_0 but not exceeding P_1 [94].

3.3.4 Analytical Expressions of the Snap-through Characteristics

Generally, the three critical behavioral values, F_cr, w_cr, and w_tr on the force-displacement curve are sufficient for characterizing a bistable buckled beam and facilitating its design.

Given the significance of these behavioral values, it is worthwhile to develop explicit analytical expressions for each of them.

3.3.4.1 Critical Force

The magnitude of F_{cr} can be considered the maximum of the function $F(\eta)$ in Eq. 3.23 when $2\pi < \eta L < 2.86\pi$:

$$F_{\text{cr}} = max[\, F(\eta)\,], \quad with \;\; 2\pi < \eta L < 2.86\pi \tag{3.26}$$

To simplify Eq. 3.26, we take advantage of the fact that the thickness of the beam h is much smaller than $\sqrt{d_0 L}$ [94, 96, 97]. Therefore, we have:

$$d_{\text{p}} L = \frac{I}{A}(\eta L)^2 = \frac{1}{12}h^2(\eta L)^2 << d_0 L \tag{3.27}$$

Hence, we can assume a simplified version of Eq. 3.26:

$$\begin{aligned} F_{\text{cr}} &= \frac{EI\sqrt{d_0 L}}{L^3} max[\, P(\eta)], \quad with \;\; 2\pi < \eta L < 2.86\pi \\ P(\eta) &= \frac{1}{\sqrt{\frac{w_0^2(\delta L)}{(2\pi)^2[(\eta L)^2-(2\pi)^2]^2} + \frac{w_1^2(\delta L)}{(2.86\pi)^2[(\eta L)^2-(2.86\pi)^2]^2}}} \end{aligned} \tag{3.28}$$

Notice that we have:

$$\begin{aligned} w_0(\delta L) &= 1 - cos(2\pi\delta) \\ w_1(\delta L) &= 1 - cos(2.86\pi\delta) - \frac{2}{2.86\pi}[2.86\pi\delta - sin(2.86\pi\delta)] \end{aligned} \tag{3.29}$$

It can be observed from Eq. 3.28 and 3.29 that $argmax\, P(\eta)$ (denoted as $\hat{\eta}$) and thus $max\, P(\eta)$ are only dependent on the parameter δ. In other words, we can denote $max\, P(\eta)$ on $[2\pi,\, 2.86\pi]$ as a function of δ, written as $F_0(\delta)$. So we have:

$$F_{\text{cr}} = \frac{EI\sqrt{d_0 L}}{L^3} F_0(\delta) \tag{3.30}$$

To obtain an analytical form of F_0, we vary δ from 0.15 to 0.5, the scope of this parameter within our consideration (note that by symmetry, we only need to consider one half of the

beam), and calculate the corresponding values of F_0. We then apply curve-fitting to obtain an analytical relationship between $F_0(\delta)$ and δ. $F_0(\delta)$ as a function of δ is visualized in Fig. 3.7 and presented in Eq. 3.31 with the error of fitting less than 7%. F_0 is chosen as a degree-4 polynomial to ensure relatively high accuracy and acceptable complexity of the model. Note that this curve-fitting can be reperformed to improve the accuracy of the final result or to reduce the complexity of the model.

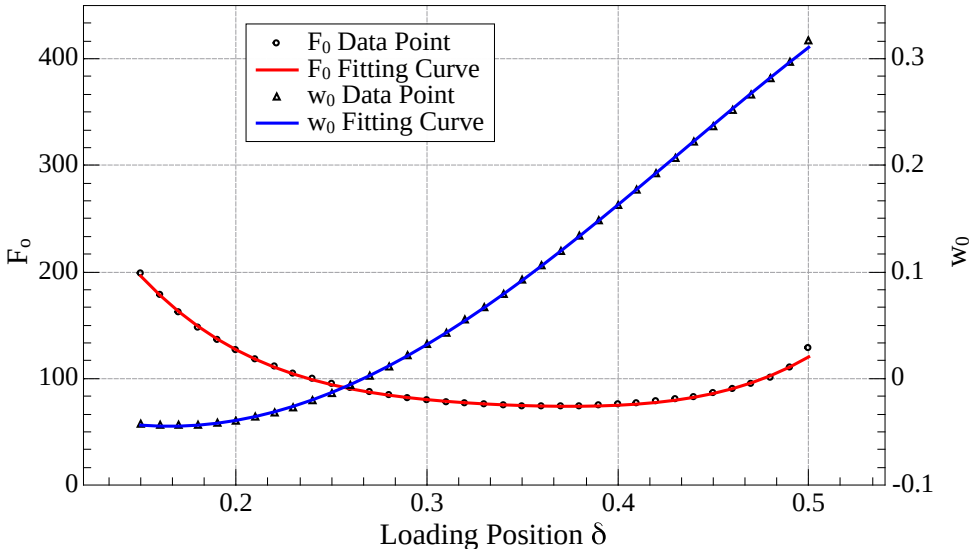

Figure 3.7: Curve fitting of F_0 and w_0.

The analytical expression of the critical force F_{cr} at a precompressed beam's switching point can be written as Eq. 3.31. Note that the minimal critical force is achieved where δ is equal to 0.37 (or 0.63).

$$\begin{aligned} F_{\text{cr}} &= \frac{EI\sqrt{d_0 L}}{L^3} F_0(\sigma) \\ \sigma &= min(\delta, 1-\delta) \\ F_0(\sigma) &= 50588\sigma^4 - 69285\sigma^3 + 36606\sigma^2 - 8894.5\sigma + 914.9 \end{aligned} \tag{3.31}$$

3.3.4.2 Critical Displacement

The critical displacement w_{cr} can also be written in form of an analytical expression of the basic parameters. From Eq. 3.24 and 3.31, we have:

$$w_{\text{cr}} = 2\sqrt{d_0 L}F_0(\delta)\{\frac{w_0^2(\delta L)}{(n_0 L)^2[(\bar{\eta}L)^2 - (n_0 L)^2]} + \frac{w_1^2(\delta L)}{(n_1 L)^2[(\bar{\eta}L)^2 - (n_1 L)^2]}\} \tag{3.32}$$

Since we have shown that $\bar{\eta}$ only depends on δ, we can conclude that $w_{\text{cr}} = 2\sqrt{d_0 L}w_0(\delta)$ by substituting the bulk of Eq. 3.32 with w_0, some function of δ. To obtain an analytical form of w_0, we vary the parameter δ from 0.15 to 0.5 and calculate the corresponding values of $w_0(\delta)$. w_0 as a function of δ is displayed in Fig. 3.7 and its analytical form is shown in Eq. 3.33 after some change of variables. The analytical expression of w_{cr} is written as follows:

$$\begin{aligned} &w_{\text{cr}} = 2\sqrt{d_0 L}w_0(\sigma) \\ &\sigma = min(\delta, 1-\delta) \\ &w_0(\sigma) = -7.155\sigma^4 + 2.872\sigma^3 + 4.339\sigma^2 - 1.538\sigma + 0.0832 \end{aligned} \tag{3.33}$$

Again, the curve-fitting can be reperformed for alternative analytical expressions of w_0. Moreover, it is important to note that the critical displacement is primarily dependent on L, d_0, and δ, a result consistent with that of Bruch et al. [98] but obtained with a different method.

3.3.4.3 Travel

The initial shape of an axially compressed beam can be approximated using the cosine curve featured in the expression of $w_0(x)$. Thus, we have $w_{\text{tr}} = \frac{w_{\text{rise}}}{2}[1 - cos(2\pi\delta)]$ by definition of the travel, where w_{rise} is the initial rise of the beam's midpoint, determined by the degree of compression. Considering Eq. 3.15, since we have shown that $d_{\text{p}} << d_0$, we can ignore the

term d_{p} and approximate w_{rise} from the following relationship:

$$\begin{aligned} L + d_0 &\approx \int_0^L \{1 + \frac{[{w_{\mathrm{init}}}'(x)]^2}{2}\} dx, \\ with \quad w_{\mathrm{init}}(x) &= \frac{w_{\mathrm{rise}}}{2}[1 - cos(\frac{2\pi x}{L})] \end{aligned} \tag{3.34}$$

It can be calculated from Eq. 3.34 that $w_{\mathrm{rise}} = \frac{2\sqrt{d_0 L}}{\pi}$, and so we have:

$$w_{\mathrm{tr}} = \frac{\sqrt{d_0 L}}{\pi}[1 - cos(2\pi\delta)] \tag{3.35}$$

One significant observation from Eq. 3.33 and 3.35 is that the value of $\frac{w_{\mathrm{cr}}}{w_{\mathrm{tr}}}$ only depends on the parameter δ. The key insight is that when designing a precompressed bistable mechanism, the possible constraints on these two behavioral parameters may uniquely determine its optimal actuation position.

3.3.5 Validation and Discussions

In this section, we consider a double-clamped bistable buckled beam with its parameters given in Table 3.2. All of the parameters above remain unchanged throughout this section unless otherwise stated.

Table 3.2: Geometric and material parameters of the beam.

Parameter	Unit	Value
Length (L_0)	mm	14.9
Width (b)	mm	3.0
Thickness (h)	mm	0.132
Precompression (d_0)	mm	0.3
Young's modulus (E)	GPa	3.0

3.3.5.1 Model Validation

To validate our model, we compare our results, the $F-w$ and $P-w$ curves for both center and off-center actuation of a bistable buckled beam, with quasi-static force-displacement curves from ABAQUS. The bistable beam was modeled in three dimensions and its geometry was meshed with quadrilateral shell elements (i.e., S4R) that can capture large deformation behaviors. The buckling of the beam was introduced by an initial imperfection in the lateral direction. In our analytical model, Eq. 3.23 and 3.24 combined give rise to the $F-w$ characteristic, while the relationship $P=\eta^2 EI$ and Eq. 3.24 combined yield the $P-w$ curve.

Center Actuation. With δ set to 0.5, the $F-w$ and $P-w$ curves of the beam are graphed and compared to data from an FEA model, as shown in Fig. 3.8. In this figure, the solid black line represents the result from the our model while the circles depict the FEA simulation data. Two series of simulation data are presented: (i) the red circles represent the snap-through motion from the top stable equilibrium state to the bottom one, as depicted in Fig. 3.5(B); (ii) the blue circles correspond to the motion in the opposite direction.

In both diagrams, point $a1$ and $a2$ represent the beam's two stable equilibrium states that feature first-mode buckling ($P=P_0, \eta L=2\pi$). Point $c1$ (or $c2$) corresponds to its unstable equilibrium state that features second-mode buckling ($P=P_1, \eta L=2.86\pi$). Point $b1$ and $b2$ are the switching points.

There is a neat agreement between the actuating force F and the compressive force P calculated from our model and from the FEA model, with errors bounded within 7% and 6%, respectively. Note that the greatest discrepancy occurs around the switching points, where the critical force is modeled fairly accurately, while the critical displacement from our model is larger than that calculated from the FEA model. This means our model suggests a premature snap-through of the bistable beam.

Off-Center Actuation. Under an off-center actuation (δ=0.37), the $F-w$ and $P-w$

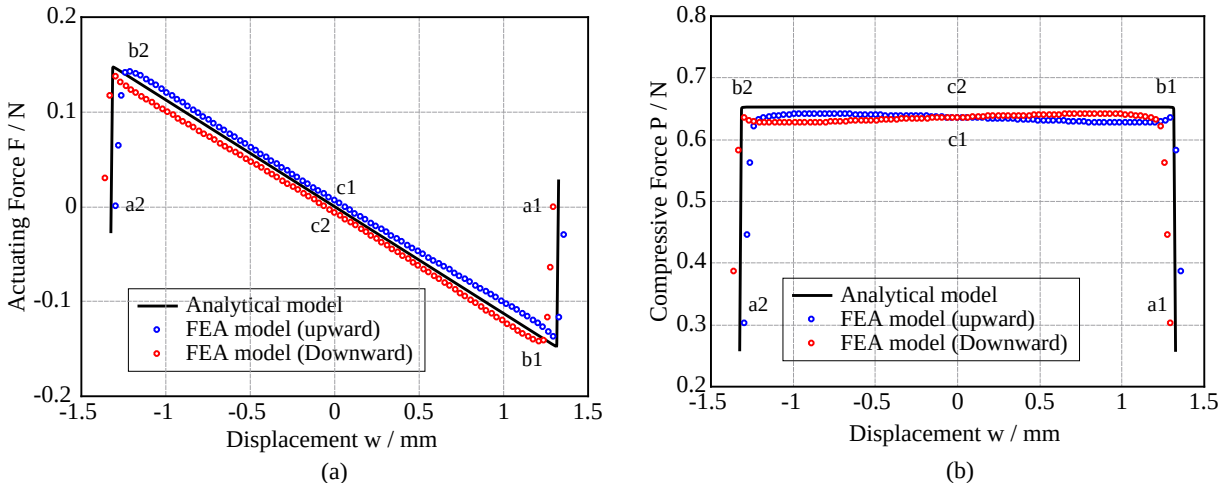

Figure 3.8: Center actuation: FEA results and comparison to our model. (A) actuating force F vs displacement w; (B) compressive force P vs displacement w.

curves of the beam are shown in Fig. 3.9. In the same manner, the solid black curves represent our analytical model while the red (downward) and blue (upward) circles come from the FEA simulation results.

Contrary to the center actuation, the off-center actuation from the two directions results in two distinct branches in the $F-w$ curve, as shown in both diagrams. This indicates that the switching of the beam involves a branch jump [96]. Similarly, $a1$ and $a2$ are the two stable equilibrium points ($P = P_0$, $\eta L = 2\pi$). $c1$ and $c2$ both represent the unstable equilibrium state of the beam ($P = P_1$, $\eta L = 2.86\pi$), approached when the beam is actuated by an off-center force from its two different stable positions. Points $b1$ and $b2$ are the switching points of the bistable beam.

The results from our analytical method are consistent with the FEA simulation data. Errors on the $F-w$ and $P-w$ curves with respect to the FEA results are bounded within 2% and 5%, respectively. The small magnitudes of these errors greatly demonstrate the validity of our model.

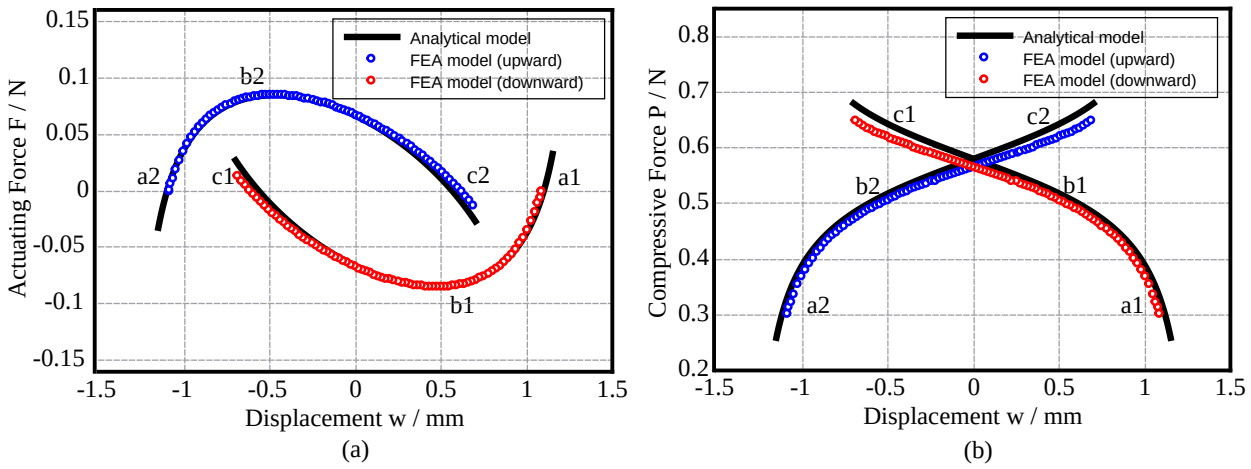

Figure 3.9: Off-center actuation: FEA results and comparison to our model. (A) actuating force F vs displacement w; (B) compressive force P vs displacement w.

3.3.5.2 Influence of Design Parameters on Snap-through Characteristics

To facilitate the rapid design of bistable buckled bistable beams, we discuss the influence of a bistable beam's key design parameters on its snap-through characteristics, namely its critical force, critical displacement, and travel. These results are also verified by an FEA model.

Actuation Position. The impact of δ on the critical force is visualized in the $F_{\text{cr}} - \delta$ curve in Fig. 3.10(A). As the parameter δ is varied from 0.15 to 0.85, the corresponding values of critical force are calculated. From Fig. 3.10(A), it can be observed that the minimal critical force is obtained when the beam is actuated around the position where $\delta = 0.37$ (or the symmetric position where $\delta = 0.63$). Interestingly, since the influence of actuation position on critical force can be assumed independent of other design parameters, as made evident in Eq. 3.31, any precompressed beam tends to obtain its minimal critical force when its actuation position is given by $\delta = 0.37$ (or $\delta = 0.63$). This finding pertains to applications that require the actuating force to be small.

Moreover, the $w_{\text{cr}} - \delta$ relationship is captured in Fig. 3.10(C). As the actuation position

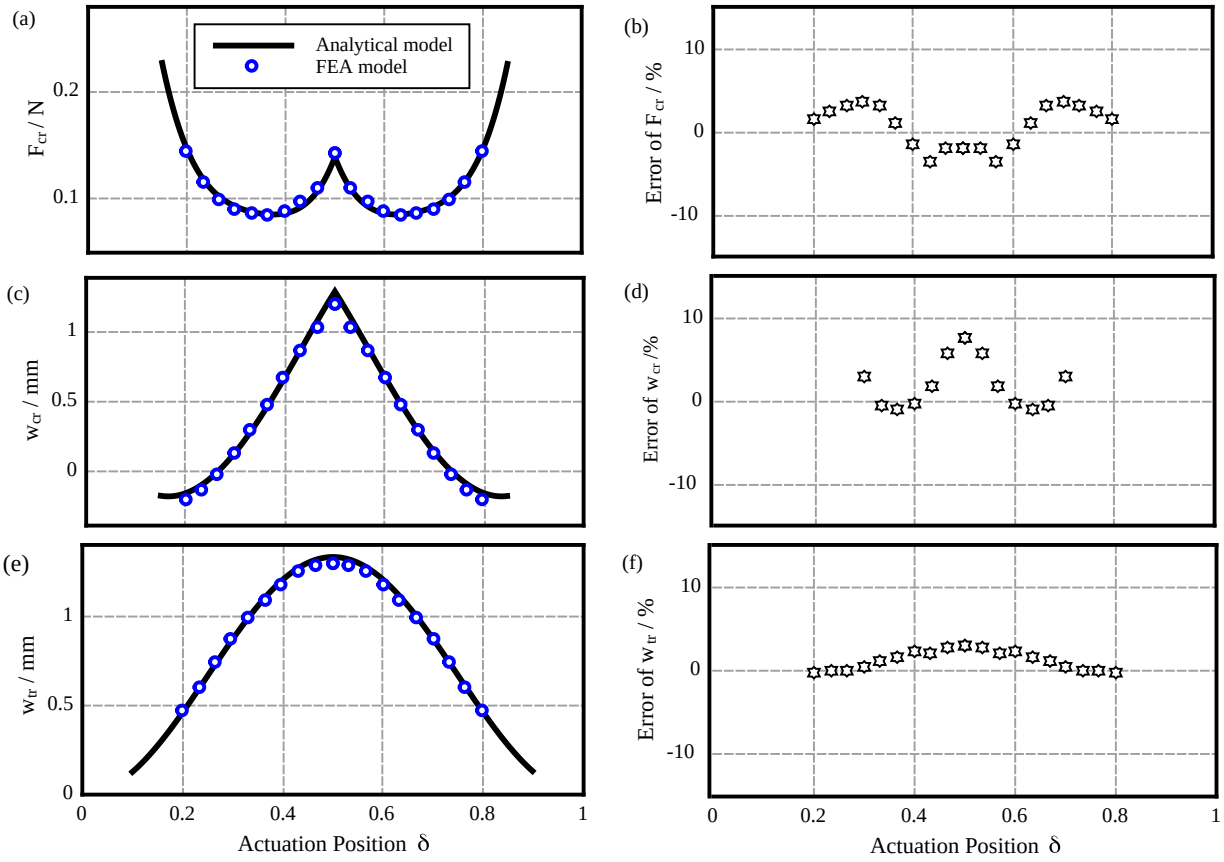

Figure 3.10: Effect of actuation position δ on the critical behavioral values. (A) Critical force F_{cr}; (B) Error of F_{cr} compared with FEA results; (C) Critical displacement w_{cr}; (D) Error of w_{cr} compared with FEA results. Note that a part of data is not shown here; (E) Travel w_{tr}; (F) Error of w_{tr} compared with FEA results.

moves from the beam's endpoint to its midpoint, the critical displacement increases, with its increment rate increasing. Note that the displacement is calculated with respect to the x-axis.

Lastly, when the design parameters of the beam are held constant, the mathematical relationship between the travel w_{tr} and δ simply features the cosine function discussed in Section 3.3.4.3, as shown in Fig. 3.10(E).

As depicted in the Fig. 3.10(A), (C) and (E), the $F_{\text{cr}} - \delta$, $w_{\text{cr}} - \delta$, and $w_{\text{tr}} - \delta$ curves generated from our model are also compared with those from the FEA model. In addition, the relative errors are presented in Fig. 3.10(B), (D) and (F). The relative errors of F_{cr} and w_{tr} with respective to the FEA simulation data are both bounded within 4%. The critical displacement w_{cr} calculated from our model matches excellently with the FEA simulation, even though the relative error is fairly notable when the actuation position largely deviates from the beam's center. Within this range, the relative error of w_{cr} is less informative and is not shown in Fig 3.10(D). However, in most applications, the actuation position parameter δ falls within the range $[0.37, 0.63]$ [90, 96, 99], where the errors of w_{cr} are bounded within 8%. Therefore, our model can be considered generally feasible and accurate.

Precompression. In order to increase the applicability of the following analysis, we define a parameter $r = \frac{d_0}{L_0}$ that denotes the precompression rate of a bistable buckled beam. Therefore, using the expressions $d_0 = rL_0$ and $L = (1 - r)L_0$, we derive the relationships among r and the behavioral parameters of a bistable beam. Applying Eq. 3.31, 3.33, and 3.35, we can obtain the relationships between F_{cr}, w_{cr}, and w_{tr} and the precompression rate r. These relationships are given as $F_{\text{cr}} \propto \sqrt{\frac{r}{(1-r)^5}}$, $w_{\text{cr}} \propto \sqrt{r(1-r)}$, and $w_{\text{tr}} \propto \sqrt{r(1-r)}$.

These mathematical relationships are demonstrated with a bistable beam with design parameters given in Table 3.2 and with δ set to 0.43. As shown in Fig. 3.11(A), (C) and (E), all of the three values increase as the precompression rate increases, with their increment rates decreasing. Again, as shown in 3.11(B), (D) and (F), the errors of our analytical model remain small (less than 9% for both F_{cr} and w_{tr}), with the exception of the critical displacement w_{cr} when the precompression rate r is very large. The enlarged error of w_{cr} when the precompression rate is large is due to the violation of the small-deflection hypothesis assumed in our model. The error of w_0, however, is bounded within 15% when r falls in the range $[0, 0.1]$, which indicates that our model still greatly applies to most circumstances [100–102].

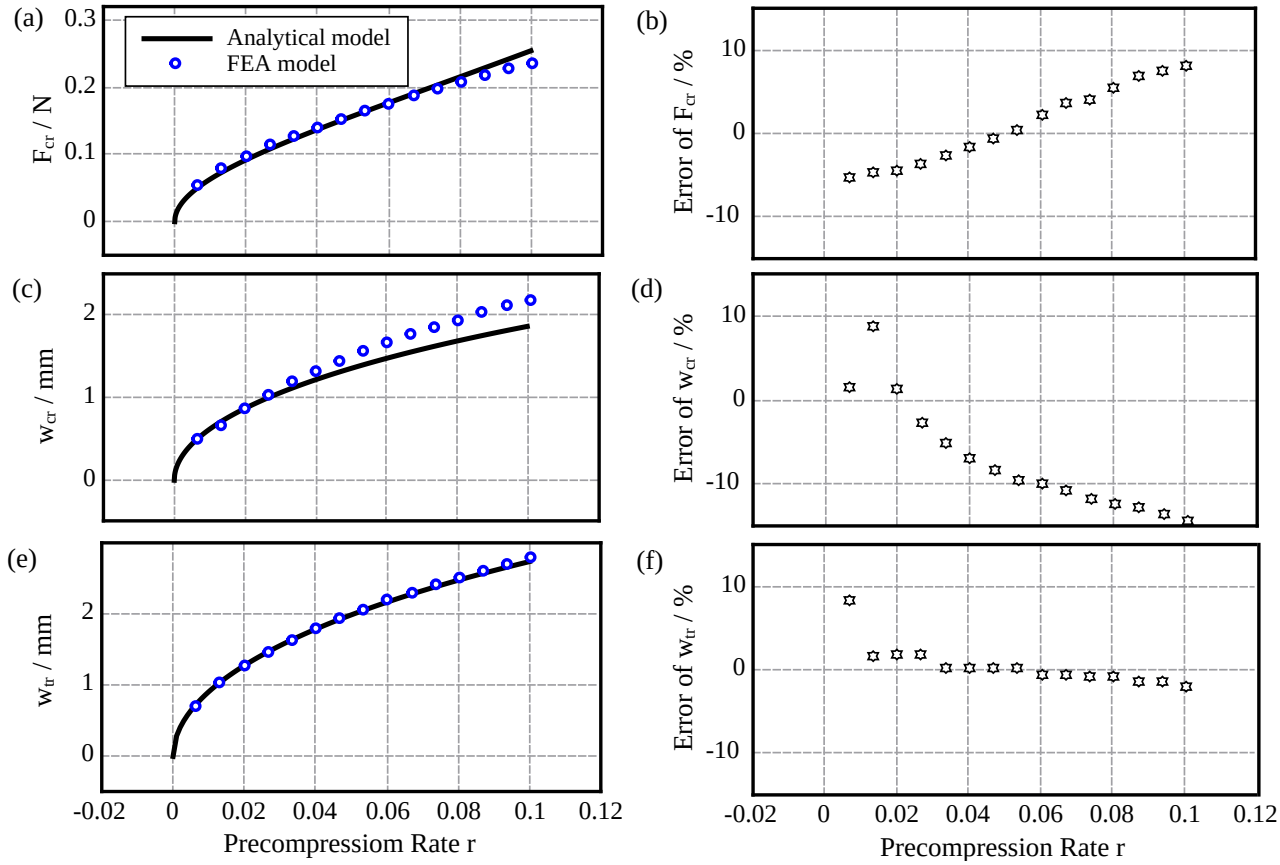

Figure 3.11: Effect of precompression rate r on the critical behavioral values. (A) Critical force F_{cr}; (B) Error of F_{cr} compared with FEA results; (C) Critical displacement w_{cr}; (D) Error of w_{cr} compared with FEA results (E) Travel w_{tr}; (F) Error of w_{tr} compared with FEA results.

3.4 Rapid Design and Evaluation

Our analytical model of the printable oscillator's oscillation period effectively guides the design of the system when a desired oscillation period is specified. Here we demonstrate one possible optimization algorithm that finds the set of design parameters that allows the printable oscillator to oscillate at a desired period and at the same time, maximizes the robustness of design and thus improves the manufacturability of the resulting system.

Importantly, users can customize their own, specific constrained optimization problems, with different degrees of freedom or parameters to be optimized, using the scheme to be discussed. The functionality of this algorithm is further demonstrated with a case study. It is worthy noting that we haven't validated the model against physical experiments.

3.4.1 Optimization Problem Formulation

3.4.1.1 Parameters and Constraints

We consider a printable oscillator with the following predetermined parameters: the temperature change compensation term c_{T}, the voltage across the actuator U, as well as the parameters γ_1, γ_2, γ_3, γ_4 that characterize the relationships between k, C_{th}, λ, and R and the length of the actuator x_0, as given in Eq. 3.5. Moreover, we assume that some design parameters, namely the thickness of the beam h, the Young's modulus E, and the actuation position μ, are predetermined by users. All of these aforementioned parameters are summarized in Table 3.3.

The remaining design parameters to be optimized include the width of the beam b, the original length L_0, the span L, and the length of the actuator x_0, all of which are subject to certain constraints. Constraints on b, L_0, and x_0 are specified by users, as shown in Table 3.3. Moreover, the analytical models of the snap-through characteristics in Eq. 3.31, 3.33 and 3.35 are highly accurate if the precompression rate is less than 8% [103], indicating an implicit constraint on L and L_0.

More constraints may be imposed on the parameters if the system has limitations for the critical snap-through force or critical displacement. For instance, if the system is unable to provide actuation force that exceeds a certain magnitude, another constraint on the design parameters may be relevant.

3.4.1.2 Optimization

As different designs of the printable oscillator may yield the same oscillation period, we choose the design with the highest robustness. Given the inevitable fabrication errors that would result in some inaccuracy in the values of design parameters, we want to minimize the ultimate error in the oscillation period T_{osc}. Fabrication tools such as laser cutters typically result in inaccuracy in the geometry of the beam, while manually cutting the actuator may result in inaccuracy in its length. Thus, the robustness of a set of design parameters is associated with the partial derivatives $\partial T_a/\partial b$, $\partial T_a/\partial L_0$, $\partial T_a/\partial L$, and $\partial T_a/\partial x_0$ when this set of parameters is adopted. Hence, our optimization problem minimizes the absolute values of these partial derivatives:

$$
\begin{aligned}
\underset{b,L_0,L,x_0}{\text{minimize}} \quad & \mathbf{g}^T \boldsymbol{\mathcal{E}} \mathbf{g} \\
\text{subject to} \quad & T_{\text{a}}(b, L_0, L, x_0) = T_{\text{osc}} \\
& b^{min} \leq b \leq b^{max} \\
& L_0^{min} \leq L_0 \leq L_0^{max} \\
& 0 \leq \frac{L_0 - L}{L_0} \leq 0.08 \\
& x_0^{min} \leq x_0 \leq x_0^{max}. \\
\text{with} \quad & \mathbf{g} = \nabla T_{\text{a}} = \left\langle \frac{\partial T_{\text{a}}}{\partial b}, \frac{\partial T_{\text{a}}}{\partial L_0}, \frac{\partial T_{\text{a}}}{\partial L}, \frac{\partial T_{\text{a}}}{\partial x_0} \right\rangle^T \\
& \boldsymbol{\mathcal{E}} = diag(e_b^2, e_{L_0}^2, e_L^2, e_{x_0}^2)
\end{aligned}
\tag{3.36}
$$

Note that we write T_{a} as a function of b, L_0, L, and x_0 for simplicity, but T_{a} also depends on the predetermined parameters in Table 3.3. $\boldsymbol{\mathcal{E}}$ contains the weight of each partial derivatives in the cost function $\mathbf{g}^T \boldsymbol{\mathcal{E}} \mathbf{g}$. The weights are given as the estimated fabrication error bounds for b, L_0, L, and x_0, which are dependent on the fabrication methods and therefore inputted by users. This optimization problem, with constraints and the weight matrix $\boldsymbol{\mathcal{E}}$ customized by users, can be solved with `fmincon` in MATLAB.

3.4.2 Case Study

We consider a printable oscillator whose predetermined parameters are given in Table 3.3. The bistable beam is made of polyester (PET) sheet, whose thickness and elastic modulus are 0.132 mm and 3 GPa, respectively. The actuation position parameter μ is chosen as 0.43 and the constraints on the geometry of the beam and the actuator are given in Table 3.3. The oscillation period is chosen as 4.0 s.

Since the bistable beam is folded from a 2D pattern fabricated with a laser cutter [90], the laser kerf, approximately 0.1 mm wide [104], may result in inacuracy in b, L, and L_0. We choose the error bounds of b, L_0, and L as twice of the width of the laser kerf. Meanwhile, we choose the error bound of x_0 as 0.6 mm, as cutting the CSCP actuator manually might involve larger error. Therefore, the entries in the weight matrix $\boldsymbol{\mathcal{E}}$, e_b, e_{L_0}, e_L, and e_{x_0}, are chosen as 0.2×10^{-3}, 0.2×10^{-3}, 0.2×10^{-3}, and 0.6×10^{-3}.

The values of b, L_0, L, and x_0 given by the optimization are 2.5 mm, 24.0 mm, 22.1 mm, and 52.8 mm, respectively. The robustness of this design is tested and compared with the robustness of another design that yields the same oscillation period ($b = 3.0$ mm, $L_0 = 15.0$ mm, $L = 14.5$ mm, $x_0 = 64.0$ mm). In Table 3.4, Case 1 and Case 6 represent ideal circumstances where no fabrication error occurs, while Case 2-5 and Case 7-10 represent those where there are significant errors in b, L_0, L, and x_0. There is an one-to-one correspondence between these cases, as the errors in these four parameters are exactly the same in Case 2 and Case 7 and this pattern holds in the other three pairs of test cases.

The small relative error in the oscillation period from Case 2-5 indicates that the parameters suggested by the algorithm feature high robustness in design. Even when fabrication errors are highly notable, we can still keep the error in the oscillation period within $\pm 10\%$. In Case 7-10 (compared to Case 6), the absolute errors in b, L_0, L, and x_0 are also 0.1 mm, 0.1 mm, 0.1 mm, and 0.3 mm, respectively, but these errors make the relative error in the oscillation period exceed 30% in multiple cases. Also, each of Case 7-10 has notably larger

Table 3.3: Parameters and constants in the optimization problem.

Parameter	Unit	Case Study
Predetermined Parameters :		
Mean Stiffness Const (γ_1)	N	9.34
Thermal Mass Const (γ_2)	$N/^\circ C$	9.06
Thermal Conductivity Const (γ_3)	$N/(s \cdot^\circ C)$	4.98
Resistance Const (γ_4)	Ω/m	277.67
Voltage (U)	V	7.64
Temperature Compensation (c_T)	$N/^\circ C$	0.0286
Beam Thickness (h)	mm	0.132
Beam Young's modulus (E)	GPa	3.0
Actuation Position (μ)	1	0.43
Constraints :		
Min Beam Width (b^{min})	mm	2.5
Max Beam Width (b^{max})	mm	3.5
Min Beam Length (L_0^{min})	mm	12.0
Max Beam Length (L_0^{max})	mm	24.0
Min Actuator Length (x_0^{min})	mm	40.0
Max Actuator Length (x_0^{max})	mm	100.0

relative error than their corresponding case from 2-5. These observations indicate that our arbitrary choice of design parameters has much lower robustness.

Importantly, these robust design parameters are obtained nearly instantly by running the optimization algorithm on a typical personal computer, while conventional parameter exploration would have been extremely time-consuming. It is worth noting that the validation of

model against physical experiment hasn't been done yet.

Table 3.4: Example test cases that demonstrate design robustness.

	Case	b mm	L_0 mm	L mm	x_0 mm	T_{osc} s	Error %
	1*	2.5	24.0	22.1	52.8	4.00	0
	2	2.4	24.1	22.2	53.1	3.97	-0.75
Optimized	3	2.4	24.1	22.0	52.5	4.26	+6.50
	4	2.6	23.9	22.0	53.1	4.13	+3.25
	5	2.6	23.9	22.2	52.5	3.64	-9.00
	6*	3.0	15.0	14.5	64.0	4.00	0
	7	2.9	15.1	14.6	64.3	3.83	-4.25
Naive	8	2.9	15.1	14.4	63.7	5.40	+35.0
	9	3.1	14.9	14.4	64.3	4.28	+7.00
	10	3.1	14.9	14.6	63.7	2.65	-33.8

Note: * represents ideal cases while the others refer to cases where there are significant errors in b, L_0, L, and x_0.

3.5 Conclusion and Discussion

We have proposed a rapid design method for printable oscillator, a complex dynamic electromechanical system composed of a bistable buckled beam and CSCP actuators. Based on a quasi-static model, we have developed an analytical expression for our printable oscillator's oscillation period. With this analytical expression, the design of printable oscillator from desired behavioral specifications is formulated into a constrained optimization problem, which takes as input predetermined parameters of the system and, after performing optimization

instantly, outputs a set of design parameters that allows the printable oscillator to oscillate at the desired period and maximizes the robustness of the design.

The analytical models and rapid design formula also apply to origami logic (see Section 4.5.3). Beyond the scope of the printable oscillator discussed in this work, our design method may apply to other dynamic electromechanical systems satisfying the quasi-static assumption. For instance, we can replace the CSCP actuator with shape memory alloy (SMA) actuator [105] or replace the bistable beam with a monostable beam [106]. Given the high simplicity and flexibility of our method, we believe that our work can facilitate the modeling, designing, and prototyping of many complicated dynamic compound systems with similar basic configurations to that of printable oscillator.

CHAPTER 4

Origami Logic and Autonomous Interaction

This chapter has been partially adapted from one journal article (1), and one conference paper (2). The text of the publication was modified to fit within the format of the thesis, and the supplementary information of the publication integrated into the main text.

(1) **Wenzhong Yan**(✉), Shuguang Li, Mauricio Deguchi, Zhaoliang Zheng, Daniela Rus, and Ankur Mehta. "Origami-Based Integration of Robots that Sense, Decide, and Respond". *Nature Communications,* 14 (1), 2023 (Featured by the editors in a Collection and Focus).

(2) **Wenzhong Yan**(✉), Chang Liu, and Ankur Mehta. "Origami Logic Gates for Printable Robots". *IEEE/RSJ International Conference on Intelligent Robots and Systems*, pp. 6084-6089, Prague, Czech Republic, 2021.

4.1 Introduction

Recent advances in origami-inspired engineering have enabled intelligent materials and structures to process and react to environmental stimuli. Yet, almost all origami robots still rely on rigid semiconductor-based electronics and auxiliary transducers for sensing, computing, and actuation to interact autonomously with their environments [107]. This dependency often restricts the potentials of origami robots: (i) Equipping external semiconductor-based electronics requires system integration thus increasing the complexity and weight of the resulting robots. These disadvantages mainly result from the undesired information trans-

mission in the electro-mechanical interface [108]; (ii) The mismatch of stiffness between rigid electronics and the compliant bodies increases the difficulty of design, fabrication, and assembly [109]; (iii) Semiconductor-based electronics are typically vulnerable to adversarial environmental events, e.g., radiation and physical impact, which limit their applications [110]; (iv) The logistic needs on-site could restrict robotic rescuers involved in disaster reliefs and first aid in resource-constrained locations; (v) The dependency on semiconductor-based electronics might inhibit the promised accessibility of the folding-based method [111]. Therefore, it is desirable to develop an alternative method for origami robots to achieve autonomy by embedding sensing, computing, and actuation into compliant materials [112]. This may lead to a new class of origami robots, with levels of autonomy similar to their rigid semiconductor-based counterparts, while maintaining the favorable attributes associated with origami folding-based fabrication [107, 108, 113].

There have been increasing efforts in investigating the feasibility of integrating smart materials into origami structures and mechanisms to realize desired functionalities, including sensing, computing, communication, and actuation [114–118]. This parallels a broader exploration into non-traditional approaches to achieve information processing and control across a range of disciplines; this has led to the opportunity of using mechanical computing systems to augment traditional electronic computing systems [58] in various fields, including soft robotics [10, 54, 119–122], microfluidics [8, 53], mechanics [110, 123, 124], and beyond [125–127]. To autonomously interact with the environment through integrating smart origami materials, an analogical sense-decide-act loop that emulates the language and structure of conventional semiconductor-based architecture should be formulated. This requires (i) computing units that can process information [128], (ii) sensors that receive signals from the environment [129], (iii) actuators that execute commands to implement the response upon the feedback [130]. Furthermore, those three classes of components must form an ecosystem that accommodates both signal transmission and energy transduction. A few components and some of their assemblies have been demonstrated individually [108, 109, 117, 131, 132].

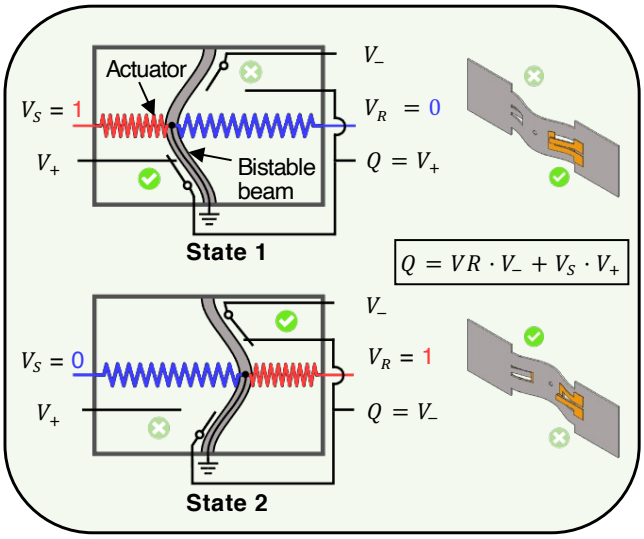

Figure 4.1: The fundamental building unit of the autonomous robot is the origami multiplexed switches (OMS). The OMS can select between two input signals (i.e., V_+ and V_-) and forward the selected one on-demand according to the selection signal V_S (with its complementary V_R).

However, it is still very challenging to build integrated autonomous origami robotic systems mainly due to the lack of suitable computing elements that can interface with available sensing and actuating components [131]. High resistance or energy loss of building components [133] and complicated fabrication [128] of current computing architectures also contribute in part to the challenge. To the best of our knowledge, origami robots have not been demonstrated that can autonomously interact with the environment with sensing, computing, and actuating capabilities fully embedded in compliant materials.

Here, we report an integrated process to create autonomous origami robots by using functional compliant, conductive materials, as illustrated in proposed design and fabrication process (see Figure 1.1). The origami multiplexed switch (OMS) is the fundamental mechanism that enables this potential (Fig.4.1); it takes an important step towards the highly integrated, untethered, autonomous origami robot concept shown in Fig.1.1A.

The OMS acts similar to a 2-to-1 multiplexer, selecting between two input signals and forwarding the selected one on demand. By incorporating bistable beams and conductive resistive actuators—conductive super-coiled polymer (CSCP) actuators [17], the OMS can control the state of conductive material networks embedded in compliant structures upon the electrical selection signals, enabling functionalities of switching, amplification, filtering, and memory storage. Based on the OMS, origami logic gates (i.e., NOT, AND, OR gates with functional completeness) are constructed with low output resistance; combinational logic and circuits, namely NAND and NOR gates, are also developed to demonstrate the capability of our system for cascading and more sophisticated computation (see Fig.4.9 for the fabrication processes). The electrical output combined with low internal resistance (order of 0.1 ohms) of origami logic makes it suitable for directly powering compliant actuators without the need for additional amplification or control electronics, enabling more applications with simple integration [123]. Therefore, the sense-decide-act loop necessary for autonomous interactions of robots can be built around the origami logic with widely available electrically-mediated sensing and actuating mechanisms [123, 134].

We demonstrate our method in three autonomous origami robots: (i) a Venus flytrap-inspired robot that can "distinguish" a living object from an non-prey stimulus and close its leaves to capture its "prey" (mimicking its natural counterparts) [135]. The robot is created by connecting two origami sensors through an origami Boolean logic gate to conductive thermal actuators in an integrated folding-based manner; (ii) an untethered cockroach-inspired crawler that can detect obstacles and execute decision-making to reverse its crawling direction. We show the capability of our process to interface with non-origami discrete electronic actuators with sensing and computing embedded in origami materials; (iii) an untethered two-wheeled car that locomotes with trajectories programmed in origami memory components, which allows non-volatile access and reprogrammability with origami logic. This work offers a way of embedding sensing, logic functions and simple control, and actuation directly into origami materials to generate autonomous compliant robots in a rapid manner. This

method opens a new design space of autonomous origami machines that are less systematically complex. The semiconductor-free and nonmagnetic nature of the resulting origami robots endows the potential to work in extreme environments (e.g., near/in magnetic resonance imaging (MRI) machines and nuclear plants) [117]. Our work is an important step toward highly integrated and robust untethered origami robots and intelligent machines.

4.2 The Origami, Multiplexed Switch

4.2.1 Mechanism and Design

An OMS acts as a 2-to-1 multiplexer that selects between two analog or digital input signals (V_+ and V_-) and forwards the chosen input based on a selection signal, V_S (and its complementary V_R, see Fig. 1.1B). The logic function of the OMS can be expressed as $Q = V_R \cdot V_- + V_S \cdot V_+$. The OMS mainly consists of one bistable beam and two CSCP actuators. One end of each actuator is attached to the bistable beam while the other is fixed on an origami framing. Thus, the actuators can drive the bistable beam switch between two stable states to control the on/off states of two electrical poles on the beam. When the beam is pulled by the left CSCP actuator, it snaps to the left stable state with the bottom pole closed and the top pole open, leading to an output $Q = V_+$. Otherwise, the output changes to V_-. The mechanism of the bistable mechanism is described in Fig.4.2. The snap-through instability endows the switch with three properties: (i) The state of the switch is binary ("open" or "closed"), which allows unambiguous control, regardless of the uncertainties resulting from the nonlinear contracting of the actuators [136]. This feature also enables it to function as a filtered touch sensor when the bistable beam is exposed to external mechanical stimuli [137] (ii) The switch requires power only when it changes between the two states; otherwise, it remains in the previous state, extensively reducing energy consumption [110]. The state of the switch is controlled by a pair of CSCP actuators [17]; the switch changes its states when the corresponding actuator drives the bistable beam reaching its switching

point. The CSCP actuator acts as a thermal actuator and can be driven through Joule heating (similar to shape memory alloy actuators).

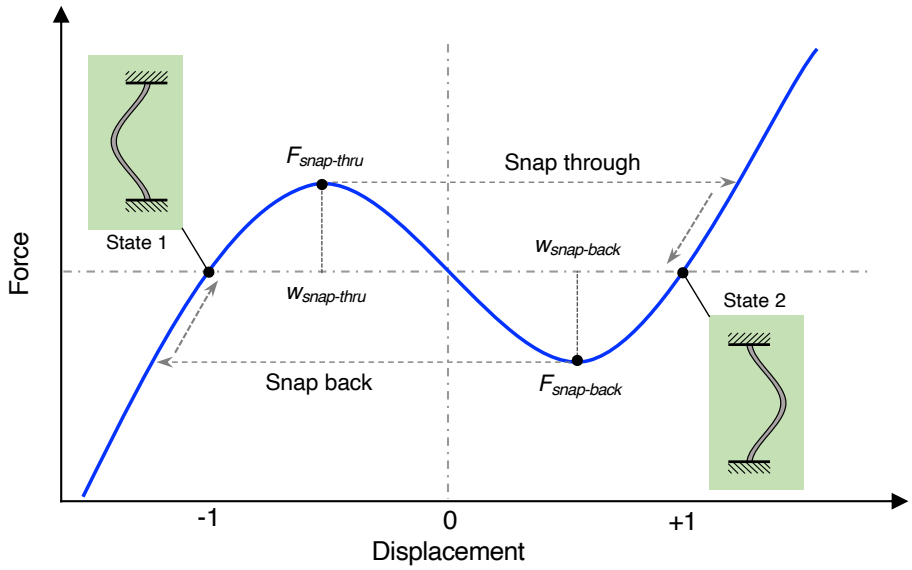

Figure 4.2: Mechanism of a bistable buckled beam. The bistable beam has two symmetric stable states, i.e., state 1 and state 2. The centerpoint of the beam will snap through towards state 2 when its displacement exceeds $w_{\text{snap-thru}}$. Similarly, the beam will snap back state 1 when it is actuated to $w_{\text{snap-back}}$.

The design of the tabs (forming the poles) on the bistable beam is critical. The two tabs naturally rest as cantilever beams. When the beam is at either state, the beam compresses a corresponding tab while releasing the other. Thus, the compressed tab forces the corresponding pole consisting of two copper tape terminals closed. The length and the angle of the tabs can be chosen such that the contact starts and finishes within the snapping motion of the beam. The width of the tab should be configured to be capable of applying enough pressure on the pole to reduce contact resistance. Our optimized design of the tab has a width of 1.2 mm, a length of 4.0 mm, and a folded angle of about 30 degree. The folding line

of the tab is aligned with the boundary of the bistable beam (with its geometry parameters listed in Table 4.1).

Table 4.1: The set of parameters of the CSCP actuator and bistable beam for characterization.

Parameters	Unit	Value
CSCP actuator :		
Length (x_0)	mm	50.0
Diameter (D)	mm	0.71
Resistance (R)	ohm	2.79
Bistable beam :		
Length (L_0)	mm	14.9
Width (b)	mm	7.0
Thickness (h)	mm	0.127
Precompression (d_0)	mm	0.9

For the current design, we have an average ON resistance of 0.6 ohms and an OFF resistance of $\sim$1.2 megohms, resulting in a particularly high ON/OFF ratio ($\sim 10^6$). Also, the ON resistance is sufficiently low that it is suitable for the control of a wide range of robotic systems, which we demonstrate by using OMS or integrated devices to drive high-current CSCP actuators with low input voltage (less than 3 V). This low-resistance nature promises that the output signal of a logic unit can drive a large number of inputs of downstream logic gates without additional interfacing circuitry; this large fan-out endows our proposed architecture with the capability to build complex circuits and systems. Coupling the instability of the bistable beam and tab design leads to binary, opposite states of two poles ("open/closed") on the bistable beam, with hysteretic switching behavior (Fig. 4.27).

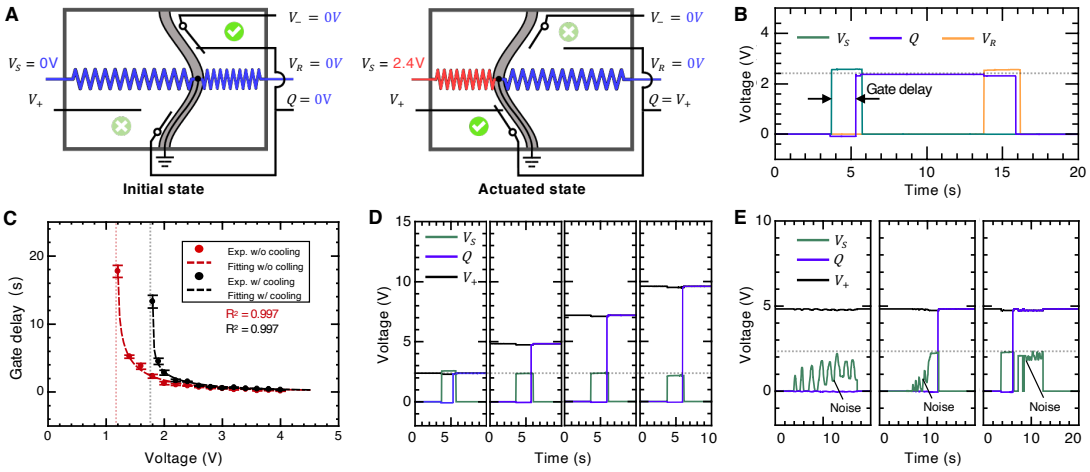

Figure 4.3: Characterization of OMS. (A) Two states of the OMS with labels of two inputs, V_+ and V_-, two control signals (V_S and V_R), and one output, Q. (B) Typical operation of the OMS with $V_S = 2.4$ V, showing a gate delay of about 1.5 s. Before the next cycle of operation, a voltage, V_R is applied to switch the bistable beam back to reset the OMS. (C) Gate delay of OMS as a function of selection voltage, V_S, with/without cooling air. Error bars represent standard deviations obtained from three separate experiments. (D) The output of the OMS for different supply voltages of V_S, functioning as a relay. (E) Response of the OMS to three pulses as control inputs, indicating its robustness to noise for binary operation. Random noise is superposed to all pulses at different phases.

4.2.2 Characterization

Figure 4.3A shows an OMS that acts as a multiplexer between two different sources of electrical power (V_+ and V_-). V_- is grounded ($V_- = 0V$) while V_+ is connected to a constant positive supply voltage. Initially, the beam rests at the right stable state, the output, Q, of the switch is 0V. When a control voltage V_S (= 2.4V) is applied, the beam snaps left, changing its output to the supply V_+. When the other control voltage, V_R, is applied to the right actuator, the beam snaps back and switches the output back to 0 V, resetting the OMS ready for the next cycle of operation. The corresponding voltage change of a typical cycle of the operation of the OMS is presented in Fig.4.3B. The output, Q, shows a lag behind

the control voltage, V_S, which is denoted as gate delay. With 2.4 V of control voltage, the gate delay is about 1.5 s. The gate delay mainly depends on the complicated interaction of mechanical, thermal, and electrical properties of the OMS; which can be captured by a simplified analytical model (see Section 4.5.3.1). For an OMS device with fixed geometry and materials, the delay is primarily determined by the amplitude of the voltage V_S and cooling conditions. We studied the dependence on these two factors (Fig.4.3 C). We first placed the OMS in the still air and varied the amplitude of the control voltage, V_S. By monitoring the output voltage of the OMS, we can characterize the gate delay as a function of the control voltage V_S (Fig.4.3C).

When the voltage was small, the actuator could not heat up to sufficient temperature to drive the bistable beam snap-through. As the voltage increased, once it exceeded the threshold value, the OMS became functional; the delay dropped monotonically as the voltage increased further, approaching its lower bound, about 0.1 s (see Section 4.5.3.2). By fitting the experimental results of the gate delay versus control voltage, we obtained the thermal mass, C_{th}, and absolute thermal conductivity, λ, of the actuator to be 4.48 $\times 10^{-2}$ Ws/°C and 1.13 $\times 10^{-2}$ W/°C, respectively. The fitting curve (the red dash line in Fig. 4.3C, $R^2 = 0.997$) indicates the lower bound of the voltage is around 1.19 V (from Eq.4.2), which is very close to our experimental observation, i.e., 1.2 V. In addition, the fitting curve suggests that the period asymptotically approaches a certain lower bound (0.1 s) with increasing supply power; however, real limits on the delay include snap-through duration, inertial dynamics (e.g., air damping), and electrical contact formation. To further reduce the gate delay, we can implement a bistable beam with a smaller timescale (see Section 4.5.3.2).

By adding a constant cooling air on the OMS, the voltage-delay curve remained similar with a voltage shift; the lower bound increased to 1.8 V (black data point, Fig.4.3C). The fit curve with cooling air (black dashed curve, $R^2 = 0.997$) matches well with the experimental data, indicating the thermal mass, C_{th}, and absolute thermal conductivity, λ, of the actuator to be 4.62 $\times 10^{-2}$ Ws/°C and 2.58 $\times 10^{-2}$ W/°C, respectively. The model suggests a

lower bound of around 1.80 V control voltage (from Eq.4.2), aligning with our experimental observation, i.e., 1.8 V.

Since the input circuit and control circuit are independent, the OMS can be used as a relay. Figure 4.3D shows the response of the switch to 10-s-long voltage pulses of $V_+ = 2.4$ V as the input signal and supply voltage rise to 9.6 V. The OMS relay can control the output with a voltage up to 4 times that of the control signal. This relay can also be used to control outputs with much higher voltages due to the electrical isolation of the input circuit from the control circuit.

The hysteresis of the beam makes the operation of this binary switch robust to noise. Noise in the control signal will not transmit to the output when it is moderate compared to the critical control voltage (i.e., 1.8 V). To demonstrate this property, we applied three types of voltage pulses of $V_+ = 2.4$ V to the left actuator (Fig.4.3E). The first signal is a 20-s-long constant voltage of 0 V accompanied by moderate noise. The output signal did not change since the control signal with noise was below the critical voltage. The second signal is a pulse with a maximum voltage amplitude of 2.4 V with noise added during the off-state. The noise did not affect the output until the control signal reached the critical switching value. The last signal is a pulse with a maximum voltage amplitude of 2.4 V with noise superposed during the on-state. After the output switched to its high voltage state, the noise did not alter its binary voltage value afterwards. It is worth noting the actual values of all outputs in Fig. 4.3E changed slightly when noise was introduced. This is mainly caused by the compliance of OMS devices; fluctuation in control signals could induce deformation on both the bistable beam and the base of the OMS, which leads to the variation of the pressure on contact pads and thus results in undulation in output signals. However, these tiny ripples would not change the binary output voltage values.

For continuous operation, the gates need to be reset after each computational execution. This reset not only includes toggling the bistable beam back to its initial stable equilibrium but also requires bringing down the actuators to ambient temperature. Thus, the delay

should be more clearly defined as the time taken for a fully reset gate to change its output upon input. Therefore, the switching speed (time duration between two executions) of such a gate needs to be sufficiently large to compensate for the cooling time required for actuators. As shown in Fig. 4.3C, we can achieve a minimal gate delay of about 0.1 s, which indicates a maximum switching speed of about 3.2 s with a cooling time of $\sim$ 3 s.

4.3 Origami Digital Computation and Memory Bit

4.3.1 Fundamental Logic Gates.

Based on the OMS, we can realize a functional-complete digital logic system that includes all three fundamental logic gates: NOT, AND, and OR. Here, we assigned voltage V = 3.0 V (for driving CSCP actuators of the display) the binary logic value "1" and voltage V = 0V the binary logic value "0". Note that these gates need to be reset every time for subsequent operation.

An Origami NOT gate was designed by configuring V_- as 1 and V_+ as 0, which provides the negation of the input signal A, i.e., V_S (Fig. 4.4A). V_R is assigned as reset R. Only when input A is 1, the output of NOT changes from 0 to 1 due to the snap-through of the bistable beam. We used a customized display to visually indicate the output of the gate (Fig. 4.4B). The display shows "1" when the output of the gate is 1, and vice versa.

Similarly, both AND and OR logic gates can be built by configuring the input voltage connections based on the OMS (Fig. 4.4C). The switch is configured as an AND gate by assigning V_S as A, V_+ as B, and V_- as 0 (Fig. 4.4C). In this configuration, only when both inputs A and B are 1, the gate outputs 1. The OR is constructed by rearranging the inputs and connections of the OMS in a similar manner (Fig. 4.4C); the OR gate will only output 0 when both A and B are 0.

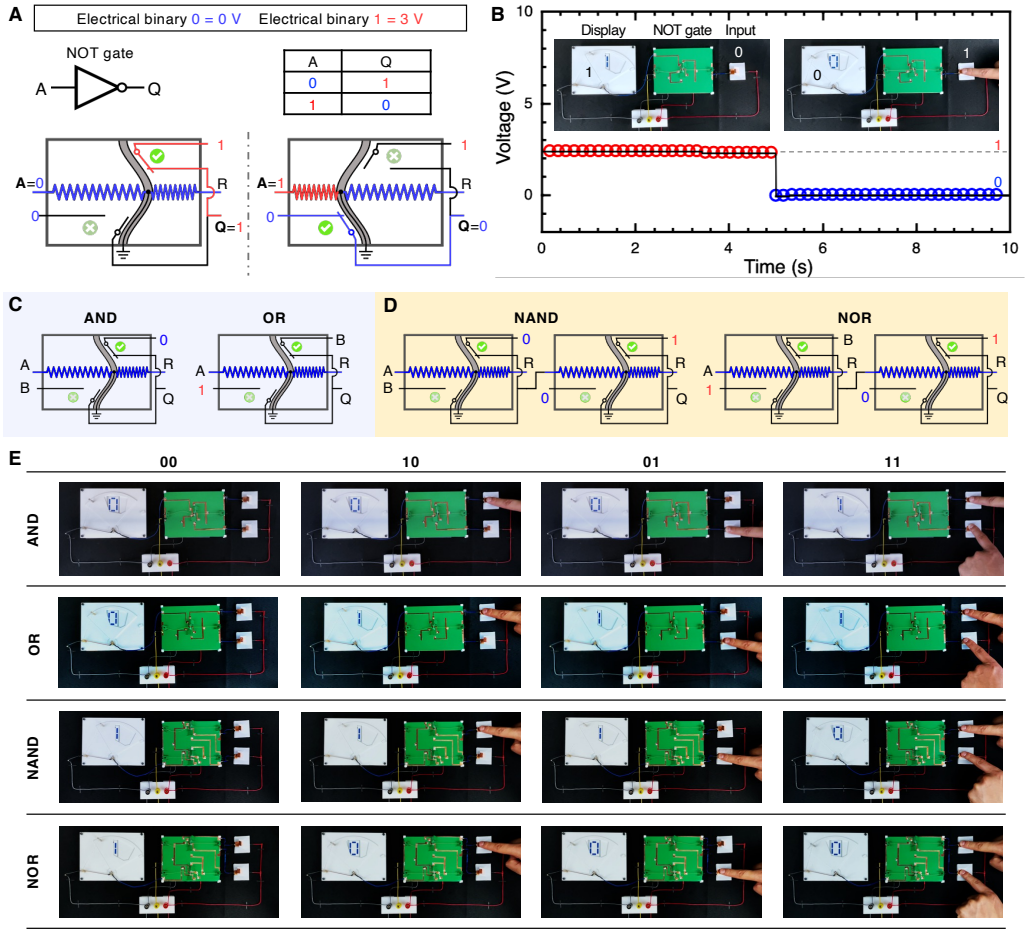

Figure 4.4: OMS-based digital logic gates. (A) An origami NOT gate. Logic diagram and truth table of a NOT gate. The schematic of an origami NOT gate in our architecture. (B) The input of the NOT gate is supplied by an origami switch; the output of the NOT gate is used to drive a CSCP actuator to change the reading ('0' or '1') of a display. (C) By configuring OMS, the other two fundamental logic elements, i.e., AND and OR gates, can be created. (D) Cascaded logic gates, i.e., NAND and NOR gates, could also be built by compositing two OMSs in series with specific configurations. (E) The full truth tables are demonstrated for the remaining logic elements, including AND, OR, NAND, and NOR gates.

4.3.2 Combinational Logic Gates.

So far, we have successfully implemented single logic gates, i.e., NOT, AND, and OR gates, which provide the basis for a functionally complete set of logical connectives. However, to create more complex functions, it is necessary to compose multiple logic gates. Thanks to the cascadable configuration and low internal resistance, we could compose several OMSs directly without requiring any intermediates, which greatly reduces the complexity, fabrication difficulty, and energy consumption of resulting systems. For example, we can construct composite logic gates, i.e., NAND and NOR, by integrating two OMSs (Fig. 4.4D). We demonstrated the logic operation of all the mentioned logic gates, including AND, OR, NAND, and NOR, experimentally with all four possible inputs (Fig. 4.4E). The remaining two basic logic gates, i.e., XOR and XNOR gates, can also be built easily in the same manner in Section4.5.1, although we have not implemented them experimentally in this paper. More complicated combinational circuits, e.g., a half adder, are possible by combining multiple logic gates. The ability to compose multiple logical functions into a more complex circuit enables the exploitation and integration of various sophisticated computation and control in digital electronics and robotics.

4.3.3 Nonvolatile Memory Bit.

Nonvolatile memory usually contains crucial programs of operation and can sustain power outages, making it essential components for autonomous control of robots. We build a simple origami Set-Reset latch with permanent storage capability upon the bistable switch design. The schematic of the S-R latch is shown in Fig. 4.5A, where $V_+ = 1$, $V_- = 0$. Meanwhile, V_S and V_R are reconfigured as SET and RESET, allowing the writing and erasing of information inside the memory device. A detailed demonstration is shown in Fig. 4.5B: After supplying power to the device, we wrote a bit 1 after 6 s. After about a 1.5 second delay, the output Q was modified to reflect the 1 input; this delay is the hold time of the latch. Then we

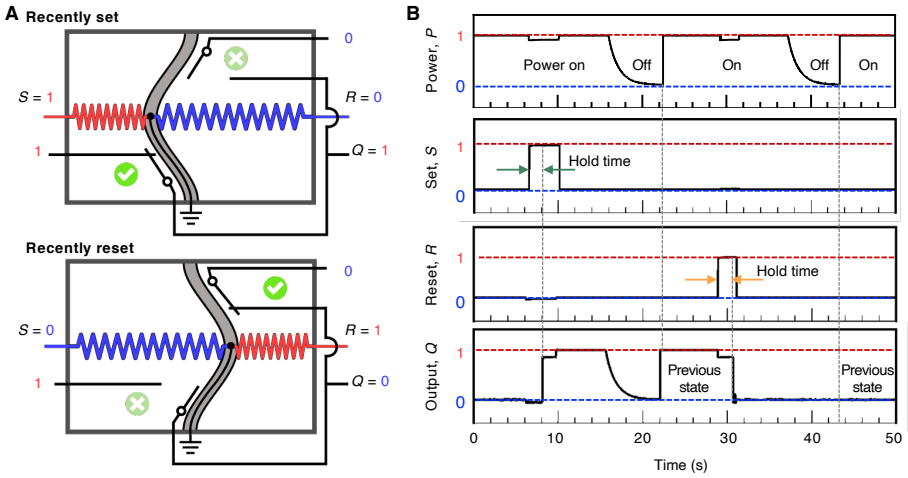

Figure 4.5: Origami memory bit. (A) An OMS is reconfigured as a set-reset latch for information storage. The S and R represent SET and RESET. If the latch is set, it outputs high voltage '1'; if reset, it yields low voltage, '0'. (B) Demonstration of writing, erasing, and nonvolatile memory of the lath with a featured hold time. The latch can sustain its recently written information after a power outage.

intentionally introduced a power outage, causing the output to drop to 0. However, we could still read the stored information after power was recovered. We could also delete/reset the memory (back to 0) by activating R with supplied power; the low voltage memory is not affected by the power outage as well. One memory device is capable of storing one bit, i.e., two states. With more memory units integrated, it allows for the storage of N = 2^n states where n is the number of bits.

4.4 Integrated Autonomous Robots with OMSs

To demonstrate the potential of the OMS in intelligent compliant devices and robotics, we used OMS-based components to control three origami robots: (i) Flytrap-inspired robot that can autonomously sense, decide, and respond to environmental stimuli, i.e., physical touch (Fig.4.6); (ii) untethered self-reversing legged robot that can detect obstacles and reverse its

locomotion direction (Fig.4.7); and (iii) an origami wheeled car can move with prescribed trajectories by utilizing reprogrammable origami memory (Fig.4.8). More details about the fabrication of robots are presented in Section4.5.1.

4.4.1 Flytrap-inspired Prey-catching Robot

The *Venus flytrap* is a carnivorous plant that is capable of distinguishing between living prey and non-prey stimuli (Fig.4.6A). The leaves (or trap) only close when there have been two stimuli of the trigger hairs within approximately 30 seconds; this closing strategy is to avoid inadvertent triggering of the trap by inanimate objects, e.g., fallen leaves, to save substantial energy. Here, we constructed a flytrap-inspired robot (Fig.4.6B, see Section 4.5.1.3 for more details) that partially imitates the prey strategy based on the proposed OMS. Although our robot does not consider the temporal information contained in stimuli, it can still be used to capture small "living prey" since an immobile object cannot activate both sensors. However, without including temporal information from stimuli, our robot cannot specify desired preys with a certain moving speed as its biological analogues [138]. Meanwhile, the robot can selectively catch a large prey since a small one is difficult to detect with both sensors. This robot consists of two origami touch sensors, one origami AND gate, and two CSCP actuators (in parallel). The schematic of the robot is detailed in Fig. 4.6C. It uses touch sensors to receive stimuli from the environment (Fig. 4.6D), which are then passed to the controller, i.e., an AND gate, for analysis. This results in an executable signal downstream to the CSCP actuators to control the open/closed states of the leaves. Only when two sensors are activated, the flytrap-inspired robot can "recognize" it as a living prey and "decide" to close its leaves to capture it by contracting CSCP actuators; otherwise, the CSCP actuators are kept inactivated with the leaves open (Fig. 4.6C). The touch sensor is modified from a bistable beam as shown in Fig. 4.6D, where a touch can trigger the snap-through of the bistable beam to change the on/off status of the circuit on it. Each sensor is integrated into the inner surface of two leaves (Fig. 4.6B). Two leaves are connected on the top surface of

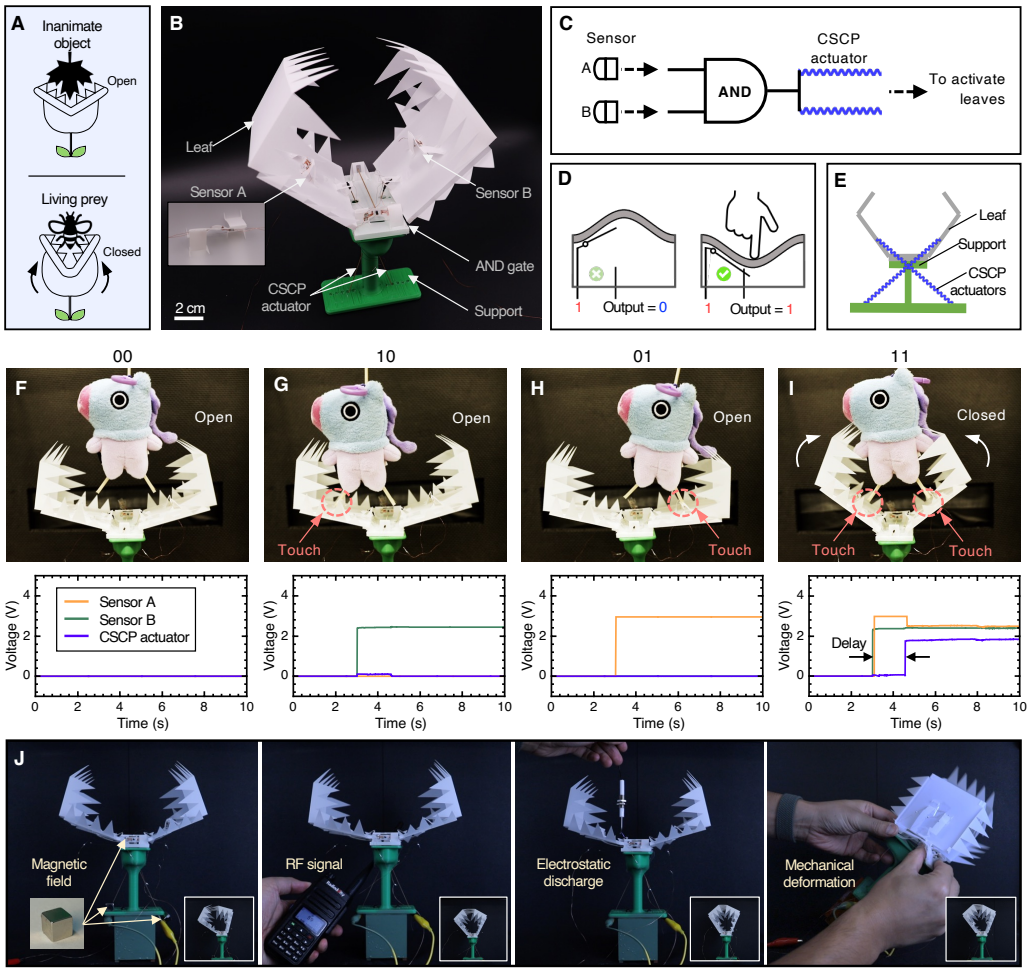

Figure 4.6: The origami flytrap-inspired prey-catching robot. (A) *Venus flytrap* can distinguish living preys from inanimate stimuli and close its leaves to capture preys. (B) The detailed structure of the robot with labels. (C) The simplified circuit diagram of the robot. (D) The schematic of a touch sensor modified from a bistable switch. (E) The actuation system of the flytrap-inspired robot. (F-I) Demonstration of a living 'prey' capture. (J) The origami flytrap-inspired robot could survive a strong magnetic field (0.47 T), intense radio frequency signal interference (power, 5W), high electrostatic discharge (output voltage $\geq$ 20kv), and large mechanical deformation (up to 50° bending and twisting) while its semiconductor-based counterpart malfunctioned under the same conditions.

the AND gate through origami tabs, which function as hinges of the motion of the leaves when driven by actuators. One end of each CSCP actuator is fixed on the bottom of a leaf while the other is attached to the support structure. Actuators are deployed diagonally for maximal actuation stroke (Fig. 4.6E).

To demonstrate, we used the flytrap-inspired robot to capture a living "prey" according to the interactions with an object (see Fig. 4.6 F to I). Initially, the leaves of the robot were open. Though the object fell into the trap, the robot did not close its leaves if the object did not touch any sensor (Fig. 4.6 F). Correspondingly, the output voltage of the circuit is 0 V, which indicates no contraction of the CSCP actuator. Even if the object activated one of the sensors, the robot would identify it as non-prey stimuli since single touch indicates immobility (see Fig. 4.6 G and H). Once the object is capable of triggering both sensors in two different positions, the robot would assume the object is moving "prey" and close its leaves to capture it (Fig. 4.6I). The voltage signals of sensor A, sensor B, and the CSCP actuator of the flytrap-inspired robot also suggests a successive capture with a delay of about 1.7 s (Fig. 4.6 F to I). The robot usually takes several seconds (e.g., 5 s in this case) to close its leaves due to system delay and low supply voltage (i.e., 2.4 V). Though the closing speed is out of the scope of this work, we can potentially improve it by two methods: (i) increasing the length of the CSCP actuators with higher supply voltage would increase the actuator speed [17]; (ii) incorporating mechanical snap-through mechanisms would further reduce the closing time, possibly down to 100 ms [139]. In this work, we chose our design based on clarity and simplicity.

The flytrap-inspired robot is fully fabricated through origami-inspired cut-and-fold out of sheet materials and conductive threads (except the 3D printed support structure i.e., its environment, though it too could be implemented in origami), which leads to semiconductor-free and nonmagnetic features, suggesting broad applications, especially in extreme environments, such as high radiation/magnetic fields, where typical semiconductor-based electronic components could not function [107]. Specifically, we operated the origami-based robot un-

der four adversarial environmental events, i.e., static magnetic field (0.47 T), radio frequency (RF) signal (power: 5 W), electrostatic discharge (ESD, output voltage $\geqslant$ 20Kv), and mechanical deformation (up to 50° bending and twisting). The results show that our robot could perform the designed task robustly (see Fig.4.6 J) while its semiconductor-based counterpart malfunctioned or even failed permanently. Although not directly tested, radiation damage to semiconductor-based devices has long been identified and well-researched [140], which also indicates the advantage of our approach in such environments. Moreover, our origami-based robots compare favorably against their semiconductor-based analogs, especially in terms of weight and cost, quantifying the benefits of our method (see Section4.5.4). In addition, there are applications where the delicate touch and intelligent capture of a soft gripper are desired, e.g., sampling brittle sea animals [141, 142]. In most cases, these grippers require external manual control from operators to execute a capture order. Instead, our robot could be used as a smart alternative to automatically recognize and capture living fragile animals without requiring human intervention or additional decision-making components; this new strategy can potentially simplify system complexity and improve operation robustness to semiconductor-based electronics unfriendly environments.

4.4.2 Untethered Self-reversing Legged Robot

Collision avoidance is one of the most essential needs of biological agents when exploring the environment, which is achieved by collecting information and thus responding upon analysis. For example, cockroaches rely on tactile sensing for perceiving physical objects to explore a neighborhood since most cockroach species are nocturnal [143]. Specifically, a cockroach can achieve collision avoidance by sensing obstacles with the antennae on their heads. To demonstrate our method, we designed an untethered self-reversing legged robot that can reverse its locomotion upon detecting obstacles inspired by the behavior of collision avoidance of cockroach (Fig. 4.7A).

This cockroach-inspired untethered legged robot is mainly composed of two touch sensors

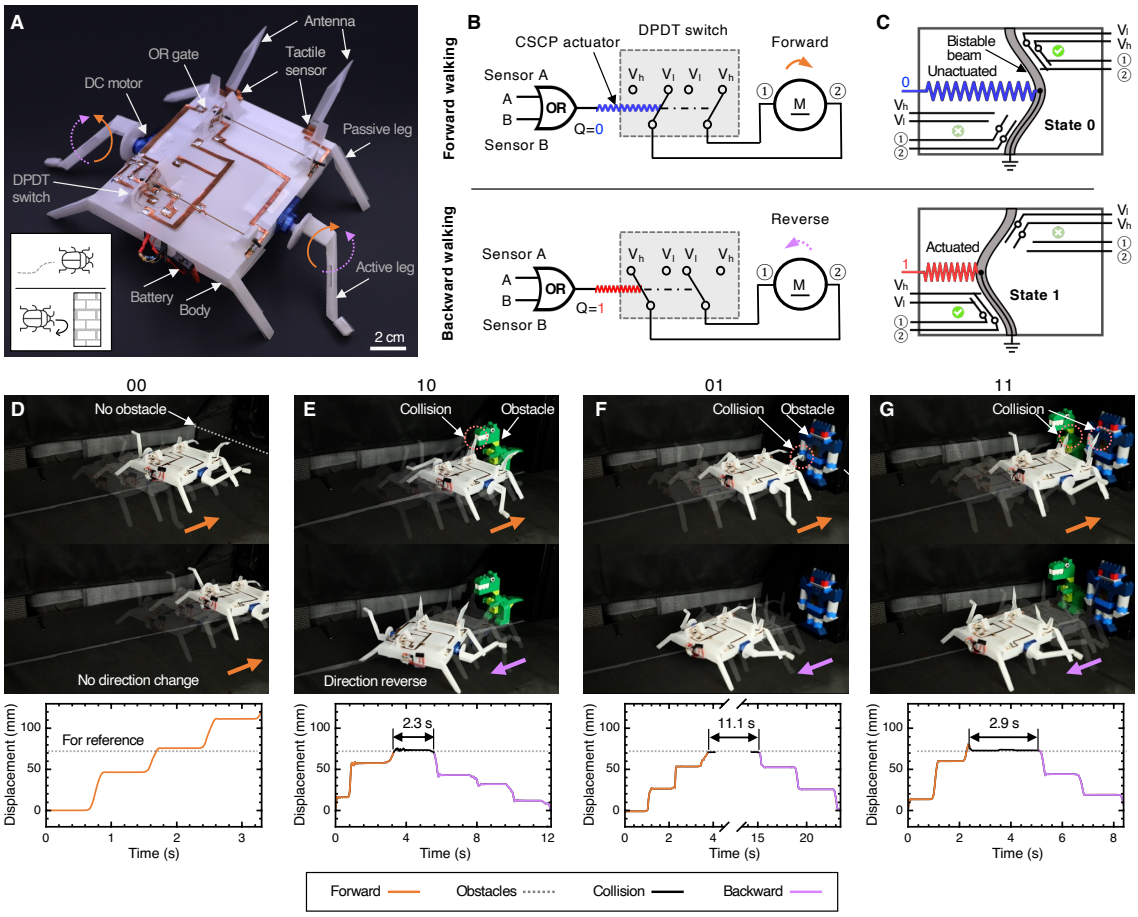

Figure 4.7: The cockroach-inspired self-reversing legged robot. (A) The detailed structure of the legged robot with labels. (B) The simplified circuit diagram of the legged robot. The information from the two tactile sensors on antenna decides the output of the origami OR gate; the output of the gate is used to determine the actuation of the CSCP actuator, which could potentially change the rotation direction of DC motors through a DPDT switch. (C) The schematic of an origami DPDT switch modified from the OMS. The switch of the states of the bistable beam changes the direction of rotation of the motors between counterclockwise and clockwise. (D-G) The legged robot encountering obstacles. Top: overlaid sequential images shows the crawling direction; bottom: displacement curves of the robot. Images and displacement curves are both derived from videos.

A and B (with the corresponding antenna), one on-board origami controller, two modified DC motors, and one lithium battery (see Section 4.5.1.2 for more details). The simplified schematic of the robot is presented in Fig.4.7B. The touch sensor consists of two initially disconnected copper strips, which could be forced closed upon the collision of the antenna to transit voltage signal to the on-board origami controller. This origami controller consists of an OR gate, a CSCP actuator, and a double-pole double-throw (DPDT) switch (see Fig.4.7C). This DPDT switch is modified from the OMS by adding another set of circuits on the bistable beam (see Fig.4.7C). This switch controls the current flow direction between four ports by toggling between two different states (corresponding to counterclockwise or clockwise rotation of the legs.) Once the OR gate is triggered by the signals from sensors (and antennae), its high output voltage will drive the CSCP actuator to toggle the DPDT switch to change the rotating direction of DC motors to reverse the locomotion (see Fig.4.7B). Figure 4.7 (D to G) shows key frames of the behavior of the legged robot in different environments. When there is no obstacle, the robot can continuously move forward. However, the robot would reverse its direction when either antenna (representing 10 or 01 for inputs of the OR gate) or both antennae (representing 11 for inputs of the OR gate) detect obstacles.

The sensing, computation, and control were done on-board the robot, demonstrating a system with semi/autonomous behaviors that can be integrated into the body of an origami robot. There are various applications where semiconductor-free self-reversing robots are of special interest. For example, the resulting crawler is of great potential for tasks, such as exploration and rescue, in extreme areas (e.g., high radiation fields).

Although the periodic actuation of the legs could have been generated by origami oscillators themselves [117], in this instance we used conventional components (in the form of DC motors used to generate motion), demonstrating the general interfacing allowing our systems to co-exist in existing robot ecosystems.

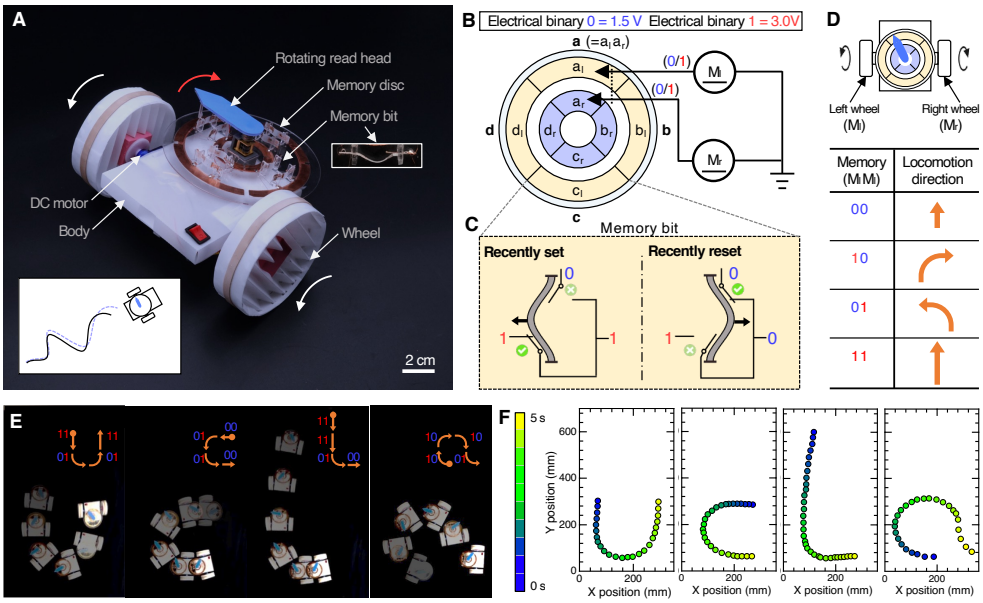

Figure 4.8: Origami wheeled car. (A) The detailed structure of the origami car with labels. The rotating read head extracts the stored memory (voltage) from the disc and forwards that to two DC motors to control the locomotion direction of the car. (B) The simplified circuit diagram of the wheeled car. Each composite memory bit consists of two basic memory bits, which control the corresponding wheels through two DC motors. For example, composite memory bit, a, is composed of two basic memory bit, a_l and a_r; a_l is used to control the left wheel (M_l) while a_r is for the right one (M_r). (C) The schematic of a basic memory bit. (D) The locomotion direction of the car is determined by the composite memory bit; the trajectory of the car is controlled by the sequence of memory bits. (E) Overlaid sequential images (derived from video frames) visualize the trajectories of the car (programmed with different locomotion plans: 'u', 'c', 'l', and 'a'. (F) X-Y position of the car in (E).

4.4.3 Untethered Origami Car with Reprogrammable trajectories

Robots that autonomously locomote along specified open-loop trajectories can serve as platforms for practical applications, e.g., detecting hazardous leakages with gas sensors equipped or executing a surveillance function with cameras on a well-defined route [144]. Here we de-

sign an origami wheeled car (see Fig.4.8A, see Section 4.5.1.4 for more details) that can follow designed trajectory patterns by reading from an origami memory disc composed from OMSs; a sequence of information (bits) written in the disc is extracted by the rotating read head and then sent to two DC motors to propel the origami car. By varying the memory, the car can drive along different prescribed trajectories.

The disc is mainly composed of four composite memory words, i.e., |(A)|(B)|(C)|(D)|; each word consists of two memory bits to control the corresponding pair of motors, respectively (see Fig. 4.8B). For example, the word (A) contains a_{l} and a_{r} (i.e., (A)=$\mathrm{a_l a_r}$); a_{l} is to control the left motor ($\mathrm{M_l}$) for driving the left wheel while a_{r} is for the right one through $\mathrm{M_r}$. When the written information in the memory bit is 0 (representing low voltage, 1.5 V), the corresponding wheel rotates slow; otherwise the wheel spins fast from memory 1 (high voltage, 3.0 V). The basic memory bit (see Fig. 4.8C) is modified from the origami Set-Reset latch (see Fig. 4.5). The origami car has four fundamental locomotion modes due to the combination of two basic memory bits (see Fig.4.8D). When both wheels receive the same information, the car moves straight forward (if both 0, the car moves slowly; if both 1, it locomotes fast). Otherwise, the car would either turn left (01) or right (10) to change the locomotion direction.

To demonstrate, we programmed the origami wheeled robot to follow the locomotion paths of the letters "u", "c", "l", and "a", respectively, to illustrate its trajectory specification (see Fig.4.8E). The X-Y position information of the trajectories was extracted from the video and shown in Fig.4.8F with the time mapped as color. Between operations, the memory in the disc needs to be erased and rewritten by switching the states of the bistable beam of the basic memory bits. For example, the memory was set to be |(A)|(B)|(C)|(D)| = |11|01|01|11| for the path of "u"; it was reprogrammed as |00|01|01|00| for that of "c". In the same manner, the memory was modified as |11|11|01|00| and |10|10|10|01| for "l" and "a", respectively.

Currently, the switching between two states of the basic memory bit is manually manipulated for simplicity. The automation of the memory writing could be done by incorporating

programmable controlling mechanisms, e.g., CSCP actuators (actuated by voltage signals, see Fig.4.5A) or through magnetic fields (with magnetic beads on the bistable beam) [145]. The origami car can have 256 ($= 2^8$) different trajectories based on the current design of the memory disc (four 2-bit memory words, i.e., 8 memory bits in total). To achieve locomotion with more sophisticated trajectories, we could (i) increase the physical density of the memory on the disc to expand the number of words in the memory bank, increasing the complexity of the representable trajectories; and (ii) increase the depth of the memory, extending each word to include more bits, e.g., $a_d \rightarrow (A)=a_l a_r a_d$ to control the rotation direction (clockwise or counterclockwise) of the motors and thus the overall locomotion direction (forward or backward) of the car. Such additional bits could be integrated through the origami DPDT switches to control the flow of current through the actuators (see Fig.4.7C). When further equipped with sensing capabilities, the origami car could presumably execute meaningful tasks such as route surveillance and radioactive leakage detection in nuclear power plants. The dependence on a DC motor to drive the memory read head could be eliminated by using linear sliding instead of rotating brushing; for example, a head (driven by a linear actuator, e.g., CSCP actuator) could slide over a memory tape to extract the stored information.

4.5 Materials and Methods

4.5.1 Fabrication of Origami-inspired Devices

4.5.1.1 Fabrication of OMS and Logic Gates

The OMS and logic gates share the same fabrication process (see Fig.4.9). Here we use an origami NOT (see Fig.4.11) as an example to demonstrate the fabrication method; the detailed creation of each logic can be found in Fig.4.10-4.15. This also similarly corresponds to that of the crawler (Fig.4.18), flytrap-inspired robot (Fig.4.20), and origami wheeled car (Fig.4.23). The fabrication of the NOT is mainly done in three stages: (i) origami cut-and-

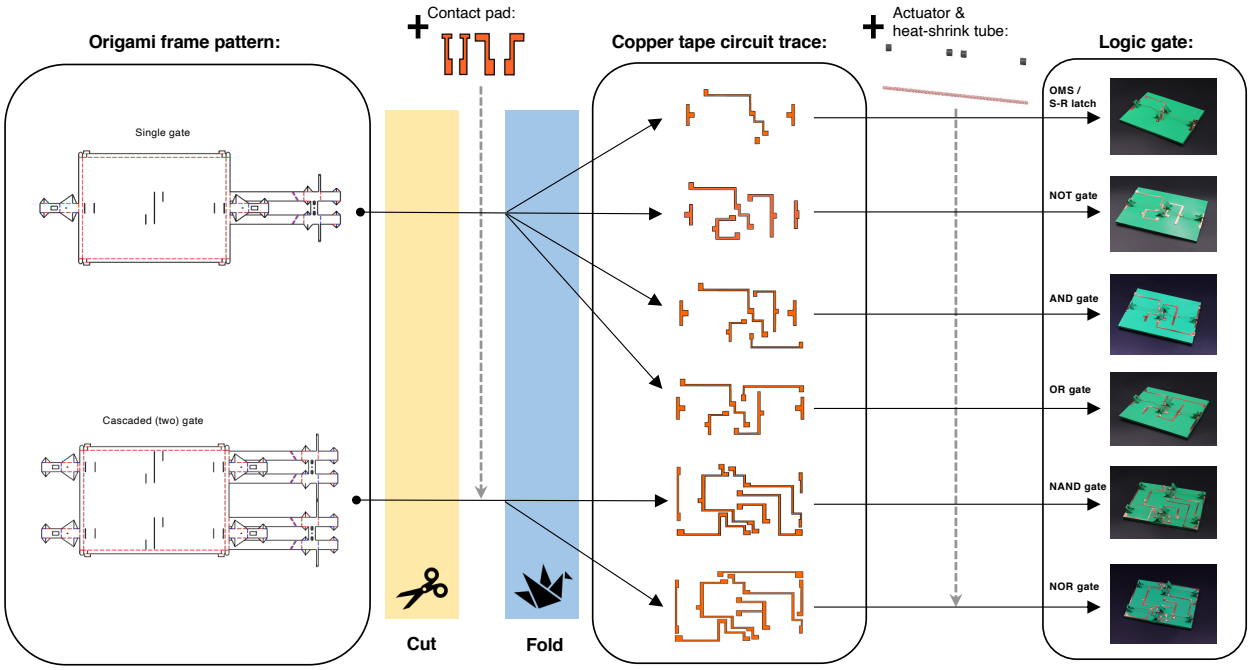

Figure 4.9: A generalized process of creating OMS-based devices. The fabrication process includes three major steps: (i) cut-and-fold 2D pattern to create origami frame; contact pads are attached on the bistable beam before folding, (ii) affix the copper circuit traces onto the base of the folded frame, and (iii) install CSCP actuator(s) and complete the circuit of the device.

fold (with contact pads attached), (ii) attaching copper tape circuit traces, and (iii) assembly of CSCP actuators.

The NOT gate is firstly constructed by patterning a flexible, polyester film (DuraLar^{TM}, Grafix Plastics) with a cutting machine (Silhouette CAMEO 2, Silhouette America, Inc.). The 2D fabrication pattern of the NOT is shown in Fig.4.11A, where the red and blue dashed lines indicate mountain and valley folds, respectively. Before folding, the contact pads are attached to the tabs; otherwise, it would be very challenging to fix them on the buckled beam (Fig.4.11C). The contact pads were partnered in such a fashion that the lower extruding rectangular parts, were facing away from one another. After partnering them, the

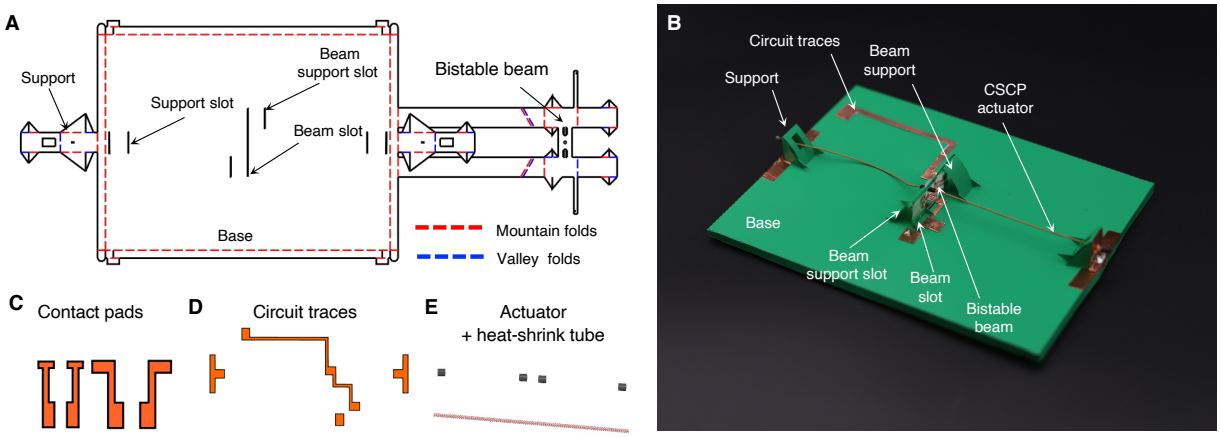

Figure 4.10: Design and assembly of the OMS / S-R latch. (A) 2D pattern of its origami frame. (B) Assembled origami OMS / S-R latch. (C) Contact pads. (D) Circuit traces. (E) CSCP actuators and heat-shrinking tubes.

smaller, T-shaped piece was attached to the thin, center, stick-like, cut out of the beam and the top edges of the T were wrapped around to ensure adhesion. Next, the z-shaped piece was directly attached to the beam with its upper rectangular piece being placed underneath the previous T-shaped pad, creating electrical contact between the two surfaces. Thus the two pads only contact when the bistable beam is at a certain stable state.

The origami frame is then folded from a planar base and various out-of-plane structures; these structures can be visualized in Fig.4.11B, indicated by the two supports along the boundary and the beam support through the center. These structures are folded in a weaving manner, coming up through a slot from below the base and folding back down through the various support slots to form the arches. By using origami features as connectors, we can minimize the resources required to assemble the devices. More fabrication details of this class of origami devices can be found in [146].

Secondly, we place the copper tape circuit traces (see Fig.4.11D) on the base of the origami framing (Fig.4.11B) while connected with contact pads through copper wires. The

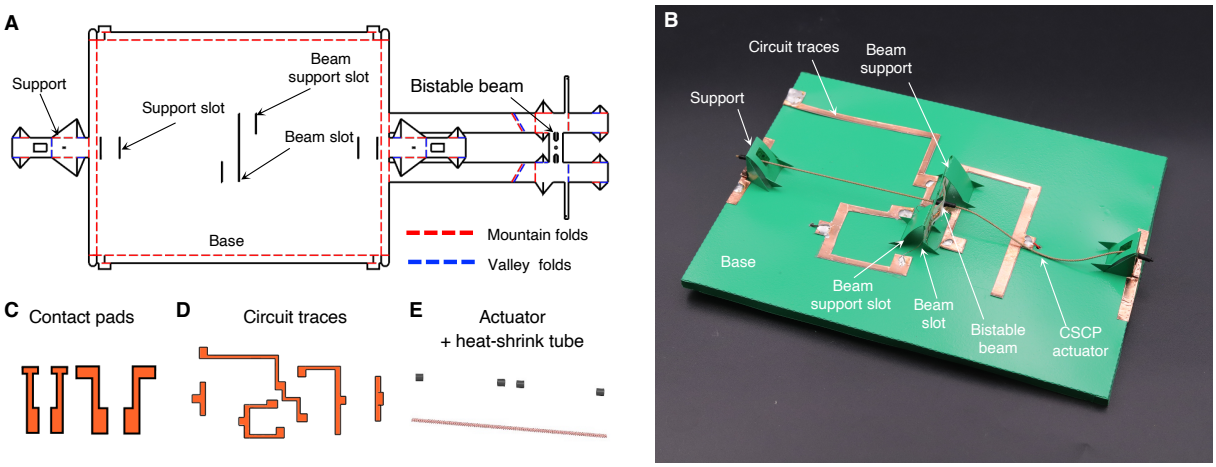

Figure 4.11: Design and assembly of the NOT gate. (A) 2D pattern of the origami frame. Red dashed lines represent mountain folds and blue lines are valley folds. (B) Assembled origami NOT gate. (C) Contact pads. (D) Circuit traces made of copper tape. (E) CSCP actuators and heat-shrinking tubes.

widths of copper traces could vary since they have very high conductivity compared with other electrical components, e.g., CSCP actuators. For convenience, we use about 3mm traces. Although it would require extra effort and care during folding, these copper traces can also be laminated onto the PET sheet before folding. For simplicity, we chose to install them after folding. Lastly, we install the actuator onto the resulting structure. One terminal of the CSCP actuator was fixed to the beam by using a piece of heat-shrink tubing (7496K81, Insultab) on either side. The other terminal of the actuator was similarly fixed to the support structure through another heat-shrink tube. Each of the exterior ends of the actuators was then connected to the circuit traces using thin copper wires, completing the electrical connection of the circuit.

The XOR and XNOR gates can be created in the same manner as shown in fig.4.16 and 4.17).

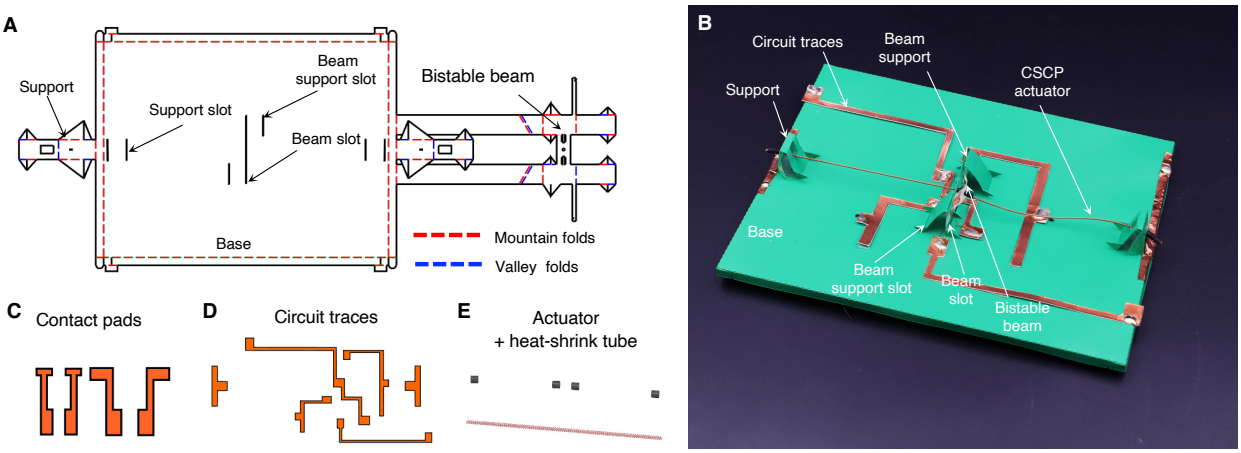

Figure 4.12: Design and assembly of the AND gate. (A) 2D pattern of the origami frame. (B) Assembled origami AND gate. (C) Contact pads. (D) Circuit traces. (E) CSCP actuators and heat-shrinking tubes.

4.5.1.2 Fabrication of the Legged Robot

The origami crawler consists of body, legs, antennae (with embedded touch sensors), origami controller, and a 3.7-V Lithium battery. (i) The body was firstly constructed by folding in accordance with the manually-designed patterns shown in Fig.4.18; the various components were then mounted together into their designated slots, completing the crawler's body. (ii) Circuit traces, including contact pads, were then cut and placed on the body (see Fig.4.19 for the detailed circuit diagram). The sensing antenna function by completing one path of the circuit when contact is made against a surface. Consistent, sustained contact is necessary in order to trigger the corresponding reversal mechanism; thus magnets were placed underneath the surface of the upper body and just in front of the antenna. These magnets guarantee a solid connection between the two contact pads, once a sufficient force has been applied for the magnetic force to bring the antenna to the body. Alternative methods were explored, such as that of a bistable beam, but much larger forces were required to trigger such switches. (iii) One CSCP actuator was incorporated in nearly the same manner as described for the NOT

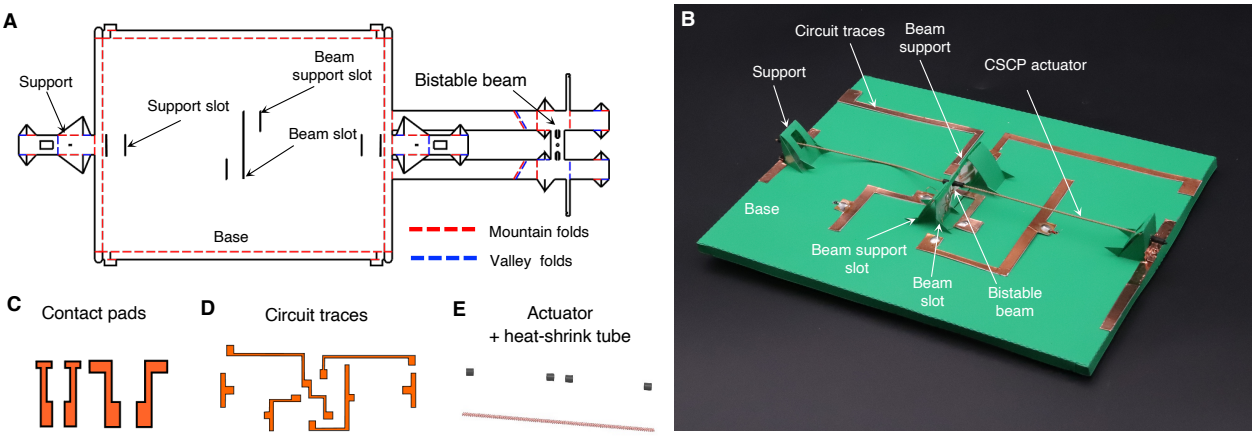

Figure 4.13: Design and assembly of the OR gate. (A) 2D pattern of the origami frame. (B) Assembled origami OR gate. (C) Contact pads. (D) Circuit traces. (E) CSCP actuators and heat-shrinking tubes.

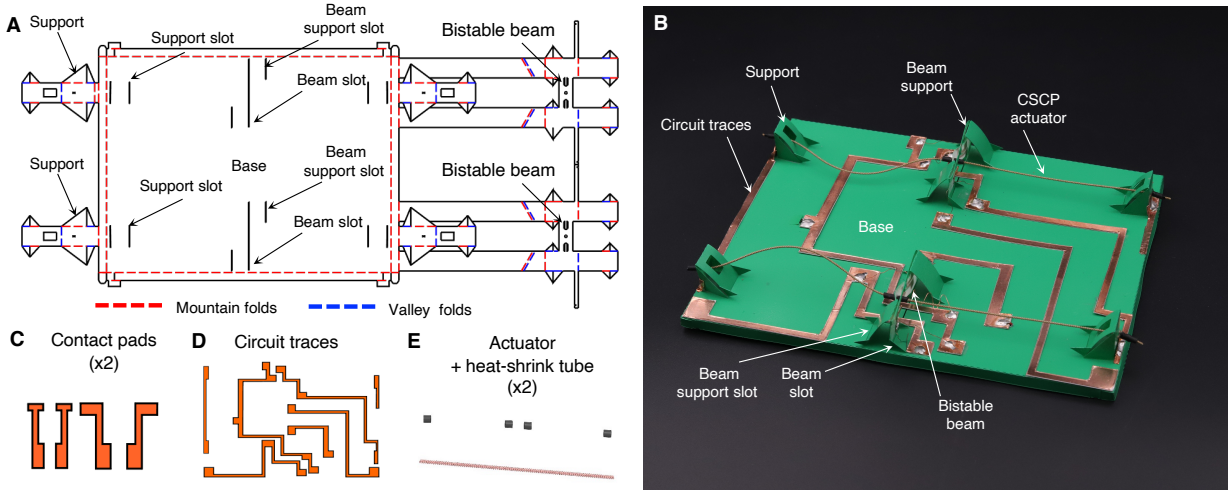

Figure 4.14: Design and assembly of the NAND gate. (A) 2D pattern of the origami frame. (B) Assembled origami NAND gate. (C) Contact pads. (D) Circuit traces. (E) CSCP actuators and heat-shrinking tubes.

gate with a single key distinction, only one support is required since the beam itself can act as an attachment point with manual reset. Another CSCP actuator was similarly attached

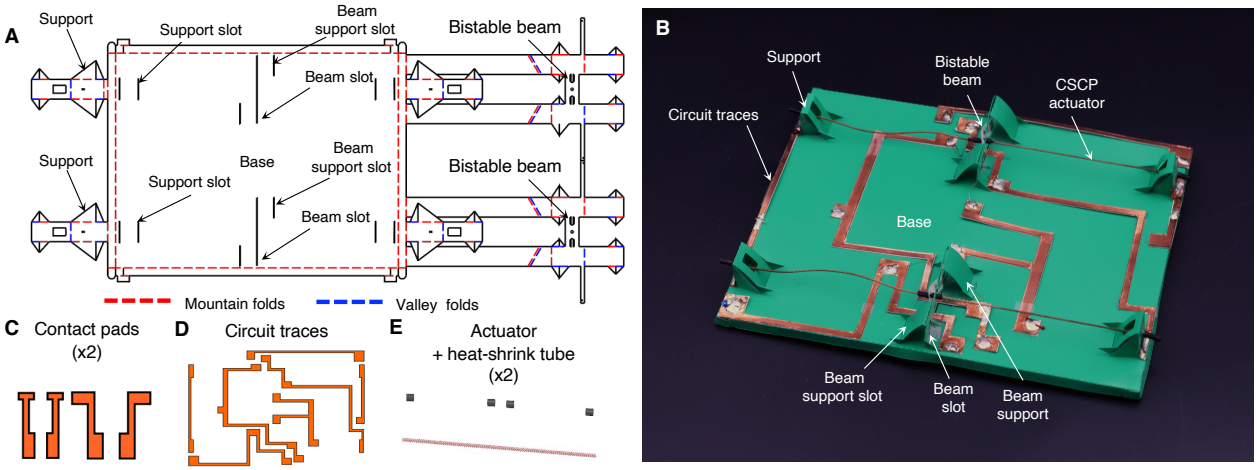

Figure 4.15: Design and assembly of the NOR gate. (A) 2D pattern of the origami frame. (B) Assembled origami NOR gate. (C) Contact pads. (D) Circuit traces. (E) CSCP actuators and heat-shrinking tubes.

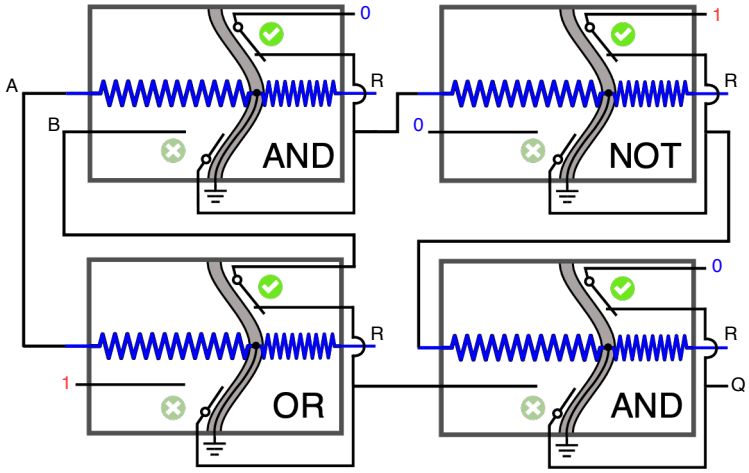

Figure 4.16: The schematic of origami XOR gate based on OMSs. The XOR gate consists of two AND gates, one OR gate, and one NOT gate.

to the DPDT switch to alter the state of the switch. (iv) Next, the various electronic components including a battery, a power switch, an 8-ohm resistor, and two DC motors (FS90R, Pololu Corporation) were embedded into the circuit as shown in Fig.4.19. Much of

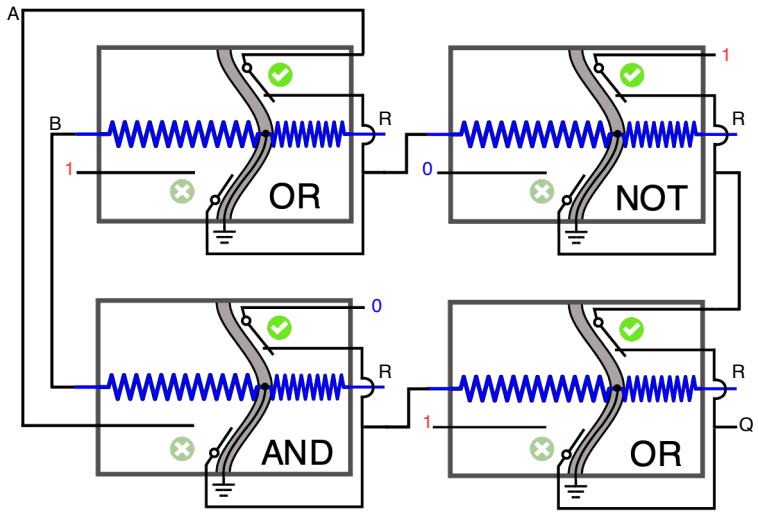

Figure 4.17: The schematic of origami XNOR gate based on OMSs. The XNOR gate consists of two OR gates, one AND gate, and one NOT gate.

the wiring is taken care of by the printed circuit trace pattern with these various components being implemented in series with the circuit, in the empty middle layer of the crawler. The active legs were attached to the output shafts of the motors to complete the assembly.

4.5.1.3 Fabrication of the Flytrap-inspired Robot

The fabrication of the flytrap-inspired robot and the crawler robot shares a similar process to that of the origami NOT described above. The robot contains an AND gate (without reset mechanism) at its central base as shown in Fig.4.20A. Its corresponding folding pattern is shown in Fig.4.20C. The outer leaves were then attached to the central switch through the leaf-base connections (see Fig.4.20A and B). These connections use double rib tabs, similar to those previously mentioned for the various beams and supports, to support the opening and closing of the leaves. A touch sensor, based on the bistable switch, is formed on the center of each leaf by adhering the contact pads shown in Fig.4.20C to both bistable beams. The outputs of the two sensors are connected to the two inputs of the AND gate (see Fig.4.6B). Then, the actuators are threaded through the holes indicated in Fig.4.20C

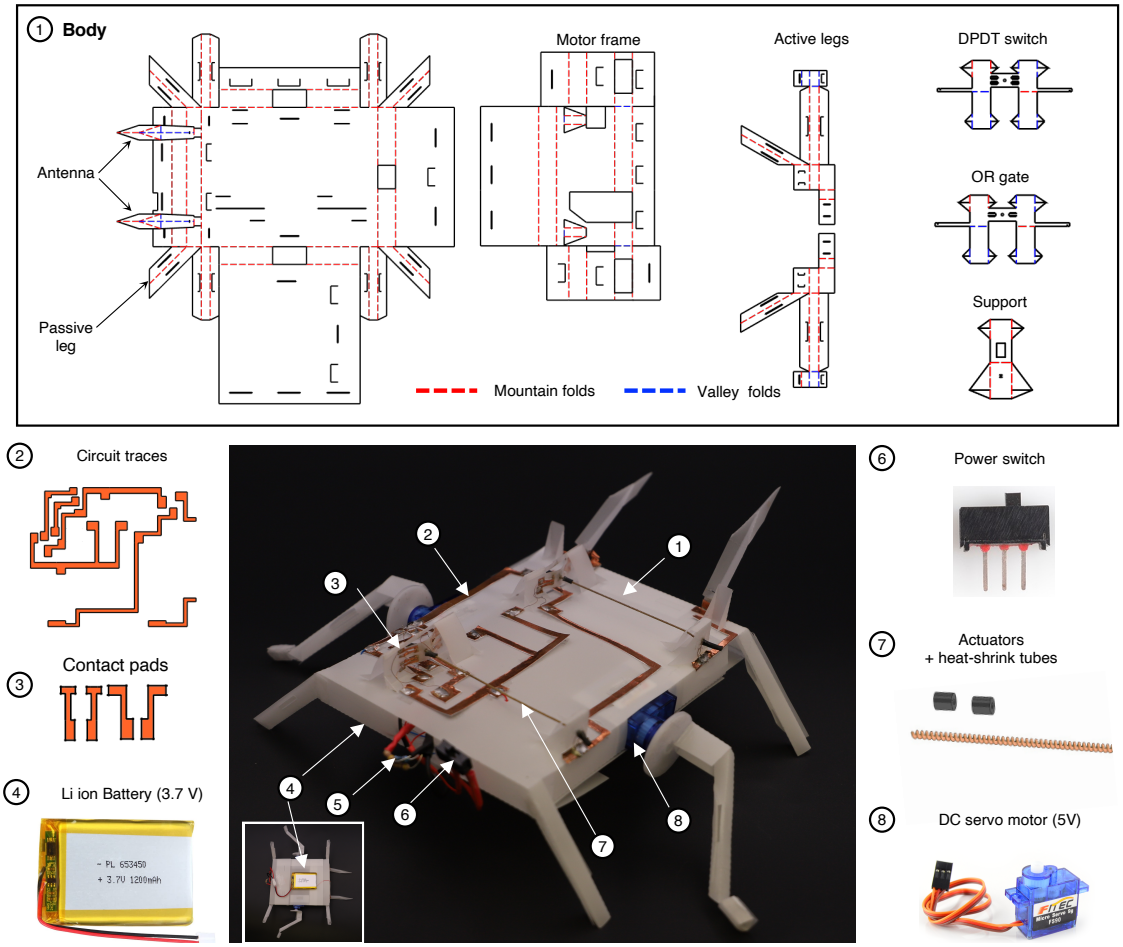

Figure 4.18: Design and assembly of the legged robot. 2D pattern of the origami structures and a list of necessary components are presented.

and tethered to the bottom platform (in green) and the support structure on the leaf itself, using shrink tubes. When the actuators contract, the leaves rotate along with the hinges on the connections to capture living "prey". The complete circuit diagram of the robot can be found in Fig. 4.22.

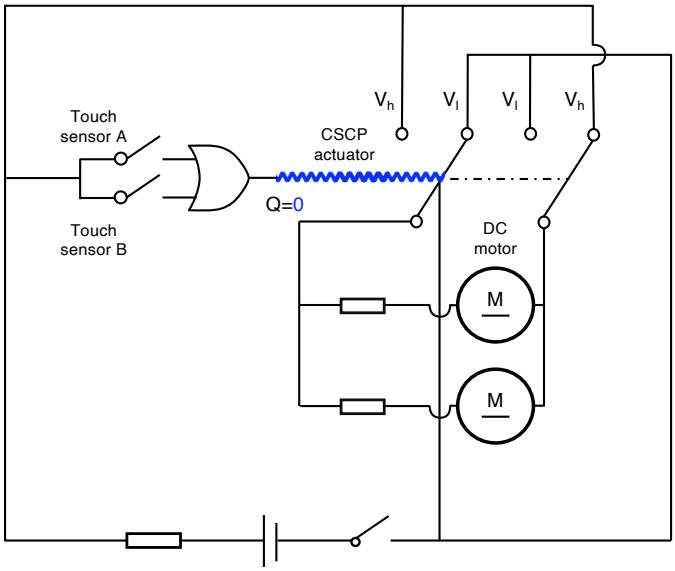

Figure 4.19: Circuit diagram of the legged robot. Two touch sensors perceive external information and send that as a voltage signal to the OR gate; the output (voltage) of the gate, in turn, is used to activate the CSCP actuator that are used to change the rotation direction of DC motors through a DPDT switch.

4.5.1.4 Fabrication of the Origami Wheeled Car

The origami wheeled car consists of three major parts: one origami body, one memory disc, and two corrugated wheels (see Fig.4.8A). The body of the car was folded from a PET sheet with the 2D pattern shown in Fig.4.23A. The motor frame is designed to hold the DC motors (FS90R, Pololu Corporation) that are used to drive the wheels. To improve the stiffness of the wheels and the robustness of locomotion, we adopted a corrugated wheel design [147]. One rubber band was attached to each wheel to increase the friction to prevent sliding for stable locomotion. The key component of the car is the memory disc with its corresponding 2D pattern in Fig.4.23C; it includes supporting disc, bistable memory bits, and associates. The supporting disc was cut from a 1.5mm-thick clear acrylic sheet by a laser cutter (Speedy 300 flexx, Trotec). The basic memory bits sharing a similar design as OMS were fixed on the supporting disc through customized beam supports; this modular design can reduce

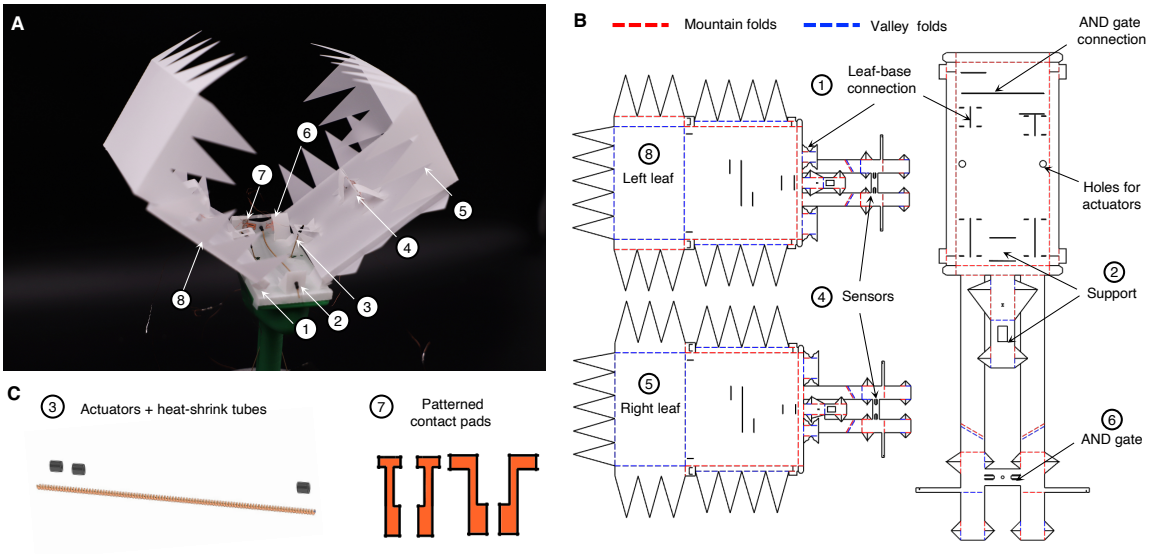

Figure 4.20: Design and assembly of the flytrap-inspired prey-catching robot. (A) The detailed structure of the robot with labels. (B) 2D fabrication pattern of the origami body of the robot. (C) CSCP actuators and contact pads.

fabrication difficulty. The information (voltage) of memory bits are read by the rotating head driven by a gearbox motor (HP 6V, Pololu Corporation, attached on the disc through the center motor slot); the sliding brushes on the read head extracted the signal through the electrical contact with the copper sliding rings (see Fig.4.23D). We also specially designed a two-channel slip ring to enable the information transmission from the rotating read head to stationary motors on the car. The detailed circuit diagram of the origami car is present in Fig.4.24, though only one composite memory bit (including two basic bistable memory bits) is shown in Fig.4.24A.

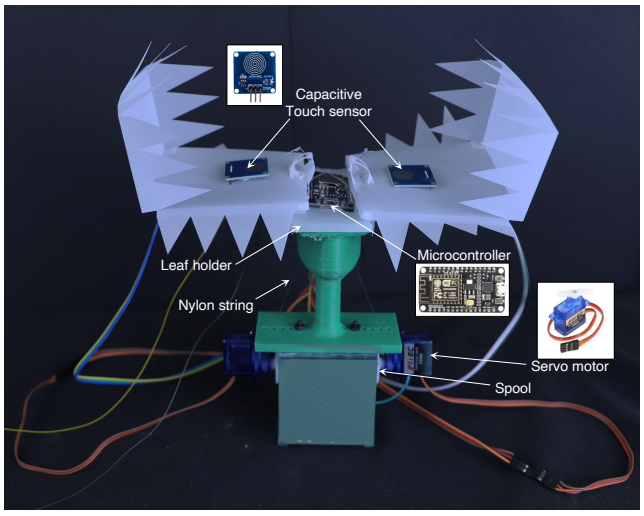

Figure 4.21: Design and assembly of the traditional flytrap-inspired robot with semiconductor-based control. We built this traditional robot to compare with the origami-based counterpart in term of the complexity, cost. weight, and robustness to adversarial environmental events.

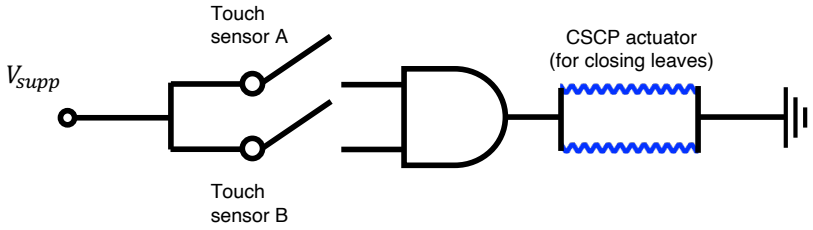

Figure 4.22: Circuit diagram of the flytrap-inspired prey-catching robot. The information from the two touch sensors on the leaves determines the output of the origami AND gate; its output is used to decide the actuation of the two CSCP actuators, which could contract to close the leaves.

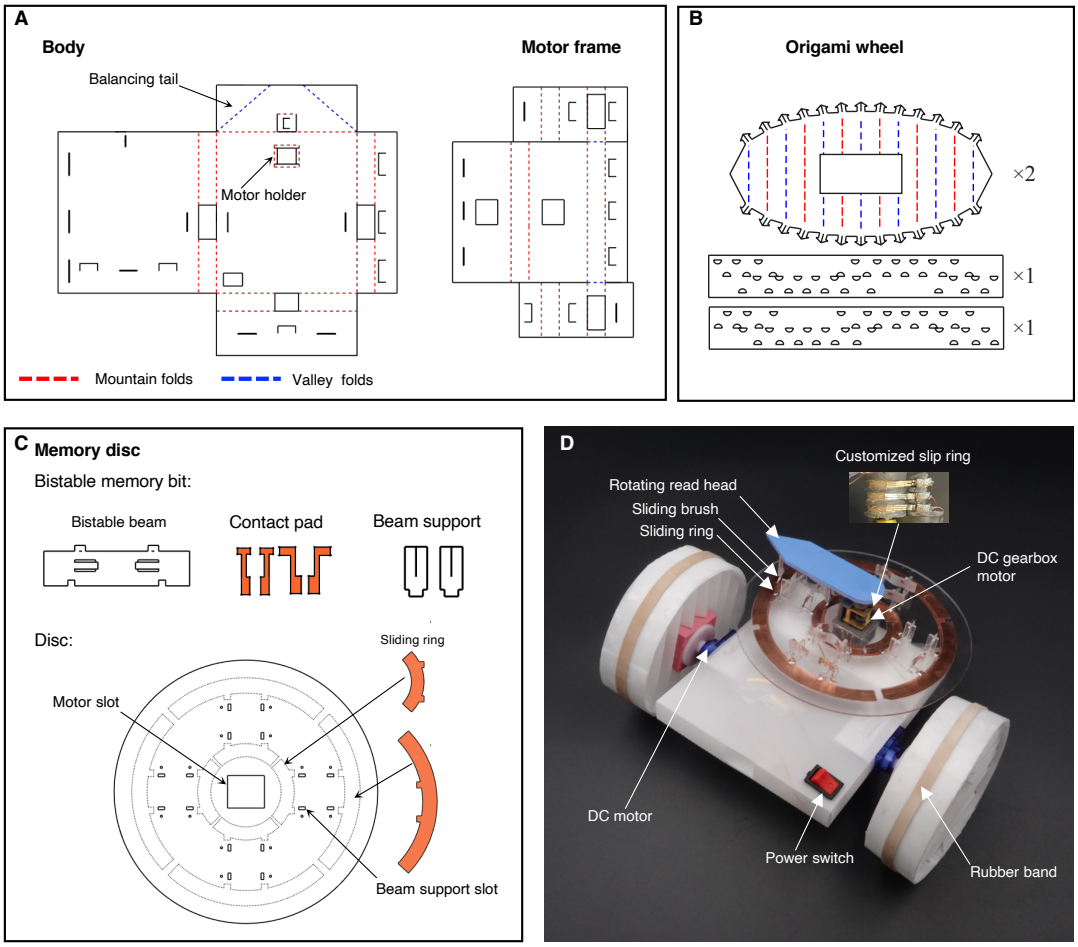

Figure 4.23: Design and assembly of the origami car with reprogrammable trajectories. 2D fabrication patterns of the origami body with motor frame (A) and origami corrugated wheel of the car (B). (C) Design of the memory disc. (D) The detailed structure of the car with labels.

4.5.2 Characterization of Components

4.5.2.1 Characterization of the CSCP actuator

There were two properties, thermal coefficient, c_T and stiffness k, of the CSCP actuator that needed to be characterized. The detailed parameters of the tested actuator sample

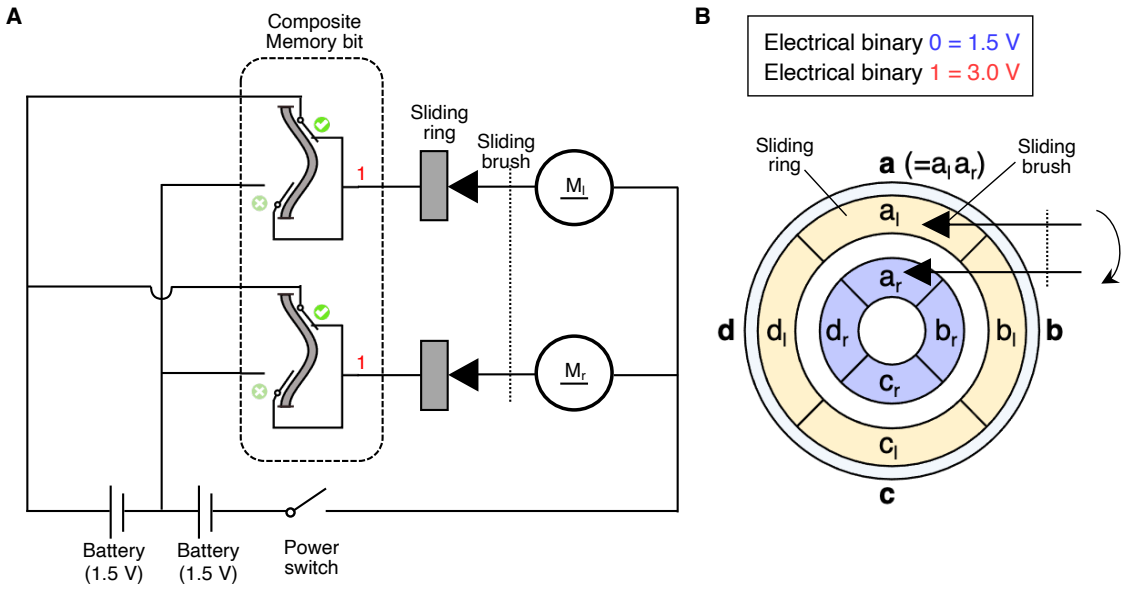

Figure 4.24: Circuit diagram of the origami wheeled car. (A) An example of the circuit of the car when the head reads a memory of 11. (B) The read head extracts information from (A) to (D) while rotating.

are listed in Table 4.1. To obtain c_T, we heated the actuator through Joule heating with a DC power supply (TP-3003D-3, Kaito Electronics, Inc.). When the actuator's temperature reached a steady state, the temperature and its corresponding generated force read from the Mechanical Test Systems (MultiTest, Mecmesin) were recorded. In the same manner, we changed the supply power, and thus temperature and recorded corresponding exerted force to plot the temperature-force curve, as shown in Fig.4.25A. By repeating the same test three times on two samples, we could fit the data with a linear curve. The curve's mean slope is the thermal coefficient, c_T, approximated as 2.18×10^{-2} N/°C [17].

k is determined through the slope of the force-displacement curve [17] produced by using the Mechanical Test Systems. A K-type thermal couple (CT-QB-K-0.1, PerfectPrime) and a thermometer (COMINHKPR146086, Leaton) were attached to the actuator using cyanoacrylate glue (Krazy glue, Elmer's Product, Inc.). The force-displacement curve has

a slope of around 0.39, which means the mean stiffness of the 50-mm-long actuator is 0.39 N/mm (Fig.4.25B).

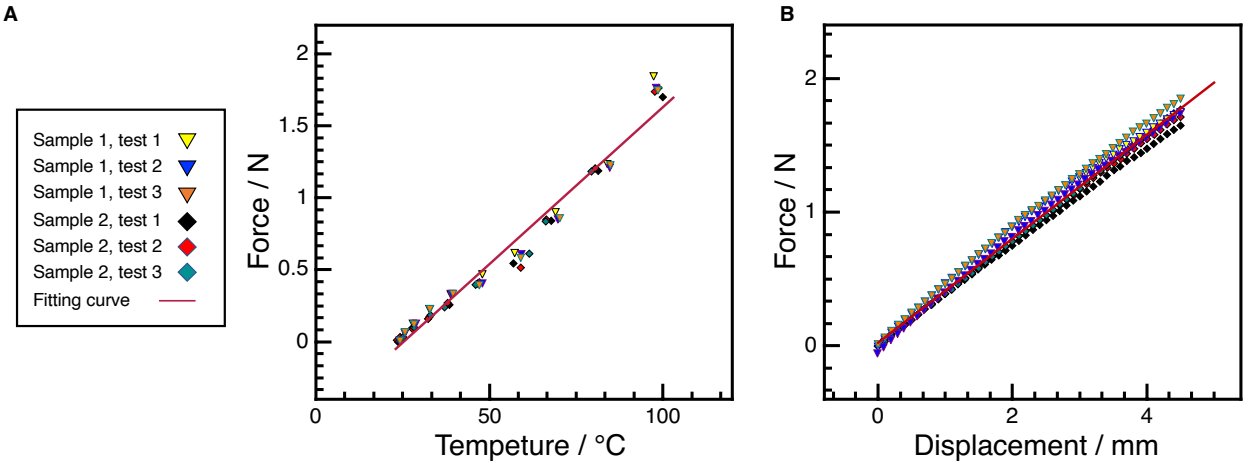

Figure 4.25: Characterization of the CSCP actuator. (A) The exerted force of the actuator as a function of its temperature when heated up through Joule heating. (B) The force-displacement curve of the actuator in room temperature.

4.5.2.2 Characterization of the Bistable Beam

The specific geometry parameters of the bistable beam testing samples are listed in Table 4.1. During the experiment, the Mechanical Test Systems (MultiTest, Mecmesin) can directly export the force-displacement curve of the bistable beam. We repeated the test three times and plot the force-displacement curve with a calculated standard deviation in light red color (see Fig.4.26). This curve indicates the values of the w_{rise}, w_{cr}, and F_{cr} are -2.12 mm, -0.83 mm, and 0.35 N. Note that the values of w_{rise}, w_{cr}, and F_{cr}, are converted to the coordinate system as shown in Fig.4.27A.

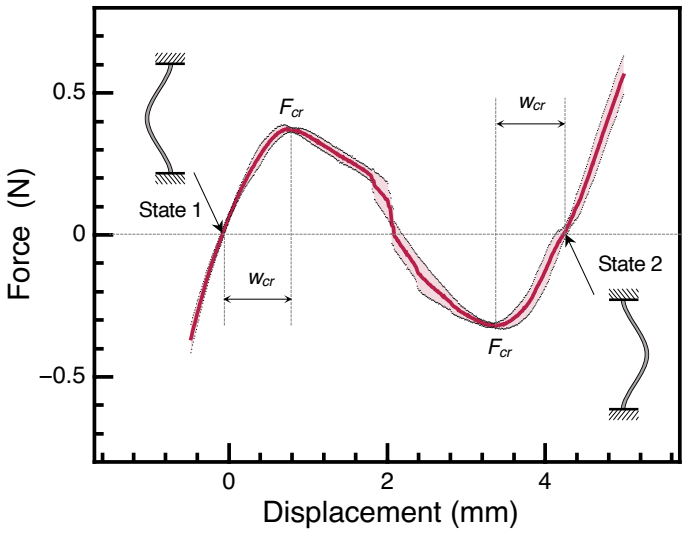

Figure 4.26: Characterization of the bistable beam. The force-displacement curve of the bistable beam.

4.5.3 Theory and Modeling of OMS

4.5.3.1 Analytical Modeling for the Gate Delay of the OMS

The schematic of the simplified OMS (actuator-bistable beam system) is the same as the oscillator as shown in Section3.2.1. Thus, expression of the actuation period, $T_{\text{actuation}}$ (=t_{snap}) can be written as follows:

$$T_{\text{actuation}} = -\frac{C_{\text{th}}}{\lambda} ln\{1 - \frac{\lambda R}{c_{\text{T}} U^2}[F_{\text{cr}} - k(w_{\text{cr}} - w_{\text{rise}})]\} \tag{4.1}$$

According to the definition of gate delay, this $\text{T}_{\text{actuation}}$ must be calculated when the opposite (reset) CSCP actuator is fully cooled down to ambient temperature. For Eq. 4.1 to be meaningful, we must force the value of the expression inside Logarithmic function to always remain positive, then we have Eq.4.2.

$$V_{supp} > \sqrt{\frac{\lambda R}{c_T}[F_{snap-thru} - k(w_{snap-thru} - w_{rise})]} \tag{4.2}$$

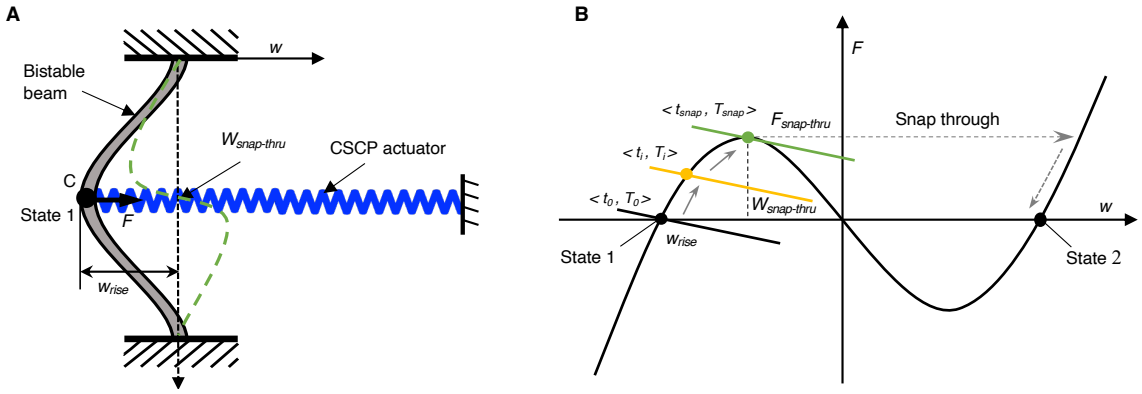

Figure 4.27: Schematic of the OMS. (A) A simplified model of OMS. The actuation force F from the actuator was applied to the centerpoint C of the bistable beam with an initial rise w_{rise}. The green dashed curve represents the transition mode (from state 1 to state 2) of the bistable beam. (B) The mechanism of the decoupled model of OMS. Black profile is the force-displacement curve of the bistable beam; straight lines represent the force-displacement curves of the CSCP actuator at different moments with their corresponding temperatures.

V_{supp} is the supplied electrical voltage across the actuator with a lower bound for snap-through defined by Eq. 4.2.

This expression serves to define the exclusive lower bound of the current necessary to cause the snap-through for a specific switch. Otherwise, the bistable bean will remain somewhere between w_{rise} and w_{cr} (see Fig.4.2 and Fig.4.27).

Thus, the gate delay can be expressed through the following:

$$T_{\text{delay}} = T_{\text{actuation}} + T_{\text{snap-thru}} \tag{4.3}$$

$T_{\text{snap-thru}}$ is the time period of the bistable beam as it transitions from a critical point snapping to another equilibrium state [148]. We characterized the $T_{\text{snap-thru}}$ of our bistable beam as about 0.11 s.

4.5.3.2 Scaling Analysis of the Gate Delay of OMS

As Eq.4.3 suggests, the lower bound of the gate delay is determined by both $T_{\text{actuation}}$ and $T_{\text{snap-thru}}$. $T_{\text{actuation}}$ is mainly attributed to actuators. To reduce $T_{\text{actuation}}$, we can increase actuation speed. For example, in our case, we can increase the supply power of the CSCP actuator as shown in Fig.4.3C. Otherwise, we can instead utilize intrinsically fast actuators, e.g., dielectric elastomer actuators. However, to obtain a smaller gate delay, it is necessary to speed up the snapping duration, which is mainly affected by the geometry and material properties of the bistable beam. According to [148], we can estimate the timescale of snapping by

$$T_* = \frac{{L_0}^2}{h}\sqrt{\frac{3\rho}{E}} \tag{4.4}$$

where L_0, h, ρ, and E are the length, thickness, density, and Young's modulus of the beam, respectively. This equation suggests that the most efficient method to reduce $T_{\text{snap-thru}}$ is to use a shorter beam; while increasing thickness, using lightweight or stiffer materials of the beam also help.

4.5.4 Comparing Two Different Control of the Flytrap-inspired Robots

To conduct a head-to-head comparison, we created a semiconductor-based traditional analog as shown in Fig. 4.21. The main difference from the origami-based robot is that we used common and easily accessible off-the-shelf semiconductor-based components for control, including a micro-controller (ESP8266), two capacitive touch sensors (TTP223B), and two linear motor modules. Each motor module consists of a servo motor (FS90R), a spool (made of a servo arm), and nylon string. When the motor is activated, it will rotate and drive the spool to contract the nylon string to close the leaves.

The detailed components, weight, and cost of these two robots are listed in Table 4.2. Here we consider the linear motor module as one component although it is composed of three sub-components. Therefore, our origami-based robot only shows a slight advantage over the

traditional one on the component count. This comparison result remains valid for most electrically/thermally driven actuators (e.g., SMA) that do not require additional associated components to close the leaves. It is worth noting that these actuators are usually more expensive and less accessible. For more general cases, we often need auxiliary components to convert the motion of actuators to achieve the closure of leaves. For example, when we use linear servo motors instead, specific transmission mechanisms or connectors are required, which increases the component number and thus the complexity.

Our origami-based robot has obvious advantages in terms of weight and cost. Specifically, the traditional robot weighs 2.5 times heavier than the origami one. The ratio could be even larger by replacing the 3D printed supports with lightweight origami counterparts. However, this advantage in weight could be mitigated when including heavy auxiliary components, e.g., batteries. As for cost comparison, we only calculate the total cost of off-the-shelf components. For example, the cost of a capacitive touch sensor is $ 0.84 (from Amazon) while that of an origami AND gate is about $ 0.34, estimated as the total cost of the required PET sheet and copper tape (from Amazon).

In addition, to compare the robustness, we operated these two robots under four different adversarial environmental events, i.e., static magnetic field, RF signal, electrostatic discharge (ESD), and mechanical deformation. (1) Static magnetic field. We used permanent magnet beads to introduce a magnetic field (0.47 T). On the traditional robot, the micro-controller and sensors were not affected by the magnetic field but the motors failed to respond. Upon removal, the traditional robot recovered its functionality. The origami-based one behaved as designed. (2) RF signal. The RF signal around the traditional robot triggered unexpected motor operation. This caused one of the leaves to close, which led to unsuccessful operation after the RF signal was removed. The origami-based counterpart remains intact. (3) ESD. A piezo igniter was adapted to generate high-voltage ESD, which damaged the micro-controller while having no impact on the origami AND gate. (4) Through bending and twisting, we applied mechanical strain rather than stress to the controllers, resulting in failure of the

micro-controller but not the origami one. It is worth noting that the pliers were electrically insulated to avoid causing a short circuit.

Table 4.2: Comparison between semiconductor- and origami-based control for the flytrap-inspired robot[1].

	Semiconductor-based	Origami-based
Component count [2]:	Total 9	Total 8
Sensing	Capacitive touch sensor (2)	Origami touch sensor (2)
Control	Microcontroller (1)	Origami AND gate (1)
Actuation	Linear motor module[3] (2)	CSCP actuator (2)
Structure	Leaf (2), support (1)	Leaf (2), support (1)
	Leaf holder (1)	
Weight (g):	Total 69.62	Total 28.03
Sensing	Capacitive touch sensor (1.91×2)	Origami touch sensor (0.34×2)
Control	Microcontroller (7.93×2)	Origami AND gate (1.91×2)
Actuation	Linear motor module (12.39×2)	CSCP actuator (0.07×2)
Structure	Leaf (3.13×2), support (17.13)	Leaf (3.13×2), support (17.13)
	Leaf holder (0.77)	
Cost ($) [4]:	Total 19.17	Total 1.48
Sensing	Capacitive touch sensor (0.84×2)	Origami touch sensor (0.08×2)
Control	Microcontroller (5.50)	Origami AND gate (0.32)
Actuation	Linear motor module (5.61×2),	CSCP actuator (0.12×2)
Structure	Leaf (0.02×2), support (0.72)	Leaf (0.02×2), support (0.72)
	Leaf holder (0.01)	
Robustness:		
Magnetic field (0.47 T)	✗	✓
RF signal (power, 5 W)	✗	✓
ESD ($V_{out} \geqslant$ 20kv)	✗	✓
Mechanical deformation	✗	✓

Note: 1. We do not include wiring and power supplies for a fair comparison. 2. We use component count to partially represent the complexity of the resulting robots. 3. Each motor module, counted as one component. 4. It is difficult to compare costs accurately. Here we only calculate the total cost of off-the-shelf components to represent the comparison.

Table 4.3: Taxonomy of autonomous origami and soft robots[1].

Robot	Sense-decide-act loop	Robustness				Easy to fabricate	Lightweight	Low cost[2]
		Magnetic filed	RF	ESD	Deformation			
Origami robots:								
Our robot	✓	✓	✓	✓	✓	✓	✓	✓
Ref. [149]	✓	✗	✗	✗	✗	✓	✓	✗
Millirobot [150]	✓	✓	✗	✗	✗	✗	✓	✓
Ref. [117]	✗	✓	✓	✓	✓	✓	✓	✓
Ref. [118]	✗	✓	✓	✓	✓	✓	✓	✓
Ref. [139]	✗	✓	✓	✓	✓	✗	✓	✗
Ref. [32]	✗	✗	✓	✓	✗	✗	✗	✗
Soft robots[3]:								
Ref. [54]	✗	✓	✓	✓	✓	✗	✗	✓
Trevor [10]	✗	✓	✓	✓	✗	✗	✓	✓
Ref. [119]	✓	✓	✓	✓	✓	✗	✗	✓
Ref. [120]	✓	✓	✓	✓	✓	✗	✗	✓
Ref. [122]	✗	✓	✓	✓	✓	✗	✓	✓
Octobot [8]	✗	✓	✓	✓	✓	✓	✓	✓
DEAnsect [81]	✓	✓	✗	✗	✓	✗	✓	✓

Note: 1. Here, we only list representative robots that can operate autonomously without requiring external control. These robots can either be powered by onboard supplies or tethered to off-board energy sources. 2. We only consider the cost of off-the-shelf materials. 3. Most remaining autonomous soft robots are composed of semiconductor-based micro-controllers and/or electromagnetic motors, which leads to low robustness against the listed adversarial environmental events and presumably loses their advantages in weight and cost.

4.6 Conclusion and Discussion

This work proposes an integrated process for creating autonomous robots with sensing, control, and actuation directly embedded into compliant origami materials and structures. This method is enabled by our origami multiplexed switch (OMS) that functions as a multiplexer by harnessing a snap-through instability to control electrical signals. The unique design endows OMS with multiple functions. (i) The OMS can be used as a relay and functions robustly to noise, which are validated through experimental demonstrations. (ii) The OMS can also be reconfigured into origami logic gates (including NOT, AND, and OR, with functional completeness). (iii) We have further shown that it is practical to compose multiple OMSs in a cascading manner by using NAND and NOR gates as examples. This successful composition suggests that the design space of our origami computing architectures is far larger than those presented in this paper. (iv) In addition, to demonstrate the potential of the OMS for origami robots, we built a 1-bit storage device (i.e., Set-Reset latch) from an OMS that can write, erase, rewrite itself, and sustain power outage, which would be necessary for achieving a higher-level autonomy of robots. (v) To achieve interaction with environments, we further proposed origami sensors and thus constructed a complete sense-decide-act loop. So far, we have also demonstrated that it is practical to create autonomous robots by integrating simple sensing, control, and actuation directly into compliant origami structures based on the OMS. These demonstrate a solid step towards untethered, autonomous origami robots and intelligent matter purely through cut-and-fold.

Our OMS and logic gates use electrical signals as both inputs and outputs; this architecture makes it possible to use the output to control any electrically or thermally driven actuators (e.g., shape memory alloy actuators [105, 114, 151], conductive liquid crystal elastomers (LCE) [134], etc.), making them suitable for integrating into a wide range of robots and machines. The system can function equally well under AC signals; though not demonstrated, the core OMS is driven by the current magnitude and is thus independent of its

direction of flow. For example, an output AC signal can be directly used to drive an electromagnetic actuator [152] from a comparable supply. For pure mechanical logic networks, the number of inputs that an output signal can drive (i.e., fan-out) is often very small, which is restricted by the limited number of accessible interactions between gates, high damping, and other losses [58]. Our proposed architecture combined with the nature of low resistance of logic gates vastly enlarges the fan-out, which could potentially increase the overall scope of the resulting computing networks and thus the design space of our proposed system.

Our OMS-based mechanism provides opportunities for adopting other actuation systems, which could lead to broader applications. As stated above, we use the same type of signal for both the inputs and outputs of OMS-based devices. The output signals from previous gates can be directly fed as the inputs of the downstream gates without additional interfacing components. Thus, we have two main requirements for actuators in our system. 1) They can be directly activated by signals of interest. For instance, CSCP actuators can be electrically driven. 2) Actuators are capable of exerting sufficient displacement and force to toggle the bistable mechanism. Taking shape memory alloy (SMA) actuators as an example, they can be electrically activated and generate large linear contractions, which makes them suitable for our systems. Actuators, like ionic polymer-metal composites, might not be competent due to their small output force. Other electrically driven actuators, e.g., conductive LCEs are also viable. Another common actuation of interest is pneumatic (or fluidic). For instance, linear contracting pneumatic actuators can be used to activate the bistable beam [153]. Accordingly, we need to use pneumatic current as a signal instead of electricity [120]. Otherwise, we could build hybrid origami logic systems for specific applications that require different input and output signals, although additional interfacing components are required for cascaded circuits. For example, we can create origami logic with pneumatic inputs but electrical outputs similar to Ref. [119]. Alternative actuators, e.g., light-driven LCEs, may be adopted into our system to build more hybrid origami logic and autonomous machines.

The proposed devices have been tested to robustly function for the order of hundreds of repetitions, which is sufficient for all of the demonstrations in this paper. Based on our previous work [117] that conducted a lifecycle test on a self-sustained oscillator that shares the same materials and physical processes, these devices could presumably work at least thousands of times with marginal degradation in performance; failure largely happened because of the thermal instability of CSCP actuators under cyclic heating/cooling. Extending the durability of origami devices is out of the scope of this paper; the feasibility of long-time operation still needs to be validated experimentally for further exploration. Alternately, this issue can be addressed by replacing the CSCP actuators with known long-life mechanisms, e.g., dielectric elastomer actuators (DEA), although that requires a high working voltage [81].

Constructing logic gates and robots with bistable beams enables easy memory and state storage, which allows energy saving since only switching between states requires power [154]. Although it is favorable for information storage, this bistability-based architecture requires a reset after each computational execution. Instead, using monostable beams with snap-through (the beams will snap back to their stable position if the applied force is removed) can enable self-reset at the cost of constant operating power. The self-reset allows continuous operation and thus less external interference for simple circuits [120]. However, the fabrication of a monostable beam using folding-based methods is much more challenging due to the high sensitivity to its geometry parameters and boundary conditions [155]. Therefore, the trade-off between two different architectures needs to be considered for specific tasks.

The delay of a single OMS-based gate is essentially determined by the time needed for the contraction of the CSCP actuator and the snap-through of the bistable beam. Presumably, we could largely shorten the response time of the actuator by increasing the supply voltage while increasing the snap-through speed by adopting a shorter, stiffer, or lightweight beam, or increasing the thickness of the beam (more discussion can be found in Section4.5.3). However, it is very challenging to further reduce the delay to be comparable with that of semiconductor-based devices, which is also not the goal of this work. Therefore, our OMS-

based devices are mainly suitable for speed-insensitive applications. Moreover, our origami-based process provides alternative approaches to generate more complicated circuits. For instance, a self-sustained oscillator can be directly created instead of combining several OMS-based gates [117]. Other more complex functionalities could presumably be built in a similar manner.

Although our origami components and devices, such as logic gates, are less performant than conventional semiconductor counterparts in terms of speed, density, and energy efficiency, our OMS information processing architecture demonstrates advantages for certain applications without a power constraint. For example, the OMS, sensors, logic gates, and origami robots are built of non-rigid, inexpensive sheet materials (polyester) and conductive sewing threads through origami-inspired folding. This approach allows integrated design and rapid fabrication for accessible, low cost, and potentially disposable designs [107]. The resulting integrated systems are semiconductor-free, and nonmagnetic, enabling practical applications in extreme environments (e.g., with high magnetic or radiation fields).

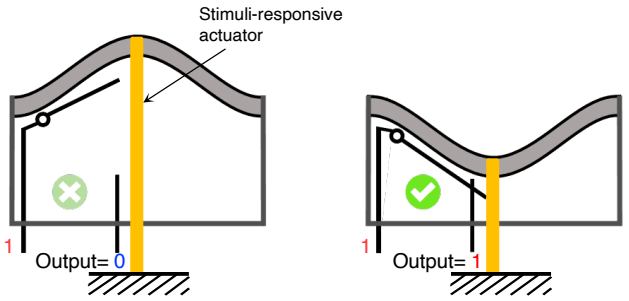

Figure 4.28: Schematic of sensors for other stimuli. The stimuli-responsive actuators can activate the bistable beam to change the on/off state of the circuit upon perceiving corresponding signals. Thus, various stimuli could be detected and converted to electrical signals to interface with our control units.

Sensors that perceive different signals allow a broader range of interactions with humans and the environment. Our current robots can only detect touch (or collision), which could largely limit their functionalities. One way they can be constructed is by replacing the CSCP

actuators on the bistable (or monostable) beam of OMS with stimuli-responsive materials (see Fig.4.28); thus the corresponding stimuli can be transduced into an output voltage signal. For example, the OMS can be modified as an optical sensor by substituting the CSCP actuators with photo-responsive liquid crystal elastomers [134].

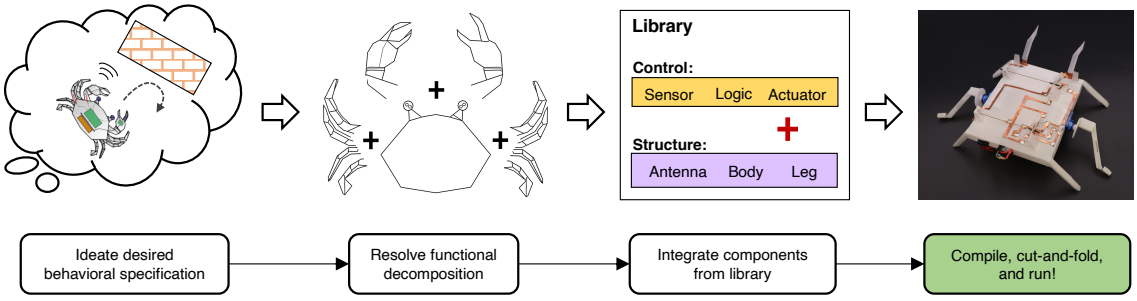

Figure 4.29: Conceptual workflow to create a functional robot/system using our monolithic paradigm. The capabilities of our manufacturing process could enable a possible computational design pipeline to take as input a schematic outlining a high-level breakdown of the required components and output manufacturable drawings ready for fabrication and assembly. Currently, our system relies on experts to decompose functionalities, combine components from the library, and generate manufacturable drawings for assembly. Further development on automated tools could enable on-demand design for non-expert users: with our existing available components (sensors, switches, logic, controllers, and actuators) as building blocks, users could compose their targeted functionalities and realize the creation of desired robotic devices through folding from functional sheet and thread materials.

Meanwhile, our folding-based compliant devices and robots are easier to build and integrate with compared with soft-bodied polymer counterparts, which typically involve multi-stage molding (or printing) and sealing processes [8, 119, 120]. The folding-based method for creating robots is engaging and unintimidating, making it desired for applications in the toy industry and education [107]. The low cost of constituent materials and simple equipment requirements further make our method more accessible for resource-constrained students.

Currently, we have realized up to two levels of cascaded combinational logic; our modularized design of fundamental gates (NOT, AND, and OR) allows us to compose arbitrarily complex gates through further cascading using geometric layout and wiring. However, to broaden the scope of our origami digital logic for autonomous robots, this universal functionality must be augmented by three additional research contributions: i) Fabrication. Although our current folding-based process makes it easy to prototype single units, it is limited for high-throughput creation. Solutions for at-scale manufacturing of origami structures include automating self-folding [32] through careful materials selection [156]. ii) Sizing. We have currently designed centimeter-scale devices. Though a nominal decrease in size might be possible through further engineering optimization, a several-fold reduction in characteristic dimension—on par with other scaled 2D printable techniques such as pop-up book MEMS [157] or direct printing of actuators [158]—would practically enable much more complex logic. iii) Design automation. With the increasing number of logic gates in more complicated circuits, the design and implementation of desired functionalities become onerous; this could also result in inefficiencies due to unoptimized circuits and their wiring. Computational design tools (e.g., [159, 160]) have been used to assist in the generation of desired devices in a rapid manner. Similarly, the creation of our proposed origami robots could be achieved efficiently through an automated workflow as shown in Fig.4.29.

CHAPTER 5

Conclusion

This thesis demonstrates a printable design and fabrication paradigm to create autonomous robots with sensing, control, and actuation fully embedded into compliant materials using idea inspired by origami cut-and-fold (see Fig. 1.1). This paradigm could lead to a new class of origami robots, with levels of autonomy approaching their semiconductor-based analogs, while maintaining the desired attributes (e.g., lightweight and low-cost) associated with the folding-based design and fabrication method. In addition, I have devised key components to realize autonomous behaviors, including self-sustained oscillations, information perception and processing, logic and computing, and human/environment-robot interactions. I have also derived tractable analytical models for proposed components to characterize critical behaviors; these models could then be developed into design tools to enable rapid prototyping of desired electromechanical components from functional specifications. Through the exploration of this thesis, the detailed design space of the proposed method can be summarized in Table 5.1.

Further integration with printable power supplies could give rise to the construction of untethered, autonomous origami machines. Current devices and robots rely heavily on off-board power or bulky Lithium batteries, which could limit their mobility and operation lifetime. To create untethered autonomous robots entirely through origami cut-and-fold, we can incorporate thin film lithium batteries by embedding them into origami structures [35, 36, 161]. These batteries can provide both load-bearing and energy storage and can be easily built through 2D fabrication without post-installation. Alternative power sources

could also be possible. For example, energy harvesters that can be adapted along with regulation systems to power resulting robots.

In this thesis, I have achieved autonomous locomotion and interaction separately. To move towards a higher level of autonomy, these two functionalities should be combined. A quick way to do this is to replace the DC motors of the self-reversing crawler (see Section 4.4.2) with origami oscillators [117] to generate periodic motions. This would lead to advances in developing untethered, intelligent systems purely through origami-inspired cut-and-fold.

Additional capabilities such as clocking logic can be created within our proposed origami paradigm to improve the autonomy of origami robotics. We can create a clock by using origami oscillators that generate alternating signals from a constant voltage supply as presented in our previous work [90]. Integrating this clock enables sequential logic and higher autonomy for origami machines.

Our work lays the groundwork for future research aimed at creating autonomous robots purely through folding without post-installation. Currently, parts of components (e.g., actuators) still need to be installed after folding processes. Therefore, it is vital to develop versatile 2D composites that tightly integrate the necessary functional materials to complete essential functionalities, including sensing, computing, and actuation. Pop-up book MEMS [162] is a promising method to embed necessary functionalities into patterned laminates that can be folded to construct autonomous machines. Another encouraging direction is 3D printing, especially multimaterial direct-ink-writing and embedded 3D printing. Thus, multifunctional 2D precursors can be directly created either through lamination or printing and then folded into preprogrammed configurations with desired functionalities without post-installation.

In summary, our proposed method provides an alternative way to create autonomous origami robots by tightly integrating smart materials to achieve a wide range of functionalities. Our method has demonstrated the great potential to use origami functional materials

and mechanisms to further advance the autonomy of robotics (e.g., realizing a finite state machine or even a Turing machine) at the same time preserving advantageous features inherent in origami-based fabrication. These origami robots—built of non-rigid, inexpensive sheet and thread materials—allow for accessible, low cost, and potentially disposable designs [107]. The resulting integrated systems are also semiconductor-free and nonmagnetic, enabling practical applications in challenging environments (e.g., with high magnetic or radiation fields).

Table 5.1: Design space of our proposed method.

Components	Implementation	Challenges
Computation :		
Single logic gates (NOT, OR, AND)	✓ (Fig.4.4A, C)	
Cascaded logic gates (NOR, NAND)	✓ (Fig.4.4D)	
Clock	✓ (Fig.2.1A)	
Complex combinational logic	✣	Fabrication
Sequential logic	✣	Fabrication; Integration with registers
Sensing :		
Sensor (touch)	✓ (Fig.4.7A, 4.6D)	
Sensor (vision)	✗	No available transducers
Sensor (other stimuli)	✣ (Fig.4.28)	Need stimuli-responsive materials
Actuation :		
Actuator (electrical/thermal driven)	✓ (Fig.4.4B, 4.7B)	
Actuator (other stimuli)	✣	Require functional materials
Actuator (linear)	✓ (Fig.4.4B, E)	
Actuator (small-angle rotating)	✓ (Fig.4.6E)	
Actuator (continuous rotating)	✗	No available rotating mechanism
Actuator (Oscillatory)	✓ (Fig.2.1A)	
Memory :		
S-R latch	✓ (Fig.4.5A)	
Multi-bit nonvolatile memory	✓ (Fig.4.8B)	
Addressable memory bank	✣	Fabrication, Require indexing mechanisms
Power :		
Battery	✣ (Ref [35, 161])	Fabrication, Need suitable electrochemical materials

Note: ✣ represents that the component has not been built but is possible based on our proposed method.

REFERENCES

[1] Jakob A. Faber, Andres F. Arrieta, and André R. Studart. Bioinspired spring origami. *Science*, 359:1386–1391, 2018.

[2] Hidetoshi Kobayashi, Biruta Kresling, and Julian FV Vincent. The geometry of unfolding tree leaves. *Proceedings of the Royal Society of London. Series B: Biological Sciences*, 265(1391):147–154, 1998.

[3] Anne Waugh and Allison Grant. *Ross and Wilson anatomy & physiology in health and illness*. 2014.

[4] C. D. Onal, R. J. Wood, and D. Rus. An origami-inspired approach to worm robots. *IEEE/ASME Transactions on Mechatronics*, 18(2):430–438, 2013.

[5] S. Felton, M. Tolley, E. Demaine, D. Rus, and R. Wood. A method for building self-folding machines. *Science*, 345(6197):644–646, 2014.

[6] E. Hawkes, B. An, N. M. Benbernou, H. Tanaka, S. Kim, E. D. Demaine, D. Rus, and R. J. Wood. Programmable matter by folding. *Proc. Natl. Acad. Sci. U.S.A.*, 107(28):12441–12445, 2010.

[7] Philipp Rothemund, Alar Ainla, Lee Belding, Daniel J. Preston, Sarah Kurihara, Zhigang Suo, and George M. Whitesides. A soft, bistable valve for autonomous control of soft actuators. *Science Robotics*, 3:eaar7986, March 2018.

[8] Michael Wehner, Ryan L. Truby, Daniel J. Fitzgerald, Bobak Mosadegh, George M. Whitesides, Jennifer A. Lewis, and Robert J. Wood. An integrated design and fabrication strategy for entirely soft, autonomous robots. *Nature*, 536:451–455, 2016.

[9] Yuanping Song, Robert M. Panas, Samira Chizari, Lucas A. Shaw, Julie A. Jackson, Jonathan B. Hopkins, and Andrew J. Pascall. Additively manufacturable micromechanical logic gates. *Nature Communications*, 10(1):882, February 2019.

[10] E.-F. Markus Henke, Samuel Schlatter, and Iain A. Anderson. Soft dielectric elastomer oscillators driving bioinspired robots. *Soft Robot.*, 4:353–366, 2017.

[11] M. Garrad, G. Soter, A. T. Conn, H. Hauser, and J. Rossiter. A soft matter computer for soft robots. *Science Robotics*, 4(33):eaaw6060, August 2019.

[12] Mattias Vangbo and Ylva Bäcklund. A lateral symmetrically bistable buckled beam. *Journal of Micromechanics and Microengineering*, 8(1):29, 1998.

[13] Tian Chen, Osama R. Bilal, Kristina Shea, and Chiara Daraio. Harnessing bistability for directional propulsion of soft, untethered robots. *Proceedings of the National Academy of Sciences*, 115(22):5698–5702, May 2018.

[14] Benjamin Treml, Andrew Gillman, Philip Buskohl, and Richard Vaia. Origami mechanologic. *Proceedings of the National Academy of Sciences*, 115(27):6916–6921, 2018.

[15] Jordan R. Raney, Neel Nadkarni, Chiara Daraio, Dennis M. Kochmann, Jennifer A. Lewis, and Katia Bertoldi. Stable propagation of mechanical signals in soft media using stored elastic energy. *Proceedings of the National Academy of Sciences*, 113(35):9722–9727, 2016.

[16] C. K. Harnett. Flexible circuits with integrated switches for robotic shape sensing. In *Sensors for Next-Generation Robotics III*, volume 9859, page 98590I. International Society for Optics and Photonics, May 2016.

[17] Michael C. Yip and Gunter Niemeyer. On the control and properties of supercoiled polymer artificial muscles. *IEEE Transactions on Robotics*, 33(3):689–699, June 2017.

[18] Subramanian Sundaram, Petr Kellnhofer, Yunzhu Li, Jun-Yan Zhu, Antonio Torralba, and Wojciech Matusik. Learning the signatures of the human grasp using a scalable tactile glove. *Nature*, 569(7758):698–702, May 2019.

[19] Daniela Rus and Michael T. Tolley. Design, fabrication and control of origami robots. *Nat. Rev. Mater.*, 3:101–112, 2018.

[20] Alexander Pagano, Tongxi Yan, Brian Chien, A. Wissa, and S. Tawfick. A crawling robot driven by multi-stable origami. *Smart Mater. Struct.*, 26:094007, 2017.

[21] S. Miyashita, S. Guitron, M. Ludersdorfer, C. R. Sung, and D. Rus. An untethered miniature origami robot that self-folds, walks, swims, and degrades. In *2015 IEEE International Conference on Robotics and Automation*, pages 1490–1496, 2015.

[22] Dae-Young Lee, Sa-Reum Kim, Ji-Suk Kim, Jae-Jun Park, and Kyu-Jin Cho. Origami wheel transformer: A variable-diameter wheel drive robot using an origami structure. *Soft Robot.*, 4:163–180, 2017.

[23] B. Shin, S. M. Felton, M. T. Tolley, and R. J. Wood. Self-assembling sensors for printable machines. In *2014 IEEE International Conference on Robotics and Automation*, pages 4417–4422, May 2014.

[24] Yash Mulgaonkar, Brandon Araki, Je Sung Koh, Luis Guerrero-Bonilla, Daniel Aukes, Anurag Makineni, Michael T. Tolley, Daniela Rus, Robert J. Wood, and Vijay Kumar. The flying monkey: A mesoscale robot that can run, fly, and grasp. In *2016 IEEE International Conference on Robotics and Automation*, pages 4672–4679, June 2016.

[25] Yufeng Chen, Hongqiang Wang, E. Farrell Helbling, Noah T. Jafferis, Raphael Zufferey, Aaron Ong, Kevin Ma, Nicholas Gravish, Pakpong Chirarattananon, Mirko Kovac, and Robert J. Wood. A biologically inspired, flapping-wing, hybrid aerial-aquatic microrobot. *Sci. Robot.*, 2(11), October 2017.

[26] Jizhai Cui, Tian-Yun Huang, Zhaochu Luo, Paolo Testa, Hongri Gu, Xiang-Zhong Chen, Bradley J. Nelson, and Laura J. Heyderman. Nanomagnetic encoding of shape-morphing micromachines. *Nature*, 575(7781):164–168, November 2019.

[27] Ziyu Ren, Wenqi Hu, Xiaoguang Dong, and Metin Sitti. Multi-functional soft-bodied jellyfish-like swimming. *Nature Communications*, 10(1):1–12, July 2019.

[28] C. D. Onal, R. J. Wood, and D. Rus. An origami-inspired approach to worm robots. *IEEE/ASME Transactions on Mechatronics*, 18:430–438, 2013.

[29] A. M. Mehta, J. DelPreto, B. Shaya, and D. Rus. Cogeneration of mechanical, electrical, and software designs for printable robots from structural specifications. In *2014 IEEE/RSJ International Conference on Intelligent Robots and Systems*, pages 2892–2897, 2014.

[30] Suk-Jun Kim, Dae-Young Lee, Gwang-Pil Jung, and Kyu-Jin Cho. An origami-inspired, self-locking robotic arm that can be folded flat. *Sci. Robot.*, 3:eaar2915, 2018.

[31] Johannes T. B. Overvelde, James C. Weaver, Chuck Hoberman, and Katia Bertoldi. Rational design of reconfigurable prismatic architected materials. *Nature*, 541(7637):347–352, January 2017.

[32] S. Felton, M. Tolley, E. Demaine, D. Rus, and R. Wood. A method for building self-folding machines. *Science*, 345(6197):644–646, 2014.

[33] Tianqi Xu, Jiachen Zhang, Mohammad Salehizadeh, Onaizah Onaizah, and Eric Diller. Millimeter-scale flexible robots with programmable three-dimensional magnetization and motions. *Sci. Robot.*, 4:eaav4494, 2019.

[34] Paul W. K. Rothemund. Folding dna to create nanoscale shapes and patterns. *Nature*, 440:297–302, 2006.

[35] Mingqiang Wang, Drew Vecchio, Chunyan Wang, Ahmet Emre, Xiongye Xiao, Zaixing Jiang, Paul Bogdan, Yudong Huang, and Nicholas A Kotov. Biomorphic structural batteries for robotics. *Sci. Robot.*, 5(45):eaba1912, 2020.

[36] Zeming Song, Teng Ma, Rui Tang, Qian Cheng, Xu Wang, Deepakshyam Krishnaraju, Rahul Panat, Candace K Chan, Hongyu Yu, and Hanqing Jiang. Origami lithium-ion batteries. *Nat. Commun.*, 5(1):1–6, 2014.

[37] Pengcheng Cao, James Strawson, Xuebin Zhu, Everbrook Zhou, Chase Lazar, Dominique Meyer, Zhaoliang Zheng, Thomas Bewley, and Falko Kuester. Beaglerover: An open-source 3d-printable robotic platform for engineering education and research. In *AIAA SCITECH 2022 Forum*, page 1914, 2022.

[38] David L Nelson and Michael M Cox. *Lehninger Principles of Biochemistry, Fourth Edition*. Fourth edition edition, 2004.

[39] Irene Luque, Stephanie A. Leavitt, and Ernesto Freire. The linkage between protein folding and functional cooperativity: Two sides of the same coin? *Annual Review of Biophysics and Biomolecular Structure*, 31(1):235–256, 2002.

[40] Paul D Boyer and Edwin G Krebs. *The enzymes*. Academic Press, 1986.

[41] F Haas, S Gorb, and RJ Wootton. Elastic joints in dermapteran hind wings: materials and wing folding. *Arthropod Structure & Development*, 29(2):137–146, 2000.

[42] Henry Gray. *Anatomy of the human body*. Lea & Febiger, 1924.

[43] Erik D Demaine, Martin L Demaine, and Joseph SB Mitchell. Folding flat silhouettes and wrapping polyhedral packages: New results in computational origami. *Computational Geometry*, 16(1):3–21, 2000.

[44] Tomohiro Tachi. Origamizing polyhedral surfaces. *IEEE transactions on visualization and computer graphics*, 16(2):298–311, 2009.

[45] Erik D Demaine and Tomohiro Tachi. Origamizer: A practical algorithm for folding any polyhedron. In *33rd International Symposium on Computational Geometry (SoCG 2017)*. Schloss Dagstuhl-Leibniz-Zentrum fuer Informatik, 2017.

[46] Anwesha Chattoraj, Eric Vin, Yusuke Tanaka, Jillian Naldrien Pantig, Daniel J Fremont, and Ankur Mehta. Tackling simulation inconsistencies in the robot design process by selective empirical evaluation. In *Proceedings of Cyber-Physical Systems and Internet of Things Week 2023*, pages 105–113. 2023.

[47] Noy Bassik, George M. Stern, and David H. Gracias. Microassembly based on hands free origami with bidirectional curvature. *Applied Physics Letters*, 95(9):91901, August 2009.

[48] H. Okuzaki, T. Saido, H. Suzuki, Y. Hara, and H. Yan. A biomorphic origami actuator fabricated by folding a conducting paper. *Journal of Physics: Conference Series*, 127:012001, August 2008.

[49] Chang Liu, Wenzhong Yan, Pehuen Moure, Cody Fan, and Ankur Mehta. A computational design and evaluation tool for 3d structures with planar surfaces. *arXiv preprint arXiv:2103.02114*, 2021.

[50] Wenzhong Yan, Dawei Zhao, and Ankur Mehta. Fabrication-aware design for furniture with planar pieces. *Robotica*, 41(1):48–73, 2023.

[51] Jan Zavodnik, Yunbo Wang, Wenzhong Yan, Miha Brojan, and M Khalid Jawed. Soft kirigami composites for form-finding of fully flexible deployables. *arXiv preprint arXiv:2301.06597*, 2023.

[52] C. D. Onal, M. T. Tolley, R. J. Wood, and D. Rus. Origami-inspired printed robots. *IEEE/ASME Transactions on Mechatronics*, 20(5):2214–2221, 2015.

[53] Bobak Mosadegh, Chuan-Hsien Kuo, Yi-Chung Tung, Yu-suke Torisawa, Tommaso Bersano-Begey, Hossein Tavana, and Shuichi Takayama. Integrated elastomeric components for autonomous regulation of sequential and oscillatory flow switching in microfluidic devices. *Nat. Phys.*, 6:433–437, 2010.

[54] Daniel J. Preston, Haihui Joy Jiang, Vanessa Sanchez, Philipp Rothemund, Jeff Rawson, Markus P. Nemitz, Won-Kyu Lee, Zhigang Suo, Conor J. Walsh, and George M. Whitesides. A soft ring oscillator. *Sci. Robot.*, 4:eaaw5496, 2019.

[55] Xi Chen, Davis Goodnight, Zhenghan Gao, Ahmet H. Cavusoglu, Nina Sabharwal, Michael DeLay, Adam Driks, and Ozgur Sahin. Scaling up nanoscale water-driven energy conversion into evaporation-driven engines and generators. *Nat. Commun.*, 6:7346, 2015.

[56] Xiao-Qiao Wang, Chuan Fu Tan, Kwok Hoe Chan, Xin Lu, Liangliang Zhu, Sang-Woo Kim, and Ghim Wei Ho. In-built thermo-mechanical cooperative feedback mechanism for self-propelled multimodal locomotion and electricity generation. *Nat. Commun.*, 9:3438, 2018.

[57] Yusen Zhao, Chen Xuan, Xiaoshi Qian, Yousif Alsaid, Mutian Hua, Lihua Jin, and Ximin He. Soft phototactic swimmer based on self-sustained hydrogel oscillator. *Sci. Robot.*, 4:eaax7112, 2019.

[58] Hiromi Yasuda, Philip R. Buskohl, Andrew Gillman, Todd D. Murphey, Susan Stepney, Richard A. Vaia, and Jordan R. Raney. Mechanical computing. *Nature*, 598:39–48, 2021.

[59] Chun-Yin Tsai, Wei-Ting Kuo, Chi-Bao Lin, and Tsung-Lin Chen. Design and fabrication of MEMS logic gates. *Journal of Micromechanics and Microengineering*, 18(4):045001, feb 2008.

[60] Pallavi Singh, Devendra Kr. Tripathi, Shikha Jaiswal, and H. K. Dixit. All-Optical Logic Gates: Designs, Classification, and Comparison. *Advances in Optical Technologies*, 2014:275083, March 2014.

[61] S. Lee and H. Chang. Magnetic bubble logic. *IEEE Transactions on Magnetics*, 10(4):1059–1066, December 1974.

[62] Daniel J. Preston, Philipp Rothemund, Haihui Joy Jiang, Markus P. Nemitz, Jeff Rawson, Zhigang Suo, and George M. Whitesides. Digital logic for soft devices. *Proceedings of the National Academy of Sciences*, page 201820672, March 2019.

[63] Wenzhong Yan, Shuguang Li, Mauricio Deguchi, Zhaoliang Zheng, Daniela Rus, and Ankur Mehta. Origami-based integration of robots that sense, decide, and respond. *Nature Communications*, 14(1):1553, 2023.

[64] Jack Thiesen Dan J. Clingman. The development of two broadband vibration energy harvesters (BVEH) with adaptive conversion electronics. *Proc.SPIE*, 10166:10166 – 10166 – 19, 2017.

[65] Adrienne Crivaro, Robert Sheridan, Mary Frecker, Timothy W Simpson, and Paris Von Lockette. Bistable compliant mechanism using magneto active elastomer actuation. *Journal of Intelligent Material Systems and Structures*, 27(15):2049–2061, 2016.

[66] Mrunmayi Mungekar, Leixin Ma, Wenzhong Yan, Vishal Kackar, Shyan Shokrzadeh, and Mohammad Khalid Jawed. Design of bistable soft deployable structures via a kirigami-inspired planar fabrication approach. *Advanced Materials Technologies*, page 2300088, 2023.

[67] Tian Chen, Jochen Mueller, and Kristina Shea. Integrated design and simulation of tunable, multi-state structures fabricated monolithically with multi-material 3d printing. *Scientific Reports*, 7:45671, mar 2017.

[68] Sicong Shan, Sung H. Kang, Jordan R. Raney, Pai Wang, Lichen Fang, Francisco Candido, Jennifer A. Lewis, and Katia Bertoldi. Multistable Architected Materials for Trapping Elastic Strain Energy. *Advanced Materials*, 27:4296–4301, 2015.

[69] Konstantin Shaposhnikov, Dayi Zhang, Wenzhong Yan, and Jie Hong. Investigation on the dynamic characteristics of a rotor suffering impact foundation external excitation. In *Proceedings of the 10th International Conference on Rotor Dynamics – IFToMM*, pages 442–459. Springer International Publishing, 2019.

[70] Wenzhong Yan, Konstantin Shaposhnikov, Pingchao Yu, Yanhong Ma, and Jie Hong. Experimental Investigation and Numerical Analysis on Influence of Foundation Excitation on the Dynamics of the Rotor System, 2015.

[71] Yanhong Ma, Zhichao Liang, Dayi Zhang, Wenzhong Yan, and Jie Hong. Experimental Investigation on Dynamical Response of an Overhung Rotor due to Sudden Unbalance, 2015.

[72] Ali Maziz, Alessandro Concas, Alexandre Khaldi, Jonas Stålhand, Nils-Krister Persson, and Edwin W. H. Jager. Knitting and weaving artificial muscles. *Science Advances*, 3(1):e1600327, January 2017.

[73] Emily Marie Lovell. A Soft Circuit Curriculum to Promote Technological Self-Efficacy.

[74] Daisong Zhang and Yahya Rahmat-Samii. Integration of electro-textile RF coil array with magnetic resonance imaging (MRI) system: Design strategies and characterization methods. In *2018 International Workshop on Antenna Technology (iWAT)*, pages 1–3, March 2018.

[75] Michael C. Yip and Gunter Niemeyer. High-performance robotic muscles from conductive nylon sewing thread. In *2015 IEEE International Conference on Robotics and Automation*, pages 2313–2318, Seattle, WA, USA, 2015.

[76] Artificial Muscles from Fishing Line and Sewing Thread. *Science*, 343(6173):868–872, February 2014.

[77] Paul Horowitz. *The art of electronics*. Cambridge University Press, New York, NY, third edition edition, 2015.

[78] Owies M. Wani, Hao Zeng, and Arri Priimagi. A light-driven artificial flytrap. *Nat. Commun.*, 8:15546, May 2017.

[79] Richard Baumgartner, Alexander Kogler, Josef M Stadlbauer, Choon Chiang Foo, Rainer Kaltseis, Melanie Baumgartner, Guoyong Mao, Christoph Keplinger, Soo Jin Adrian Koh, Nikita Arnold, et al. A lesson from plants: high-speed soft robotic actuators. *Advanced Science*, 7(5):1903391, 2020.

[80] Alar Ainla, Mohit S. Verma, Dian Yang, and George M. Whitesides. Soft, Rotating Pneumatic Actuator. *Soft Robot.*, 4(3):297–304, May 2017.

[81] Xiaobin Ji, Xinchang Liu, Vito Cacucciolo, Matthias Imboden, Yoan Civet, Alae El Haitami, Sophie Cantin, Yves Perriard, and Herbert Shea. An autonomous untethered fast soft robotic insect driven by low-voltage dielectric elastomer actuators. *Sci. Robo.*, 4(37):eaaz6451, December 2019.

[82] Johannes T. B. Overvelde, Tamara Kloek, Jonas J. A. D'haen, and Katia Bertoldi. Amplifying the response of soft actuators by harnessing snap-through instabilities. *Proc. Natl. Acad. Sci.*, 112(35):10863–10868, September 2015.

[83] Daniel Bruch, Steffen Hau, Philipp Loew, Gianluca Rizzello, and Stefan Seelecke. Fast model-based design of large stroke dielectric elastomer membrane actuators biased with pre-stressed buckled beams, 2018.

[84] Adrienne Crivaro, Robert Sheridan, Mary Frecker, Timothy W Simpson, and Paris Von Lockette. Bistable compliant mechanism using magneto active elastomer actuation. *Journal of Intelligent Material Systems and Structures*, 27(15):2049–2061, August 2016.

[85] Jae-Hung Han, Reynolds Addo-Akoto, Jong-Seob Han, Jong-Eun Suh, and Jongwan Lee. Buckled bistable beam actuation with twisted strings. In Alper Erturk, editor, *Active and Passive Smart Structures and Integrated Systems XII*, page 30, Denver, United States, March 2018. SPIE.

[86] Tiefeng Li, Zhanan Zou, Guoyong Mao, and Shaoxing Qu. Electromechanical bistable behavior of a novel dielectric elastomer actuator. *Journal of Applied Mechanics*, 81(4):041019, November 2013.

[87] Lior Medina, Rivka Gilat, Bojan Ilic, and Slava Krylov. Two-directional operation of bistable latchable micro switch actuated by a single electrode. *Proceedings*, 1(4):277, August 2017.

[88] Renjing Gao, Mingli Li, Qi Wang, Jian Zhao, and Shutian Liu. A novel design method of bistable structures with required snap-through properties. *Sensors and Actuators A: Physical*, 272:295 – 300, 2018.

[89] AH Nayfeh and RA Ibrahim. Nonlinear interactions: analytical, computational, and experimental methods. *Applied Mechanics Reviews*, 54:B60, 2001.

[90] Wenzhong Yan, Angela L Gao, Yunchen Yu, and Ankur Mehta. Towards autonomous printable robotics: Design and prototyping of the mechanical logic. *Proceedings of the 2018 International Symposium on Experimental Robotics*, pages 631–644, 2020.

[91] Singiresu S Rao and Fook Fah Yap. *Mechanical vibrations*, volume 4. Prentice hall Upper Saddle River, 2011.

[92] Hassen M. Ouakad and Mohammad I. Younis. The dynamic behavior of MEMS arch resonators actuated electrically. *International Journal of Non-Linear Mechanics*, 45(7):704–713, September 2010.

[93] Wenzhong Yan, Yunchen Yu, and Ankur Mehta. Rapid Design of Mechanical Logic Based on Quasi-Static Electromechanical Modeling. In *2019 IEEE/RSJ International Conference on Intelligent Robots and Systems (IROS)*, pages 5820–5825, November 2019.

[94] Mattias Vangbo. An analytical analysis of a compressed bistable buckled beam. *Sensors and Actuators A: Physical*, 69(3):212 – 216, 1998.

[95] Jin Qiu, J. H. Lang, and A. H. Slocum. A curved-beam bistable mechanism. *Journal of Microelectromechanical Systems*, 13(2):137–146, 2004.

[96] Paul Cazottes, Amâncio Fernandes, Joël Pouget, and Moustapha Hafez. Bistable Buckled Beam: Modeling of Actuating Force and Experimental Validations. *Journal of Mechanical Design*, 131(10):101001–101010, sep 2009.

[97] B. Camescasse, A. Fernandes, and J. Pouget. Bistable buckled beam and force actuation: Experimental validations. *International Journal of Solids and Structures*, 51(9):1750 – 1757, 2014.

[98] Daniel Bruch, Steffen Hau, Philipp Loew, Gianluca Rizzello, and Stefan Seelecke. Fast model-based design of large stroke dielectric elastomer membrane actuators biased with pre-stressed buckled beams. *Proc.SPIE*, 10594:10594 – 10594 – 8, 2018.

[99] Tiefeng Li, Zhanan Zou, Guoyong Mao, and Shaoxing Qu. Electromechanical Bistable Behavior of a Novel Dielectric Elastomer Actuator. *Journal of Applied Mechanics*, 81(4):41015–41019, nov 2013.

[100] Jin-Han Jeon, Tai-Hong Cheng, and Il-Kwon Oh. Snap-through dynamics of buckled ipmc actuator. *Sensors and Actuators A: Physical*, 158(2):300 – 305, 2010.

[101] Xue Hou, Yin Liu, Guangchao Wan, Zhe Xu, Chunsheng Wen, Hui Yu, John X. J. Zhang, Jianbao Li, and Zi Chen. Magneto-sensitive bistable soft actuators: Experiments, simulations, and applications. *Applied Physics Letters*, 113(22):221902, 2018.

[102] Reynolds Addo-Akoto and Jae-Hung Han. Bidirectional actuation of buckled bistable beam using twisted string actuator. *Journal of Intelligent Material Systems and Structures*, 0(0):1045389X18817830, 2018.

[103] Wenzhong Yan, Yunchen Yu, and Ankur Mehta. Analytical modeling for rapid design of bistable buckled beams. *Theoretical and Applied Mechanics Letters*, 9(4):264–272, July 2019.

[104] C.-T. Pan, H. Yang, M.-K. Wei, and F.-Y. Chang. Pet polymer ablation using excimer laser for nozzle plate application. *Materials Science and Technology*, 23(8):980–986, August 2007.

[105] Jie Hong, Wenzhong Yan, Yanhong Ma, Dayi Zhang, and Xin Yang. Experimental investigation on the vibration tuning of a shell with a shape memory alloy ring. *Smart Materials and Structures*, 24(10):105007, September 2015.

[106] Jin Qiu, Jeffrey Lang, and Alexander Slocum. A curved-beam bistable mechanism. *Journal of Microelectromechanical Systems*, 13(2):137–146, April 2004.

[107] Daniela Rus and Michael T Tolley. Design, fabrication and control of origami robots. *Nat. Rev. Mater.*, 3(6):101–112, 2018.

[108] Haitao Yang, Bok Seng Yeow, Zhipeng Li, Kerui Li, Ting-Hsiang Chang, Lin Jing, Yang Li, John S Ho, Hongliang Ren, and Po-Yen Chen. Multifunctional metallic backbones for origami robotics with strain sensing and wireless communication capabilities. *Sci. Robot.*, 4(33):eaax7020, 2019.

[109] Benjamin Treml, Andrew Gillman, Philip Buskohl, and Richard Vaia. Origami mechanologic. *Proc. Natl. Acad. Sci. U.S.A.*, 115:6916–6921, 2018.

[110] Yuanping Song, Robert M Panas, Samira Chizari, Lucas A Shaw, Julie A Jackson, Jonathan B Hopkins, and Andrew J Pascall. Additively manufacturable micromechanical logic gates. *Nat. Commun.*, 10(1):1–6, 2019.

[111] Marc Z Miskin, Alejandro J Cortese, Kyle Dorsey, Edward P Esposito, Michael F Reynolds, Qingkun Liu, Michael Cao, David A Muller, Paul L McEuen, and Itai Cohen. Electronically integrated, mass-manufactured, microscopic robots. *Nature*, 584(7822):557–561, 2020.

[112] Michael Andrew McEvoy and Nikolaus Correll. Materials that couple sensing, actuation, computation, and communication. *Science*, 347(6228):1261689, 2015.

[113] Guang-Zhong Yang, Jim Bellingham, Pierre E Dupont, Peer Fischer, Luciano Floridi, Robert Full, Neil Jacobstein, Vijay Kumar, Marcia McNutt, Robert Merrifield, et al. The grand challenges of science robotics. *Sci. Robot.*, 3(14):eaar7650, 2018.

[114] Qingkun Liu, Wei Wang, Michael F Reynolds, Michael C Cao, Marc Z Miskin, Tomas A Arias, David A Muller, Paul L McEuen, and Itai Cohen. Micrometer-sized electrically programmable shape-memory actuators for low-power microrobotics. *Sci. Robot.*, 6(52):eabe6663, 2021.

[115] Owies M Wani, Hao Zeng, and Arri Priimagi. A light-driven artificial flytrap. *Nat. Commun.*, 8(1):1–7, 2017.

[116] Priyanka Bhovad, Joshua Kaufmann, and Suyi Li. Peristaltic locomotion without digital controllers: Exploiting multi-stability in origami to coordinate robotic motion. *Extreme Mech. Lett.*, 32:100552, 2019.

[117] Wenzhong Yan and Ankur Mehta. A cut-and-fold self-sustained compliant oscillator for autonomous actuation of origami-inspired robots. *Soft Robot.*, 9(5):871–881, 2022.

[118] Wenzhong Yan and Ankur Mehta. A crawling robot driven by a folded self-sustained oscillator. *2022 IEEE 5th International Conference on Soft Robotics*, pages 455–460, 2022.

[119] M Garrad, Gabor Soter, AT Conn, Helmut Hauser, and Jonathan Rossiter. A soft matter computer for soft robots. *Sci. Robot.*, 4(33):eaaw6060, 2019.

[120] Daniel J Preston, Philipp Rothemund, Haihui Joy Jiang, Markus P Nemitz, Jeff Rawson, Zhigang Suo, and George M Whitesides. Digital logic for soft devices. *Proc. Natl. Acad. Sci. U.S.A.*, 116(16):7750–7759, 2019.

[121] Sukho Song, Sagar Joshi, and Jamie Paik. Cmos-inspired complementary fluidic circuits for soft robots. *Adv. Sci.*, 8(20):2100924, 2021.

[122] Dylan Drotman, Saurabh Jadhav, David Sharp, Christian Chan, and Michael T Tolley. Electronics-free pneumatic circuits for controlling soft-legged robots. *Sci. Robot.*, 6(51):eaay2627, 2021.

[123] Charles El Helou, Philip R Buskohl, Christopher E Tabor, and Ryan L Harne. Digital logic gates in soft, conductive mechanical metamaterials. *Nat. Commun.*, 12(1):1–8, 2021.

[124] Charles El Helou, Benjamin Grossmann, Christopher E. Tabor, Philip R. Buskohl, and Ryan L Harne. Mechanical integrated circuit materials. *Nature*, 608(1):699–703, 2022.

[125] C Kaspar, BJ Ravoo, Wilfred G Van der Wiel, SV Wegner, and WHP Pernice. The rise of intelligent matter. *Nature*, 594(7863):345–355, 2021.

[126] Metin Sitti. Physical intelligence as a new paradigm. *Extreme Mech. Lett.*, 46:101340, 2021.

[127] Johannes TB Overvelde. Popping, locking robots. *Nat. Mater.*, 20(12):1590–1591, 2021.

[128] Zhiqiang Meng, Weitong Chen, Tie Mei, Yuchen Lai, Yixiao Li, and C.Q. Chen. Bistability-based foldable origami mechanical logic gates. *Extreme Mech. Lett.*, 43:101180, February 2021.

[129] Min Zhang, Jiaxing Jeccy Sun, Muhammad Khatib, Zi-Yang Lin, Zi-Han Chen, Walaa Saliba, Yehu David Horev, Viki Kloper, Yana Milyutin, Tan-Phat Huynh, et al. Time-space-resolved origami hierarchical electronics for ultrasensitive detection of physical and chemical stimuli. *Nat. Commun.*, 10(1):1–10, 2019.

[130] Mustafa Boyvat, Je-Sung Koh, and Robert J Wood. Addressable wireless actuation for multijoint folding robots and devices. *Sci. Robot.*, 2(8):eaan1544, 2017.

[131] Larissa S Novelino, Qiji Ze, Shuai Wu, Glaucio H Paulino, and Ruike Zhao. Untethered control of functional origami microrobots with distributed actuation. *Proc. Natl. Acad. Sci. U.S.A.*, 117(39):24096–24101, 2020.

[132] Hang Zhang, Jun Wu, Daining Fang, and Yihui Zhang. Hierarchical mechanical metamaterials built with scalable tristable elements for ternary logic operation and amplitude modulation. *Sci. Adv.*, 7(9):eabf1966, 2021.

[133] Wenzhong Yan, Chang Liu, and Ankur Mehta. Origami logic gates for printable robots. *2021 IEEE/RSJ International Conference on Intelligent Robots and Systems*, pages 6084–6089, 2021.

[134] Qiguang He, Zhijian Wang, Yang Wang, Adriane Minori, Michael T Tolley, and Shengqiang Cai. Electrically controlled liquid crystal elastomer–based soft tubular actuator with multimodal actuation. *Sci. Adv.*, 5(10):eaax5746, 2019.

[135] Wenlong Li, Naoji Matsuhisa, Zhiyuan Liu, Ming Wang, Yifei Luo, Pingqiang Cai, Geng Chen, Feilong Zhang, Chengcheng Li, Zhihua Liu, et al. An on-demand plant-based actuator created using conformable electrodes. *Nat. Electron.*, 4(2):134–142, 2021.

[136] Philipp Rothemund, Alar Ainla, Lee Belding, Daniel J Preston, Sarah Kurihara, Zhigang Suo, and George M Whitesides. A soft, bistable valve for autonomous control of soft actuators. *Sci. Robot.*, 3(16):eaar7986, 2018.

[137] Hortense Le Ferrand, Andre R Studart, and Andres F Arrieta. Filtered mechanosensing using snapping composites with embedded mechano-electrical transduction. *ACS nano*, 13(4):4752–4760, 2019.

[138] Jan T Burri, Eashan Saikia, Nino F Läubli, Hannes Vogler, Falk K Wittel, Markus Rüggeberg, Hans J Herrmann, Ingo Burgert, Bradley J Nelson, and Ueli Grossniklaus. A single touch can provide sufficient mechanical stimulation to trigger venus flytrap closure. *PLoS Biol.*, 18(7):e3000740, 2020.

[139] Seung-Won Kim, Je-Sung Koh, Jong-Gu Lee, Junghyun Ryu, Maenghyo Cho, and Kyu-Jin Cho. Flytrap-inspired robot using structurally integrated actuation based on bistability and a developable surface. *Bioinspir. Biomim.*, 9(3):036004, 2014.

[140] Helmuth Spieler. Introduction to radiation-resistant semiconductor devices and circuits. *AIP Conference Proceedings*, 390(1):23–49, 1997.

[141] Zhi Ern Teoh, Brennan T Phillips, Kaitlyn P Becker, Griffin Whittredge, James C Weaver, Chuck Hoberman, David F Gruber, and Robert J Wood. Rotary-actuated folding polyhedrons for midwater investigation of delicate marine organisms. *Sci. Robot.*, 3(20):eaat5276, 2018.

[142] Nina R Sinatra, Clark B Teeple, Daniel M Vogt, Kevin Kit Parker, David F Gruber, and Robert J Wood. Ultragentle manipulation of delicate structures using a soft robotic gripper. *Sci. Robot.*, 4(33):eaax5425, 2019.

[143] Jiro Okada. Cockroach antennae. *Scholarpedia of Touch*, pages 31–43, 2016.

[144] Jiaming Liang, Wu Yichuan, Justin K. Yim, Huimin Chen, Zicong Miao, Hanxiao Liu, Liu Ying, Yixin Liu, Dongkai Wang, Wenying Qiu, Zhichun Shao, Min Zhang, Xiaohao Wang, Junwen Zhong, and Liwei Lin. Electrostatic footpads enable agile insect-scale soft robots with trajectory control. *Sci. Robot.*, 6(55):eabe7906, 2021.

[145] Tian Chen, Mark Pauly, and Pedro M. Reis. A reprogrammable mechanical metamaterial with stable memory. *Nature*, 589(7842):386–390, January 2021.

[146] Wenzhong Yan and Ankur Mehta. Towards one-dollar robots: An integrated design and fabrication strategy for electromechanical systems. *Robotica*, 41(1):31–47, 2023.

[147] Chang Liu, Wenzhong Yan, and Ankur Mehta. Computational design and fabrication of corrugated mechanisms from behavioral specifications. *2021 IEEE International Conference on Robotics and Automation (ICRA)*, pages 7087–7093, 2021.

[148] Michael Gomez, Derek E. Moulton, and Dominic Vella. Critical slowing down in purely elastic 'snap-through' instabilities. *Nat. Phys.*, 13(2):142–145, February 2017.

[149] Cagdas D Onal, Michael T Tolley, Robert J Wood, and Daniela Rus. Origami-inspired printed robots. *IEEE/ASME Trans. Mechatronics*, 20(5):2214–2221, 2014.

[150] Zhenishbek Zhakypov, Kazuaki Mori, Koh Hosoda, and Jamie Paik. Designing minimal and scalable insect-inspired multi-locomotion millirobots. *Nature*, 571(7765):381–386, 2019.

[151] Luyang Zhao, Yijia Wu, Wenzhong Yan, Weishu Zhan, Xiaonan Huang, Joran Booth, Ankur Mehta, Kostas Bekris, Rebecca Kramer-Bottiglio, and Devin Balkcom. Starblocks: Soft actuated self-connecting blocks for building deformable lattice structures. *IEEE Robotics and Automation Letters*, 2023.

[152] Guoyong Mao, Michael Drack, Mahya Karami-Mosammam, Daniela Wirthl, Thomas Stockinger, Reinhard Schwödiauer, and Martin Kaltenbrunner. Soft electromagnetic actuators. *Sci. Adv.*, 6(26):eabc0251, 2020.

[153] Dian Yang, Mohit S Verma, Ju-Hee So, Bobak Mosadegh, Christoph Keplinger, Benjamin Lee, Fatemeh Khashai, Elton Lossner, Zhigang Suo, and George M Whitesides. Buckling pneumatic linear actuators inspired by muscle. *Adv. Mater. Technol.*, 1(3):1600055, 2016.

[154] Markus P Nemitz, Christoffer K Abrahamsson, Lukas Wille, Adam A Stokes, Daniel J Preston, and George M Whitesides. Soft non-volatile memory for non-electronic information storage in soft robots. *2020 3rd IEEE International Conference on Soft Robotics*, pages 7–12, 2020.

[155] Guangchao Wan, Yin Liu, Zhe Xu, Congran Jin, Lin Dong, Xiaomin Han, John XJ Zhang, and Zi Chen. Tunable bistability of a clamped elastic beam. *Extreme Mech. Lett.*, 34:100603, 2020.

[156] Shuhei Miyashita, Laura Meeker, Michael T Tolley, Robert J Wood, and Daniela Rus. Self-folding miniature elastic electric devices. *Smart Mater. Struct.*, 23(9):094005, 2014.

[157] J P Whitney, P S Sreetharan, K Y Ma, and R J Wood. Pop-up book MEMS. *Journal of Micromech. Microeng.*, 21(11):115021, oct 2011.

[158] Teresa A Kent, Michael J Ford, Eric J Markvicka, and Carmel Majidi. Soft actuators using liquid crystal elastomers with encapsulated liquid metal joule heaters. *Multifunct. Mater.*, 3(2):025003, 2020.

[159] Ankur M Mehta, Joseph DelPreto, Kai Weng Wong, Scott Hamill, Hadas Kress-Gazit, and Daniela Rus. Robot creation from functional specifications. *Robotics Research: Volume 2*, pages 631–648, 2018.

[160] Isaac A Cabrera, Zhaoliang Zheng, Patricia Castillo, Eric Ngo, Sebastian Troncoso, Win-Ying Zhao, Niyonika Sheth, Connie Gean, Jan Hsiao, John Vincent Laxa, et al. Smartphone telemedicine: A novel workflow for creating prosthetic sockets using semi-automated photogrammetry. *preprint, Jul*, 2020.

[161] Mihai Duduta, Sebastien de Rivaz, David R Clarke, and Robert J Wood. Ultra-lightweight, high power density lithium-ion batteries. *Batter. Supercaps*, 1(4):131–134, 2018.

[162] J P Whitney, P S Sreetharan, K Y Ma, and R J Wood. Pop-up book MEMS. *Journal of Micromechanics and Microengineering*, 21:115021, November 2011.